Astronomy Reports, Vol. 46, No. 3, 2002, pp. 173–181. Translated from Astronomicheskiĭ Zhurnal, Vol. 79, No. 3, 2002, pp. 195–204.

Does the LMC Possess a Dark Bulge?

A. V. Zasov and A. V. Khoperskov

Sternberg Astronomical Institute, Universitetskiĭ pr. 13, Moscow, 119899 Russia

Received June 15, 2001

Abstract—A series of numerical dynamical models for the LMC are constructed in order to fit the observed rotational velocities and stellar velocity dispersions at various galactocentric distances. The models include a three-dimensional spherical disk and nonevolving spherical components with various relative masses. The two LMC rotation curves presented by Kim *et al.* (1998) and Sofue (2000), which differ strongly in the inner region of the galaxy, are compared. The latter curve requires the presence of a massive dark bulge. Models based on the rotation curve of Sofue (2000) cannot account for the observed velocity dispersion or the presence of a long-lived bar in the galaxy. A model with no dark bulge is in good agreement with the observations if we assume that the disk dominates over the halo in terms of the mass within the optical radius (about 7 kpc). © *2002 MAIK "Nauka/Interperiodica"*.

1. INTRODUCTION

The results of recent studies suggest that the morphology of the Large Magellanic Cloud is more complex than previously believed. When observed in HI, the galaxy appears more symmetrical than in optical images and resembles a classical disk galaxy [1]. The gaseous disk can be traced to a galactocentric distance of 7 kpc. Individual stars can be distinguished to about the same distance. Rotation-curve measurements based on HI and brightest-star observations can be used to construct models for the mass distribution in the galaxy. The photometric and stellar-kinematic data, as well as the presence of a bar, appreciably constrain the uncertainties in the free parameters describing the radial dependences of the mass density in the disk and halo.

At large distances from the center of the LMC, the observed disk rotational velocities (as inferred from both gas and stars) lie in the range 68–80 km/s, with no sign of a velocity decrease with radius. Sofue's [2] reanalysis of the data of Kim *et al.* [1] led him to construct an HI rotation curve with a significantly higher rotational-velocity gradient in the central region ($r \lesssim 2$ kpc) than for the $V^K_{\rm gas}$ rotation curve of Kim *et al.* [1]. This discrepancy is due primarily to the different choices of kinematic center in the two studies. To explain the high gradient of the gas velocity in the vicinity of his adopted center, Sofue [2] had to introduce a dark bulge, which mainly affects motions at $r \lesssim 1$ kpc. The second distinguishing feature of Sofue's [2] model is the short radial scale of the surface density, equal to 1 kpc—significantly smaller than the exponential scale length of $L = 1.6$ kpc usually adopted for the LMC. No massive bulge is required to interpret the rotation curve reported by Kim *et al.* [1]. To investigate whether or not the LMC has such a dark, massive bulge, we constructed two series of dynamical models for each of these rotation curves. Our dynamical modeling was based on a numerical solution of the equations of motion for N self-gravitating bodies, taking into account the external potential.

The aim of the dynamical modeling was to obtain constraints that would make it possible to choose between the rotation curves of Kim *et al.* [1] and Sofue [2], and thereby test the possibility that the LMC has a dark bulge. Our main conclusion is that the rotation curve of Kim *et al.* [1] is in better agreement with the collected observational data for the LMC and that no significant amount of dark mass inside the LMC is required.

2. DYNAMICAL MODELING

The observed rotation curve of the galaxy is consistent with various radial density distributions in the disk and spherical subsystems, so estimates of the relative masses of these subsystems can vary appreciably. This uncertainty can be reduced significantly by requiring that the model rotational velocities and stellar velocity dispersions both agree with the observed values. Our analysis is based on the assumption that the stellar velocity dispersion ensures gravitational stability of the stellar disk in the LMC. Therefore, when modeling the galaxy, we initially specified an obviously unstable distribution of the velocity dispersion in the stellar disk, which attained a quasi-stationary level in the process of its

1063-7729/02/4603-0173$22.00

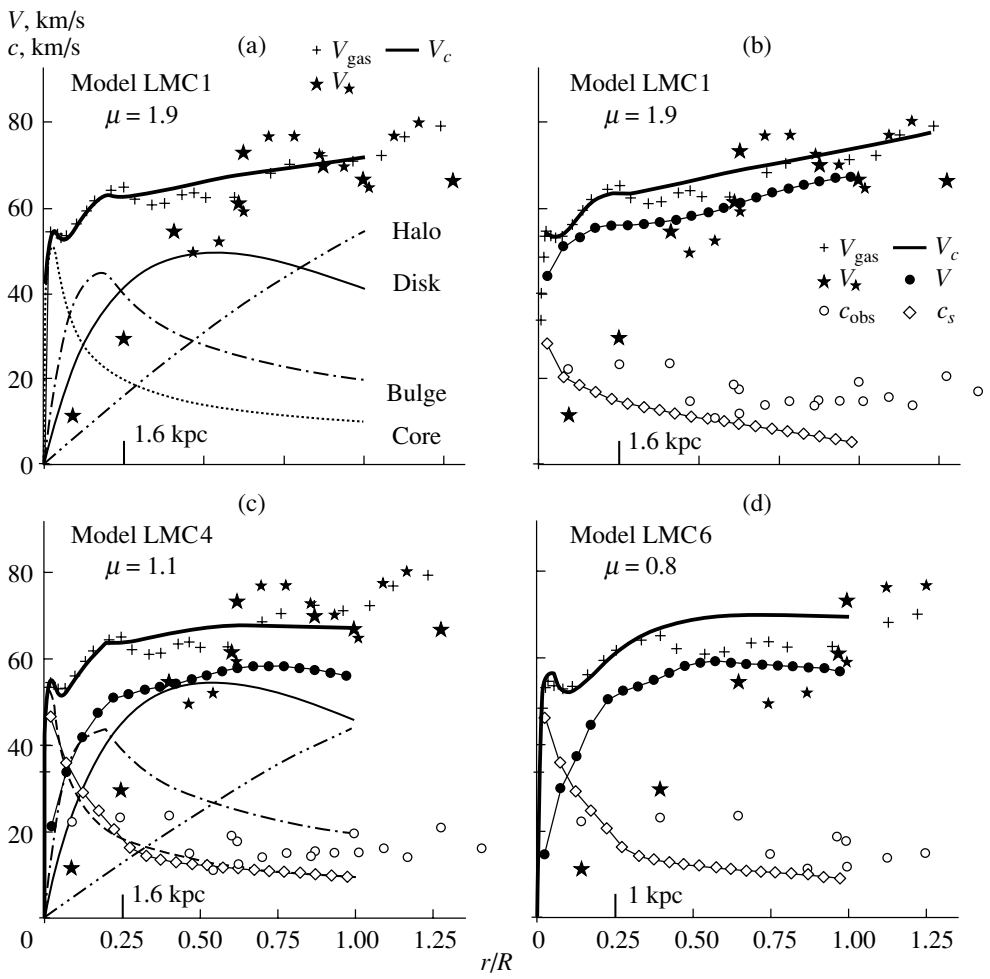

Fig. 1. (a) Disk, halo, bulge, and core contributions to the circular velocity of the galaxy (solid bold curve) and the radial distributions of the observed and model velocities for models with (b) $\mu = 1.9$ and $L = 1.6$ kpc (LMC1), (c) $\mu = 1.1$ and $L = 1.6$ kpc (LMC4), and (d) the maximum-disk model with $\mu = 0.8$ and $L = 1$ kpc. Shown are the HI rotational velocities (+), the stellar rotational velocities ($\star$); large and small symbols correspond to data from [17] and [6], respectively), the observed stellar velocity dispersion ($\circ$), model estimates of the stellar rotational velocities ($\bullet$), and model estimates of the stellar line-of-sight velocity dispersion ($\diamond$).

evolution. In this approach, under certain conditions, the disk can develop a bar.

A detailed description of the dynamical stellar-disk models and conditions for the numerical simulations we applied can be found in [3]. The main feature of this study is that we now compute the gravitational forces between particles using the TREEcode algorithm [4] instead of the particle–particle method, making it possible to increase the number of particles N. The comparison of models with the same initial conditions and the same number of particles convinced us of the good agreement between the results obtained using the two different methods.

The LMC contains a significant amount of gas ($M_{gas} = 5.2 \times 10^8\, M_\odot$ within 8 kpc), which makes up $\sim 7\%$ of the total mass [1]. However, in our modeling, we do not distinguish between the gaseous and stellar subsystems and assign both components to the disk. The model consists of a disk with finite width and radius $R_d = 4L$ (where L is the radial exponential disk scale length) and a spherical subsystem. In general, the spherical subsystem includes three components: core, bulge, and halo. We fitted the volume density distribution of the first two components by the King law

$$\varrho_{c,\,b} = \frac{(\varrho_0)_{c,\,b}}{\left[1 + (r/b_{c,\,b})^2\right]^{3/2}},$$

where the subscripts c and b refer to the core and bulge, respectively. The masses in these subsystems are contained only within some radius $r \le (r_{c,\,b})_{max}$. We approximated the density distribution in the halo

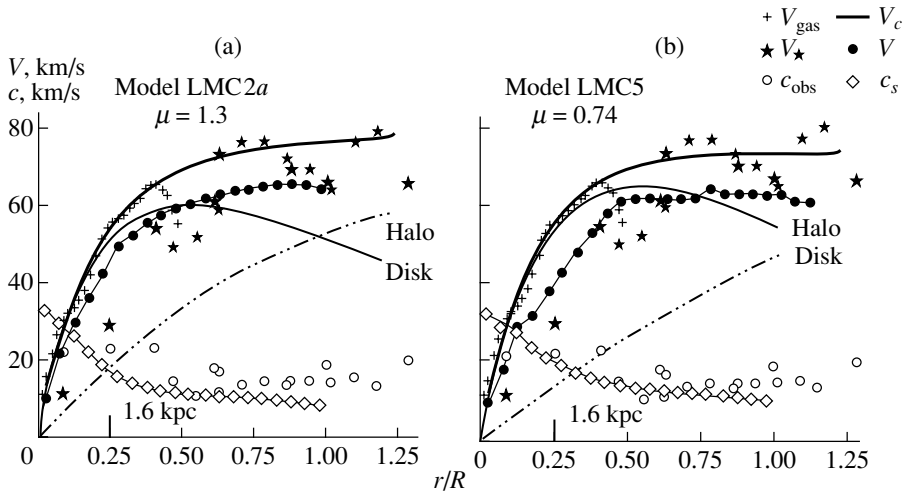

Fig. 2. Comparison of the observed and model parameters of the rotation curve $V^K_{gas}(r)$ for (a) the model with a massive halo $\mu = 1.3$ and (b) the maximum-disk model ($\mu = 0.74$). Notation is the same as in Fig. 1.

by the quasi-isothermal law

$$\varrho_h = \frac{\varrho_{0h}}{1 + (r/a)^2}$$

characterized by two parameters: the scale length a and central density ϱ_{0h}, or, alternatively, the mass M_h within $r \le R = 4L$. The total relative mass of the spherical components is $\mu = (M_h + M_b + M_c)/M_d$. We assumed all nondisk components to be rigid, i.e., nonevolving. In our dynamical models, we used a system of units in which the gravitational constant $G = 1$, $R = 1$, and the disk mass $M_d = 1$.

The results of the dynamical modeling include the radial dependences of the circular rotational velocity V_c, azimuthal velocity V of the disk rotation, and line-of-sight velocity dispersion $c_s = \sqrt{c_\varphi^2 \sin^2 i + c_z^2 \cos^2 i}$ along the major axis of the galaxy. The development of barlike features can be identified via Fourier analysis of the surface density in φ and $\ln r$ [5] coordinates. For the Fourier coefficients, we have

$$A(m,p,t) = \frac{1}{N}\sum_{j=1}^{N} \exp\left\{i\left[m\varphi_j(t) + p\ln r_j(t)\right]\right\},$$

where r_j and φ_j are the radial and azimuthal coordinates of the jth particle, m is an integer, and the parameter p characterizes the degree of twisting of the spiral waves. We performed our computations with $m = 0, 1, 2, 3, 4, 5, 6$, and various p values. The case $p = 0$ corresponds to spoke-type perturbations. The domination of perturbations with $m = 2$ and $p = 0$ indicates the presence of a bar. We also considered the integrated amplitudes of the Fourier harmonics

$$\hat{A}(m) = \sqrt{\sum_{p=-15}^{15} |A(m,p)|^2}.$$

The heating of an initially cool disk can involve a substantial redistribution of mass, which slightly changes the circular rotational velocity. This results in a dependence (usually weak) of the radial velocity dispersion $c_r(r)$ on the initial state of the system. To avoid this, when constructing a marginally stable equilibrium disk, we used an iterative procedure in which we could chose a subcritical level for the initial state. In the first iteration, we specified obviously unstable initial distributions of the velocity dispersion and disk thickness. We performed the next computation from an initial state intermediate between the initial and final states (after several disk revolutions) of the previous iteration, etc.

3. OBSERVATIONAL DATA

3.1. Mass Distribution in the Disk Component

We used the commonly accepted values for the LMC's distance (50.1 kpc) and inclination ($i = 33°$) [6].

The radial profiles of the disk surface brightness, RR Lyrae stars, and carbon stars fit an exponential law with $L = 1.6$ kpc well (see [7] and references therein).

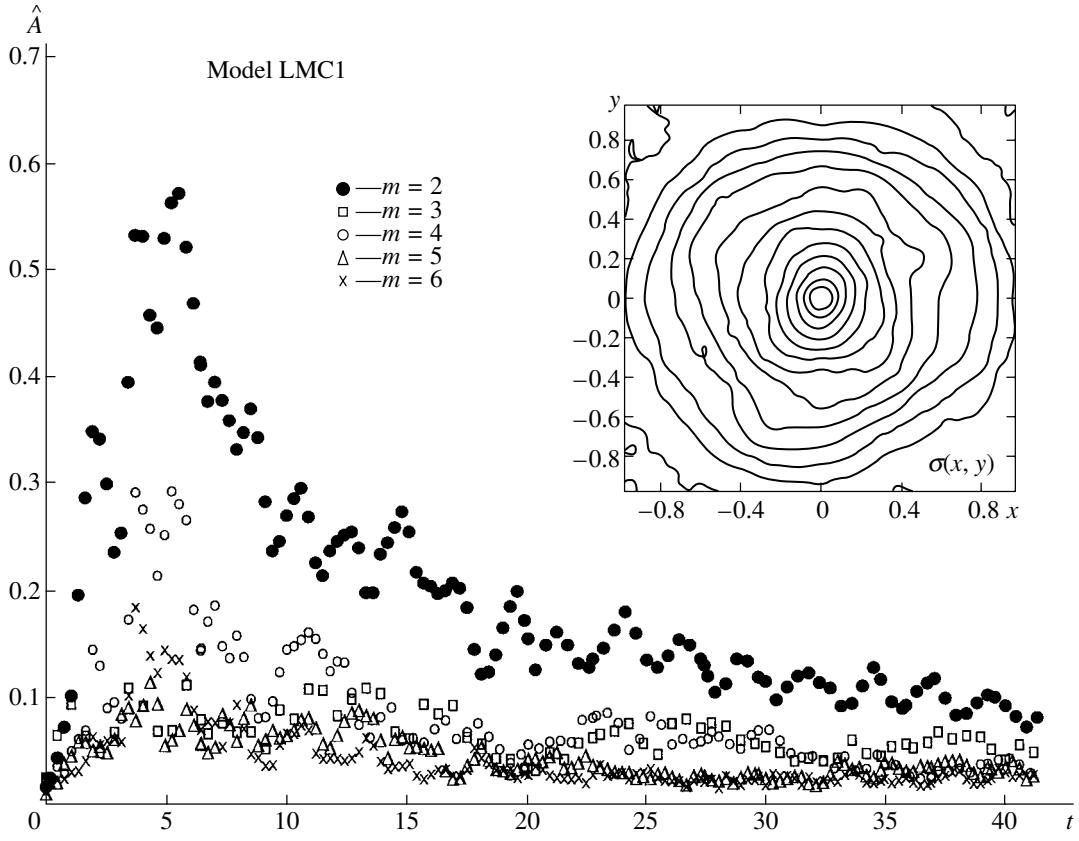

Fig. 3. Time dependence of the integrated amplitudes of Fourier harmonics for various modes m in the model with $V^S_{\rm gas}(r)$. Waves with different azimuthal numbers dissipate after the disk heats ($t \gtrsim 10$). The final state of the system is axisymmetric, without the development of a long-lived bar. The inset shows contours of surface density in the disk plane $\sigma(x, y)$ at $t = 40$, which corresponds to 5 Gyr.

3.2. The Bar

An optical bar about 3.3 kpc in length stands out in the central part of the LMC. A distinctive feature of the central region of the LMC is the offset between the bar and the kinematic center [8]. Note, however, that the possible presence of a bar in the density distribution of the LMC is still under debate [9].

The observational data seem to rule out active star formation in the central region of the galaxy within the last $(2–4)\times10^9$ yr [10]. Holtzman [11] found most of the stars to be older than 4 Gyr and concluded that the fraction of old stars is higher in the bar region than in the outer regions of the galaxy, independent of the model adopted. We therefore assume that the bar in the LMC is a stable structural feature: its age is estimated to be 2–9 Gyr, based on various observational data [11–13]. It follows that, even if the bar initially formed as the result of a tidal interaction or some other mechanism, rather than the development of a global bar-mode instability, the conditions in the galaxy must allow the bar to persist for at least several billion years.

3.3. Kinematics of Gas and Stars

Our dynamical models are based on the gas rotation curves of Sofue [2] ($V^S_{\rm gas}(r)$) and Kim *et al.* [1] ($V^K_{\rm gas}(r)$) (Figs. 1a, 2a, bold curves). Figures 1 and 2 also show the rotational velocities $V_\star$ and velocity dispersion $c_{\rm obs}$ of the stellar subsystem. We adopted a smoothed version of the gas rotation curve for the circular rotation curve $V_c(r)$.

The kimematics of the disk stars in the LMC have been studied fairly thoroughly. Kunkel *et al.* [6] constructed a rotation curve for galactocentric distances from 3–12 kpc based on data for 759 carbon stars. We use this rotation curve, taking into account the galaxy's inclination $i = 33°$ (Figs. 1, 2). The velocity dispersion for these stars varies only slightly with the radius and is equal to $c_{\rm obs} = 12–16$ km/s, which in the opinion of Kunkel *et al.* [6] indicates a relatively young age. In addition to these data, Figs. 1 and 2 show the radial dependences of the rotational velocity and velocity dispersion of the disk stars obtained by Alves and Nelson [7].

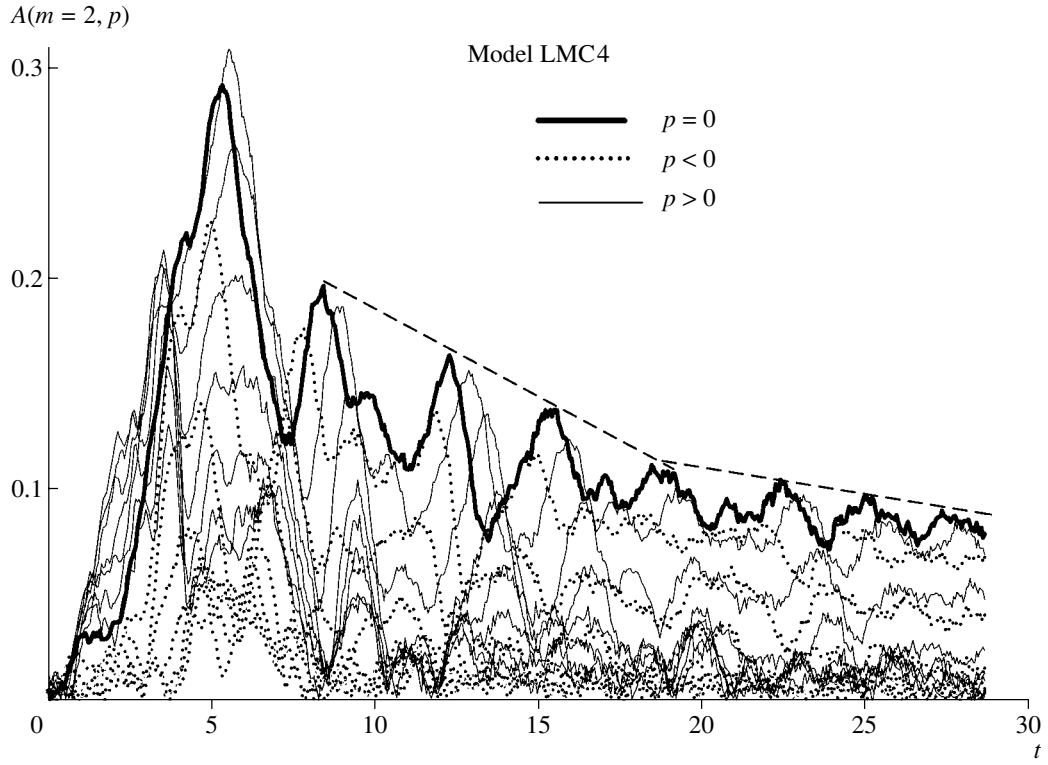

Fig. 4. Time dependence of the amplitudes of Fourier harmonics for the second mode $m = 2$ and various p. The bar mode ($p = 0$) slowly dissipates. The stellar orbital periods in the model are $t \simeq 5$ at a radial distance of $r = 6.4$ kpc.

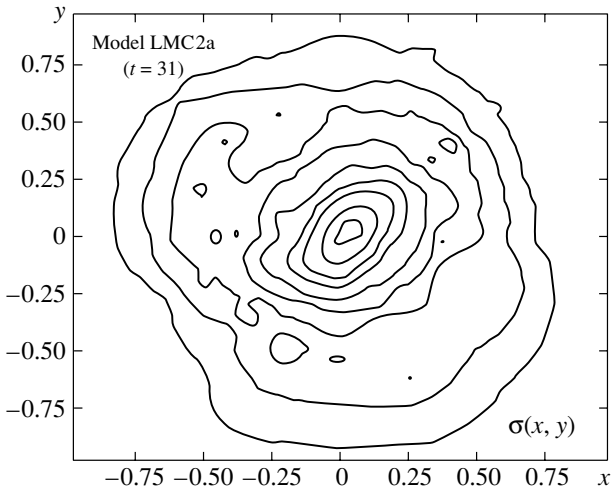

Fig. 5. Contours of surface density in the model with rotation curve $V^K_{\rm gas}(r)$, taking into account the inclination of the LMC. The center of mass (0, 0) is close to the center of the bar.

A kinematic analysis of more than five hundred carbon stars [14] revealed, together with a younger population with a velocity dispersion of about 8 km/s, an old disk component with a velocity dispersion of $\simeq 22$ km/s. Zaritsky *et al.* [15] derived a velocity dispersion of 18.4 ± 2.8 km/s based on data for 190 Vertical Red Clump stars. The kinematic data for planetary nebula reported by Meatheringham *et al.* [16] yield $c_{\rm obs} = 19.1 \pm 1$ km/s, in agreement with these results. An analysis of the motions of 975 carbon stars yielded a maximum circular rotational velocity of $\simeq 80$ km/s at a galactocentric distance of 3.4 kpc, and a line-of-sight velocity dispersion of $c_r = 28 \pm 14$ km/s for the disk component [17].

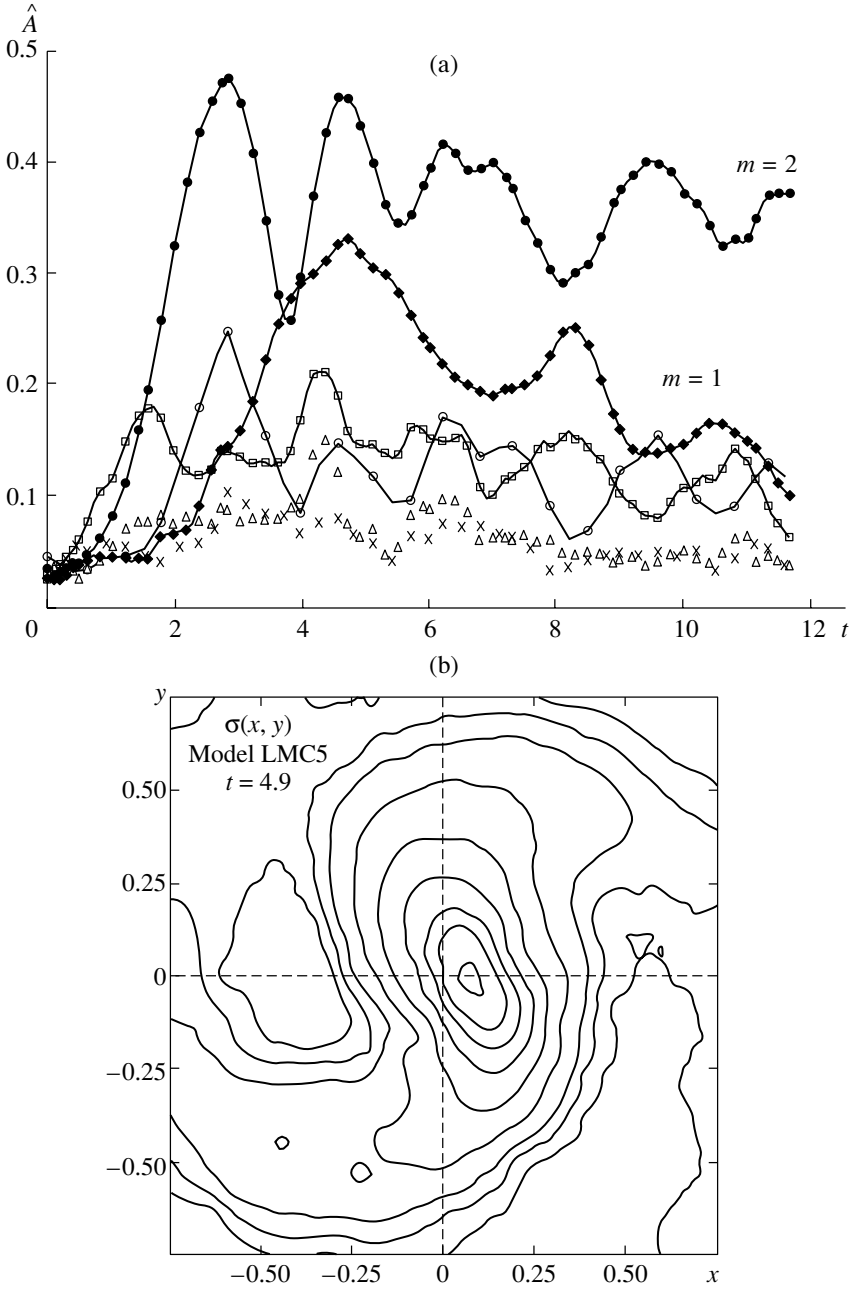

Fig. 6. (a) Time dependence of the integrated amplitudes of Fourier harmonics. At the initial stage of its evolution, the initially cool disk exhibits a large perturbation amplitude with azimuthal number $m = 1$. Notation is the same as in Fig. 3. (b) Contours of surface density at $t = 4.9$ (one orbital period of the disk). The kinematic center and center of mass are located at the intersection of the dashed lines.

Note that the radial dependence of the rotational velocity and stellar velocity dispersion change somewhat if we displace the kinematic center, following Sofue [2]. However, since the velocity dispersion $c_{\rm obs}$ depends only slightly on the radial distance, the radial profile of the velocity dispersion remains virtually unchanged and appreciable changes in the stellar rotation curve $V_\star$ are possible only in the central region, $r \lesssim 1$ kpc. It is for this reason, in particular, that the kinematic parameters of stars near the center of the LMC should be considered more trustworthy.

4. RESULTS OF DYNAMICAL MODELING OF THE LMC

To elucidate the role of certain factors relating the rotational velocity and stellar velocity dispersion, we constructed more than 20 dynamical models with various mass distributions and with $N = 40$–$180 \times$

10^3 disk particles. The table presents parameters for some of these models. Varying the number of particles enabled us to analyze the role of numerical effects in the dynamical models. When constructing models with the rotation curve $V^S_{\rm gas}(r)$ [2], we used more particles than when using the curve $V^K_{\rm gas}(r)$, in order to avoid numerical effects in the case of rapid rotation in the central region [18]. Since Sofue [2] considered a mass distribution that differs from the usually adopted brightness distribution in order to explain the rotation curve $V^S_{\rm gas}$ (see Section 3), we constructed several dynamical models with different radial disk scales $L =$ 1–1.6 kpc, treating it as a free parameter.

4.1. Dynamical models with the rotation curve V^S_{gas}

Let us now consider the case of the rotation curve $V^S_{\rm gas}(r)$ with $L = 1.6$ kpc and a massive halo ($\mu = 1.9$). To explain the central maximum in the rotation curve, the model includes a compact core with $b_c/L = 0.035$ in addition to the massive bulge ($M_b/M_d = 0.23$). Figure 1a shows the contributions from various components to the circular rotational velocity $V_c(r)$, and Fig. 1b the distributions of the observed quantities $c_{\rm obs}$, $V_{\rm gas}$, $V_\star$ and the corresponding model quantities c_s, V_c, and V. At the edge of the galaxy, a steady state is attained at very low stellar-velocity dispersions—the radial velocity dispersion is $c_r = 10$–14 km/s at $r > 3L$, which is comparable to the gas-velocity dispersion. This model assumes a substantial margin for stability: $c_s < c_{\rm obs}$ within the galaxy, where c_s and $c_{\rm obs}$ are line-of-sight velocity dispersions (see Section 2). The stellar rotational velocity V in this model is comparable to the circular velocity $V_{\rm c}$ and significantly exceeds the observed stellar rotational velocities $V_\star$ in the central region, which is one drawback of the model. Increasing μ worsens the discrepancy with the observed velocity dispersion.

Moreover, models with high μ fail to develop any long-lived bar, no matter what initial distribution of stellar velocity dispersion is considered. The combined effect of the two factors—the relatively massive halo and the concentrated core—make the central bar a short-lived feature that appears during the heating of the system, as evidenced by the decrease of the amplitudes of all Fourier harmonics, including the $m = 2$ mode, with time (Fig. 3). Even if the initial conditions are specified to correspond to a very cool disk with a small Toomre parameter $Q_T < 1$ throughout a large interval of radial distances, the system still develops a steady-state, axisymmetric density distribution after violent heating and the formation of a barlike feature at the initial stage (Fig. 3 shows contours of the surface-mass density at the outer disk boundary after ~ 12 orbital periods).

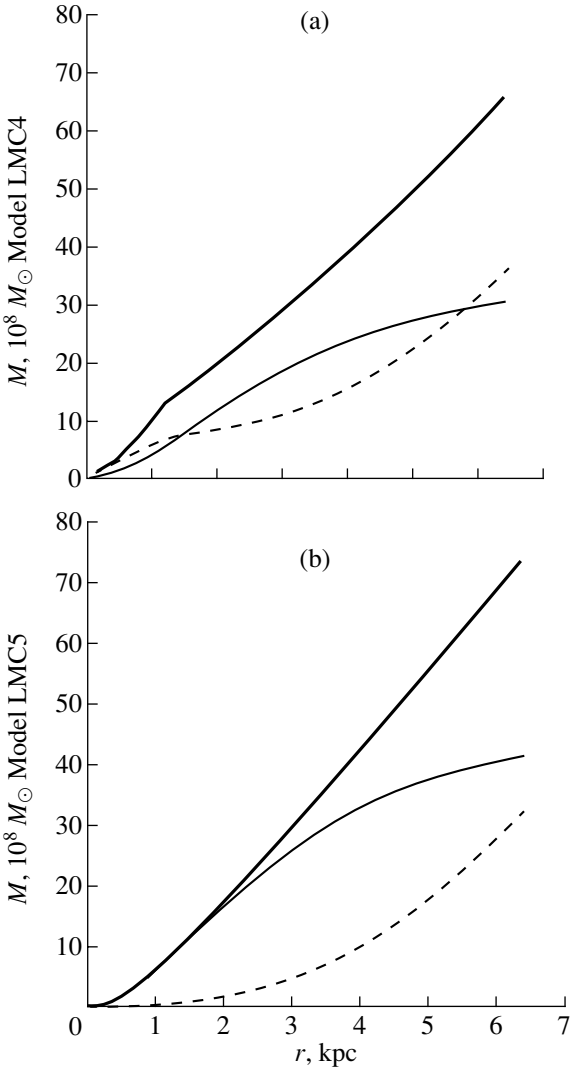

Fig. 7. Radial dependences of the mass contained within the radius r for the disk and spherical subsystems for models with rotation curves (a) $V^S_{\rm gas}(r)$ and (b) $V^S_{\rm gas}(r)$ (LMC 4 and LMC 5 models, respectively). The bold, thin solid, and dashed curves show the total mass, mass of the disk component, and mass of the spheroidal subsystem, respectively.

An alternative to the above model for the adopted L value is a maximum disk model (MDM), where $\mu =$ 1.1 (LMC4 model in Fig. 1c). In this case, the velocity dispersion c_s at the edge of the disk is in agreement with the observed distribution. However, the line-of-sight velocity dispersion in the central region is $c_s \simeq$ 40–50 km/s, in contradiction with the observations. An initially cool disk can develop a bar, which, however, also proves to be a short-lived feature. Figure 4a shows the time dependence of the amplitude $A(m = 2, p)$ of the second harmonic. The presence of a bar

Parameters of the dynamical models for the LMC

Model	N	M_n	a	M_b	b	$r_{\max}$	M_c	b	$r_{\max}$	μ
LMC2a	80000	1.3	0.66							1.3
LMC5	80000	0.74	1.07							0.74
LMC4	180000	0.9	1.26	0.18	0.074	0.20	0.041	0.0067	0.034	1.12
LMC1	180000	1.77	1.13	0.22	0.082	0.20	0.061	0.0092	0.039	2.05
LMC6	180000	0.71	1.98	0.071	0.070	0.32	0.53	0.0098	0.055	0.83

corresponds to $p = 0$. After it finally develops ($t \simeq 5$–6), the bar begins to be disrupted due to scattering in the concentrated core. As a result, its lifetime is limited to $\sim(2$–$3) \times 10^9$ yrs, which only slightly exceeds the lower limit for the bar's age based on an analysis of its stellar content. The shorter lifetime of the bar in the previous case ($\mu = 1.9$) compared to the case of $\mu = 1.1$ must be due not only to the different halo masses for the two models, but also to the fact that the disk becomes thicker in the MDM case. Therefore, a compact core with a radial scale length much shorter than the inferred vertical disk scale length of $h \simeq 360$ pc does not provide a rapid disruption of the bar mode, and the dissipation process continues over ~ 10 bar revolutions. The formation and subsequent evolution of the bar are characterized by a low value of the first harmonic $m = 1$, which is near the noise level, implying that the bar center, kinematic center, and center of mass are coincident.

Models with more concentrated disks ($L = 1$ kpc) and the same rotation curve $V^S_{\rm gas}$ show even poorer agreement with the observed velocity dispersion; nearly the entire disk has a large margin of stability, whereas the opposite condition is satisfied at the very center of the system: $c_{\rm obs} < c_s$.

4.2. Dynamical Models with the Rotation Curve V^K_{gas}

We now describe the results of dynamical modeling with the rotation curve $V^K_{\rm gas}(r)$, whose interpretation requires neither a bulge nor a core.

In model LMC2a, with a massive halo ($\mu = 1.3$), the stellar velocity dispersions obey the condition $c_s < c_{\rm obs}$ everywhere except at the very center, and satisfactory agreement is achieved with the rotational velocities of stars at $r > 1.5L$ (Fig. 2a). Better agreement can be achieved between the modeling results and the observed velocity dispersion and rotational velocity of stars in the MDM with $\mu = 0.7$ (model LMC5) for $V^K_{\rm gas}(r)$ (Fig. 2b). This confirms the small mass of the halo in the LMC reported by Zasov [19], based on kinematic data for disk globular clusters and the condition of marginal gravitational stability for the disk.

Models with the rotation curve $V^K_{\rm gas}(r)$ always develop a bar if the initial disk is not too hot. Figure 5 shows the model surface-brightness distribution, which exhibits a long-lived bar ($\simeq 4 \times 10^9$ yr if computed for the LMC). The presence of the bar is indicated by the domination of the $p = 0$ harmonic in the $m = 2$ mode. The angular rotational velocity of the bar in this model is $\Omega_{\rm bar} = 23$ km/(s kpc), which corresponds to a corotation radius of $R_{\rm c} \simeq 1.55$ kpc.

One distinguishing feature of the development of the bar structure in models with $V^K_{\rm gas}(r)$ is the large amplitude of the first mode $m = 1$ under certain conditions, which remains important throughout the evolution of the bar and characterizes the disruption of the bar's symmetry with respect to the center of the galaxy. This latter property is in good agreement with the observed offset between the kinematic center and bar center. Figure 6 shows the temporal dynamics of Fourier harmonics and surface-density contours in the bar region, which demonstrate the offset of the bar center relative to the kinematic center and the center of mass of the system as a whole at the initial stage, as a result of the development of perturbations with the azimuthal number $m = 1$. Due to the rigid halo in the dynamical model adopted here, this effect diminishes with time (Fig. 5). Note that bars whose centers are offset from the center of the galaxy as a whole are not uncommon among late-type galaxies. Numerical simulations show that this situation can arise when a bar develops in an initially cool disk where one-armed perturbations are subject to strong gravitational instability. This can take place when the mass of the disk is much greater than that of the halo nearly throughout the disk. The dominant instability of the $m = 1$ mode in the disk may be fairly typical of both the linear and nonlinear stages of the evolution of perturbations [18, 20].

The above discussion is illustrated in Fig. 7, which shows the radial dependences of the mass within a given radius for models LMC4 and LMC5. In the case of the rotation curve $V^S_{\rm gas}(r)$, the mass of the

disk dominates at 1.5 kpc $\leq r \leq$ 6 kpc (Fig. 7a). In the model based on the rotation curve $V^K_{\rm gas}(r)$, most of the mass of the galaxy can be concentrated in the disk components at all radii (Fig. 7b). In this case, the mass of the halo at $r < 2L = 3.2$ kpc is only 20% of the mass of the disk; i.e., dark mass plays only a minor role.

A model with a less massive halo ($\mu < 0.7$) consistent with $V_{\rm gas}$ beyond $r > 4$ kpc cannot be constructed using the isothermal halo model considered here. However, if the observed increase of the $V_{\rm gas}$ curve at the edge of the disk is due to tidal effects and not to an increase of the circular velocity, the mass of the halo may be even lower.

5. CONCLUSIONS

We now summarize the specific properties of models with the rotation curve as derived by Sofue (with a dark bulge) that make models with $V^K_{\rm gas}(r)$ (without a dark bulge) more consistent with the observations. (1) Models with $V^S_{\rm gas}(r)$ fail to explain the observed radial dependence of the stellar velocities in the inner part of the galaxy at $r < 2L$. (2) In these models, either the bar mode does not develop or the lifetime of the bar is insufficiently long. (3) In models with massive bulges, the amplitude of the one-arm mode $m = 1$ characterizing the asymmetry in the mass distribution is very small (comparable to the noise level) throughout the evolution of the system, in contrast to models with $V^K_{\rm gas}(r)$, where the $m = 1$ mode has a large amplitude during the development of the bar and is exceeded only slightly by the amplitude of the second mode throughout the evolution. This provides a natural explanation for the observed offset of the kinematic center of the LMC with respect to the center of the bar, even without invoking tidal effects. (4) To ensure disk stability, models with $V^S_{\rm gas}(r)$ require a line-of-sight stellar velocity dispersion of > 40 km/s, which appreciably exceeds the observed value $c_{\rm obs}$. Models with short radial disk scales $L \simeq 1$ kpc are less consistent with the observed distributions of the rotational velocity and stellar velocity dispersion than are models with $L = 1.6$ kpc.

Thus, the rotation curve of Kim *et al.* [1] appears to be preferable. Our results do not confirm the need for a dark bulge in the LMC.

When the dynamical models constructed are applied to the maximum-disk model for the LMC, the resulting halo mass within $r < 4L = 6.4$ kpc is about 70% of the mass of the disk component. The observed velocity dispersion at the edge of the disk ($c_{\rm obs}(r \geq 3) \simeq 16$–$20$ km/s) [6, 7, 17] implies that this region possesses a margin of stability, even in the MDM model. It is important that the dynamical models we have constructed do not rule out the existence of a more massive halo with $\mu \simeq 1$–2; however, in this case, the velocity dispersion in the stellar disk must be due to other factors than dynamical heating as a result of gravitational instability.

6. ACKNOWLEDGMENTS

This work was supported by the Russian Foundation for Basic Research (project no. 01-02-17597).

REFERENCES

1. S. Kim, L. Staveley-Smith, M. A. Dopita, *et al.*, Astrophys. J. **503**, 674 (1998).
2. Y. Sofue, Publ. Astron. Soc. Jpn. **51**, 445 (1999).
3. A. V. Khoperskov, A. V. Zasov, and N. V. Tyurina, Astron. Zh. **78**, 1 (2001) [Astron. Rep. **45**, 180 (2001)].
4. J. E. Barnes and P. Hut, Nature **324**, 446 (1986).
5. E. Athanassoula and J. Sellwood, Mon. Not. R. Astron. Soc. **221**, 213 (1986).
6. W. E. Kunkel, S. Demers, M. J. Irwin, and L. Albert, Astrophys. J. Lett. **488**, L129 (1997).
7. D. R. Alves and C. A. Nelson, Astrophys. J. **542**, 789 (2000).
8. L. T. Gardiner, C. Turfus, and M. E. Putman, Astrophys. J. Lett. **507**, L35 (1998).
9. H. S. Zhao and N. W. Evans, Astrophys. J. Lett. **545**, L35 (2000).
10. J. S. Gallagher, A. A. Cole, J. Holtzman, and T. Smecker-Hane, in *New Views of the Magellanic Clouds (IAU Symposium 190),* Ed. by Y.-H. Chu, N. Suntzeff, J. Hesser, and D. Bohlender (1999), p. 306.
11. J. A. Holtzman, J. S. Gallagher, A. A. Cole, *et al.*, Astron. J. **118**, 2262 (1999).
12. A. Ardeberg, B. Gustafsson, P. Linde, and P.-E. Nissen, Astron. Astrophys. **322**, 13 (1997).
13. A. S. Gusev, Astron. Zh. **75**, 506 (1998) [Astron. Rep. **42**, 446 (1998)].
14. D. S. Graff and A. P. Gould, Astrophys. J. **540**, 211 (2000).
15. D. Zaritsky, S. A. Shectman, and I. Thompson, Astron. J. **117**, 2268 (1999).
16. S. J. Meatheringham, M. A. Dopita, H. C. Ford, and B. L. Webster, Astrophys. J. **327**, 651 (1988).
17. D. R. Alves, in *Galaxy Disks and Disk Galaxies,* Ed. by J. G. Funes, S. J. and E. M. Corsini (Astronomical Society of the Pacific, San Francisco, 2000).
18. J. A. Sellwood and N. W. Evans, Astrophys. J. **546**, 176 (2001).
19. A. V. Zasov, Pis'ma Astron. Zh. **11**, 730 (1985) [Sov. Astron. Lett. **11**, 307 (1985)].
20. N. W. Evans and J. C. A. Read, Mon. Not. R. Astron. Soc. **300**, 106 (1998).

Translated by A. Dambis

Astronomy Reports, Vol. 46, No. 3, 2002, pp. 182–192. Translated from Astronomicheskiĭ Zhurnal, Vol. 79, No. 3, 2002, pp. 205–215.

Spatial Structure of the Globular Cluster M15

Z. I. Peĭkov[1] and P. I. Kadiĭskaya[2]

[1] *University for Foreign Students, Sofia, Bulgaria*

[2] *St. Kliment Okhridskiĭ University, Sofia, Bulgaria*

Received April 14, 2000

Abstract—The spatial structure of the metal-poor globular cluster M15 is studied as a function of magnitude interval ΔB and the limiting B magnitude of star counts. Astrometric and photometric measurements of two plates obtained with the 2-m reflector of the National Academy of Sciences of Bulgaria were used. Analysis of the differential and integrated apparent ($\Delta F(r)$ and $F(r)$) and spatial ($\Delta f(r)$ and $f(r)$) stellar density distributions in different ΔB intervals and to different limiting magnitudes reaching $B = 21.5^m$ indicates that the cluster structure changes systematically as we consider fainter stars, beginning with the transition region between the subgiant branch and the main-sequence turnoff in the $(V, B-V)$ diagram. This variation is manifest in two ways: a homological growth in the radii of spatial zones of the cluster and of the cluster radius in accordance with a single law, and variations in the stellar density, with the rate of increase in the number of faint stars growing toward the outer zones of the cluster. Empirical relations describing these variations and parameters determining the cluster structure are obtained. © *2002 MAIK "Nauka/Interperiodica".*

1. INTRODUCTION

This work continues our studies of the deep spatial structure of a number of globular and open clusters (M56 [1], M12 [2], NGC 6535 [3], NGC 6171 [4], NGC 5466 [5], M92 [6], the Pleiades, Prasepe, and Coma [7]) based on star counts, using the technique of Kholopov [8, 9]. We have already shown that the structure of these objects changes systematically with increasing limiting magnitude for cluster subsystems containing stars below the transition region between the subgiant branch and the main-sequence (MS) turnoff on the $(V, B-V)$ diagram. It is therefore of interest to apply the same technique to other clusters with different parameters.

In the current paper, we analyze the spatial structure of the metal-poor globular cluster M15 (NGC 7078) ($\alpha_{2000.0} = 21^{\rm h}30.0^m$, $\delta_{2000.0} = +12°10'$, $l = 65.02°$, $b = -27.32°$, concentration class CC=IV, $[m/{\rm H}] = -2.02$) in different magnitude intervals and to different limiting magnitudes for star counts. M15's strong metal deficiency, membership in the Galactic halo population, old age, and collapsed core make this cluster a very interesting object. Accordingly, both its photometric and structural properties have been comparatively well studied (see, e.g., [10–16]). However, a complete comparative analysis of the spatial structures of individual cluster subsystems to deep limiting magnitudes has not yet been carried out. A detailed analysis of the distribution of stars located near or below the MS turnoff can therefore provide additional information about the spatial structure of the cluster.

2. DATA

We performed star counts on plate no. 1824 and 1846 taken in 1991 at the Ritchey–Chrétien focus of the 2-m telescope ($F = 16$ m) of the National Astronomical Observatory of Bulgaria in 1991. The overall plate size was 30×30 cm, with a plate scale of $12.89''$/mm, and an unvignetted field radius of 12 cm. The emulsion used was ZU21, with a GG 385 filter. The exposure, seeing, and limiting magnitude for plate no. 1824 are $t = 15$ min, $\tau \approx 1''$, and $B = 19.25^m$, and the corresponding parameters for plate no. 1846 are $t = 120$ min, $\tau \approx 1.5''$, and $B = 21.5^m$.

3. COORDINATE MEASUREMENT AND PHOTOMETRY OF PLATE STARS

We measured the Cartesian coordinates of 4963 stars down to $B = 19.25^m$ on plate no. 1824 within a circle of radius 9 cm centered on the cluster center using the ASCORECORD measuring machine at the Institute of Astronomy of the Academy of Sciences of Bulgaria, to an average accuracy of ± 0.05 mm.

We measured the Cartesian coordinates and B magnitudes of 21 374 stars down to $B = 21.5^m$ on plate no. 1846 within a circle of the same radius using the ASCOIRIS iris photometer at the National

1063-7729/02/4603-0182$22.00

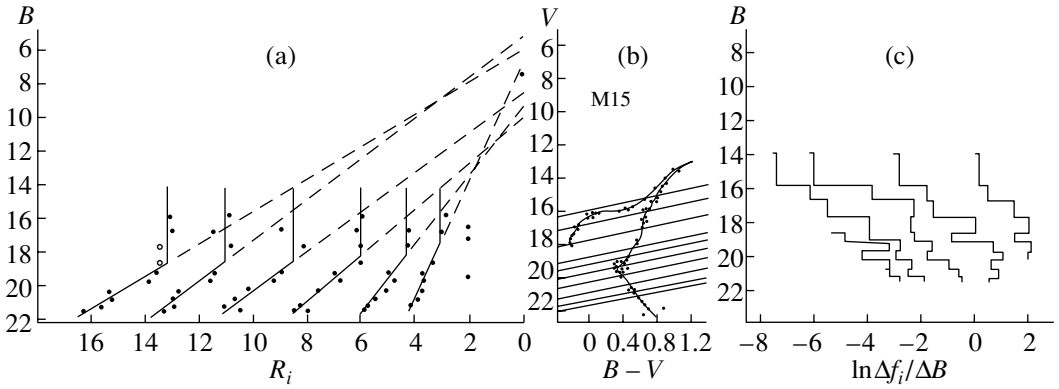

Fig. 1. (a) $B-R_i$, (b) $V, B-V$, and (c) $B-\ln(\Delta f_i/\Delta B)$ diagrams for the globular cluster M15 (R_i is in arcmin and Δf_i in mag/arcmin^3).

Astronomical Observatory of Bulgaria. We used the photographic calibration of Sandage [10]. The measured coordinates are accurate to ±0.05 mm; Table 1 gives the mean accuracy of the measured B magnitudes as a function of distance r from the cluster center for various ΔB intervals. We did not consider the central region of the cluster, where star images overlap and cannot be resolved.

4. DIFFERENTIAL AND INTEGRATED DISTRIBUTIONS OF THE APPARENT AND SPATIAL STELLAR DENSITY

We used the measurements for plate no. 1846 and the technique of Kholopov [8, 9] (assuming spherical symmetry) to compute the following apparent stellar density distributions as a function of the distance r, which we determined as the arithmetic mean of the coordinates of all stars measured.

(a) Differential curves $\Delta F(r,\varphi,\Delta B)$, obtained in eight 90-degree projected radial sectors of the cluster. The sectors are rotated by 45° in azimuth φ relative to each other, so they include stars in different directions from the cluster center with B magnitudes within the intervals $B<15.78^m$, $B=15.78$–16.68^m, 16.68–17.68^m, 17.68–18.68^m, 18.68–19.18^m, 19.18–19.68^m, 19.68–20.18^m, 20.18–20.68^m, 20.68–21.18^m, and 21.18–21.5^m.

(b) Differential curves $\Delta F(r,\Delta B)$ averaged over all directions from the cluster center and determined for the same B-magnitude intervals.

(c) Integrated curves $F(r,B)$ averaged over all directions and including stars down to the limiting magnitudes $B=16.68$, 17.68, 18.68, 19.18, 19.68, 20.18, 20.68, 21.18, and 21.5^m.

All ΔB intervals and limiting B magnitudes are shown by straight lines in the $(V,B-V)$ diagram for M15 (Fig. 1) adopted from [10]. Some $\Delta F(r,\Delta B)$ curves are shown in Fig. 2. The vertical error bars indicate the scatter in the data derived by assuming a Poisson distribution of stars in each zone [9]. The density F is in stars/arcmin^2 and the radius r in arcmin. None of the curves reaches the cluster center, since the plate image of the center cannot be resolved into individual stars.

We used our measurements of plate no. 1824 and the same method to construct integrated $F(r,\varphi,B)$ and $F(r,B)$ curves for all cluster stars down to $B<19.25^m$. Figure 3 shows the $F(r,B)$ curve using the same units as in the previous case. This curve is in satisfactory agreement with the corresponding $F(r,B)$ curve for $B<19.18^m$ based on plate no. 1846 for $r>4'$; the two curves show some systematic differences at $r<4'$, which are due to the higher photometric errors in the central part of the cluster on the second plate, where the higher background

Table 1. Average errors of B stellar photometry

ΔB	r		
	2.0–3.5′	3.5–4.5′	4.5–18.0′
$<15.78^m$	$\pm0.3^m$	$\pm0.10^m$	$\pm0.10^m$
15.78–16.68	0.3	0.10	0.10
16.68–17.68	0.3	0.10	0.10
17.68–18.68	0.4	0.10	0.10
18.68–19.18	0.4	0.10	0.10
19.18–19.68	0.4	0.10	0.10
19.68–20.18	0.4	0.15	0.10
20.18–20.68	0.4	0.15	0.10
20.68–21.18	–	0.20	0.10
21.18–21.50	–	–	0.20

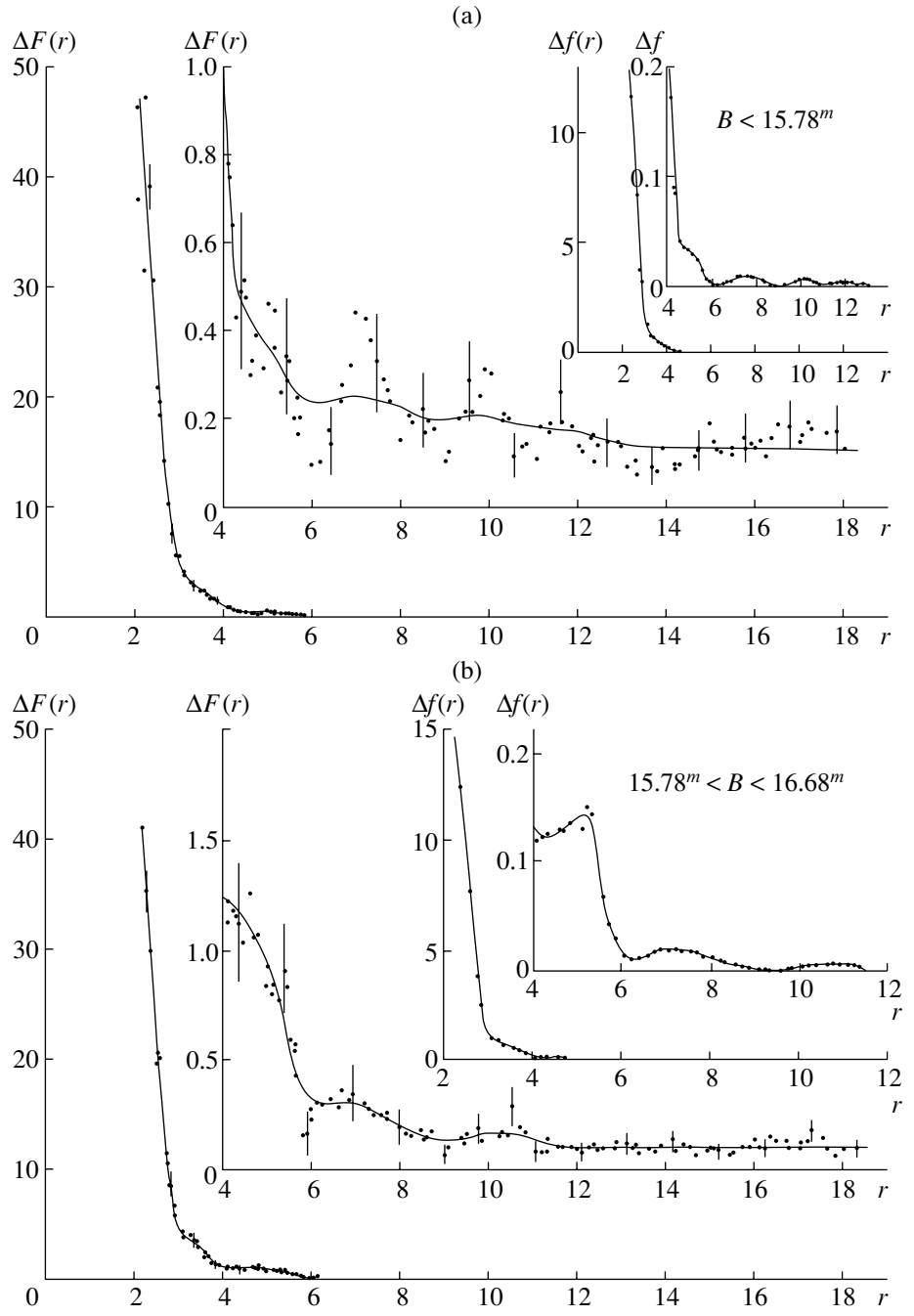

Fig. 2. Differential curves of the apparent and spatial stellar density in the globular cluster M15 for various B-magnitude intervals. See text for units.

density makes it difficult to correct for it using the Weaver method.

Figure 4 shows contours of the differential apparent stellar density derived from $\Delta F(r, \varphi, \Delta B)$. The contours (stars/arcmin^2) increase in multiples of four and correspond to the excess above the mean density $\Delta F_\phi(\varphi, \Delta B)$ in the given direction (Figure 4 shows the densities of field stars in square regions). A comparison of all the apparent stellar density contours reveals systematic deviations from sphericity in the cluster corona, primarily for subsystems of bright stars. These deviations are associated with statistical fluctuations due to the small number of stars in the corona and they decrease with increasing B. We have observed a similar pattern in various other clusters [4, 5], as have other authors.

When computing the differential and integrated stellar spatial distributions $\Delta f(r, \Delta B)$ and $f(r, B)$,

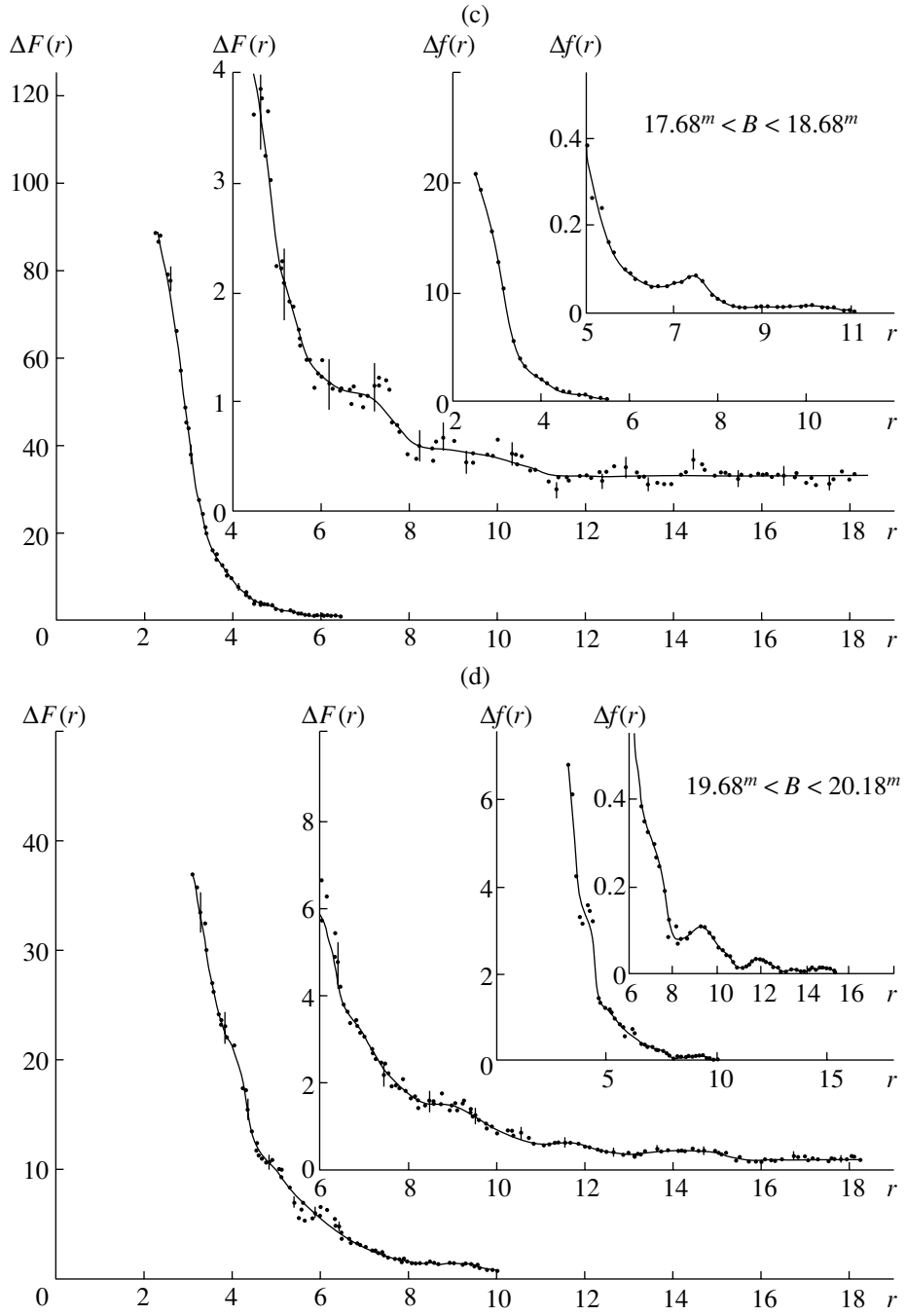

Fig. 2. (Contd.)

we took the cluster radius R_c for each $\Delta F(r, \Delta B)$ and $F(r, B)$ curve to be the horizontal coordinate of the intersection of this curve with the corresponding mean apparent density of field stars $\Delta\overline{F}_\phi$ or $\overline{F}_\phi$. Table 2 lists the radii (in arcmin) determined in this way and averaged over all directions ($R_c = R_7$). We derived $\Delta f(r, \Delta B)$ and $f(r, B)$ from the corresponding $\Delta F(r, \Delta B)$ and $F(r, B)$ using the numerical technique of Kholopov [9] ($a = 1$, spherical symmetry). Figures 2 and 3 show some of the $\Delta f(r, \Delta B)$ curves (in stars/arcmin^3).

5. ANALYSIS OF THE STELLAR DENSITY DISTRIBUTIONS

5.1. Spatial Zones in the Cluster Structure

The ΔF, F, Δf, and f curves can be used to fairly confidently identify six spatial zones in the clus-

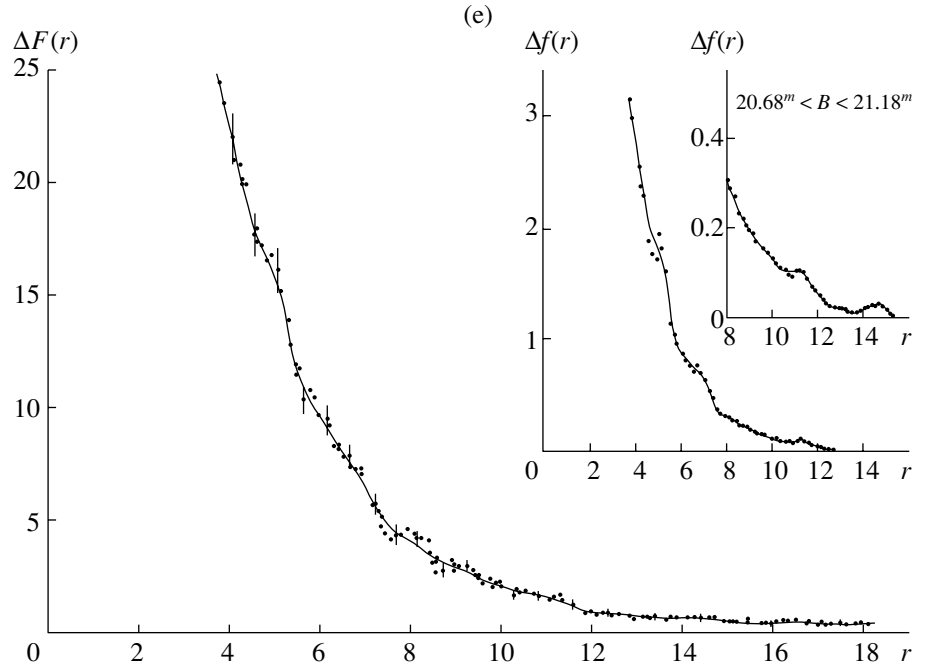

Fig. 2. (Contd.)

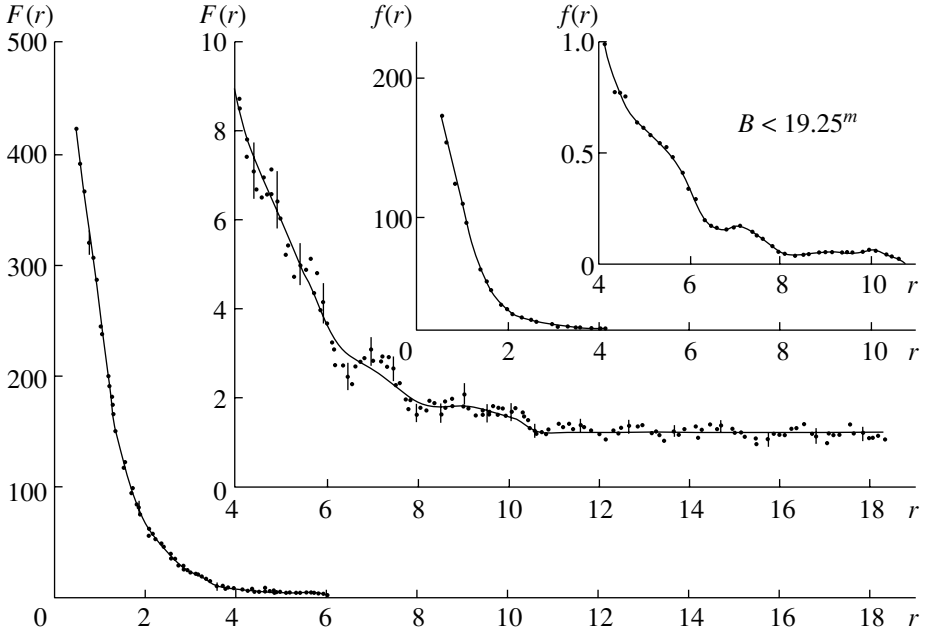

Fig. 3. Integrated curves of the apparent and spatial stellar density distributions in M15 to limiting magnitude $B = 19.25^m$, based on plate no. 1824. See text for the units.

ter such that the density gradient remains approximately constant or varies only slightly within each zone and changes rapidly at the boundary between zones. These zones are listed below in order of increasing distance from the cluster center, in accordance with the terminology of Kholopov [9, 11].

Zone II. Inner core of radius R_2. This is the region with the fastest decrease of stellar density. The radius inferred from the F and f curves for $B < 19.25^m$ based on plate no. 1824 is $R_2 \approx 2'$, whereas the radius inferred from the F and f curves for $B < 19.18^m$ based on plate no. 1846 is $R_2 \approx 3'$. This discrepancy is due to the poor agreement of the curves based on the two different plates in the central region of the

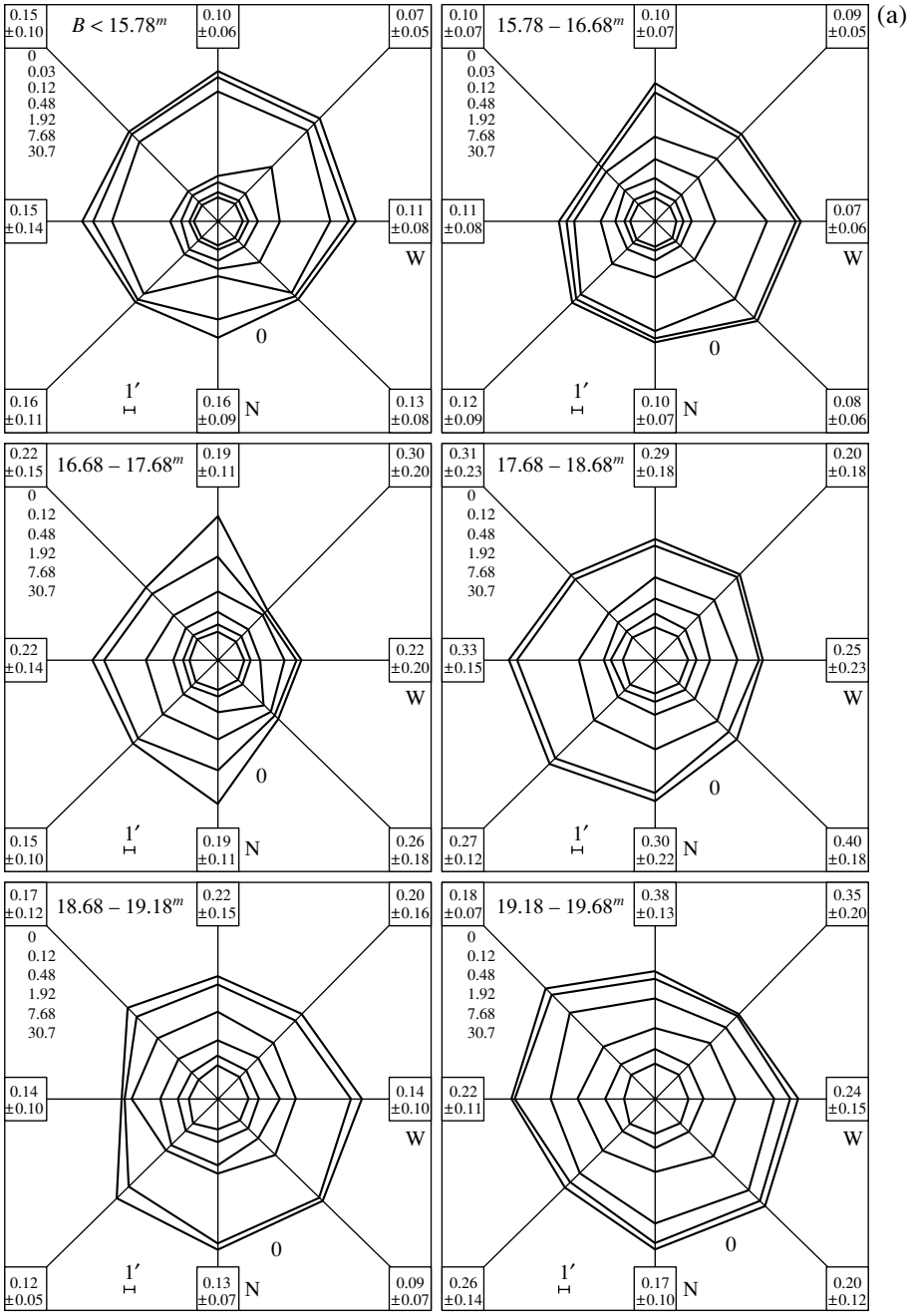

Fig. 4. Contours of differential apparent stellar density in M15 normalized to the corresponding density of field stars. The B-magnitude intervals, contour levels, field-star density and dispersion (within square regions), and the directions North and West are indicated.

cluster, at $r < 4'$. We believe that the first R_2 value is closer to the real value. Moreover, Kholopov [11] also gives $R_2 \approx 2'$ for bright-star subsystems to limiting magnitudes $m_{\rm pg} \leqslant 16.6^m$ and $m_{\rm pg} \leqslant 7.3^m$ (see Fig. 5 below).

Zone III. Outer core region of radius R_3, defined as the boundary between the core and the corona.

Zone IV. Inner corona of radius R_4, characterized by a slow decrease in the stellar density.

Zones V and VI. Intermediate corona zones with radii R_5 and R_6, with fairly slow decreases in density.

Zone VII. Outer corona of radius R_7, which we adopt as the cluster radius $R_{\rm c}$.

In some cases, these last two zones are difficult or impossible to identify for some stellar subsystems in some directions, due to weak variation of the zone-to-zone density gradient and fluctuations in the corona region.

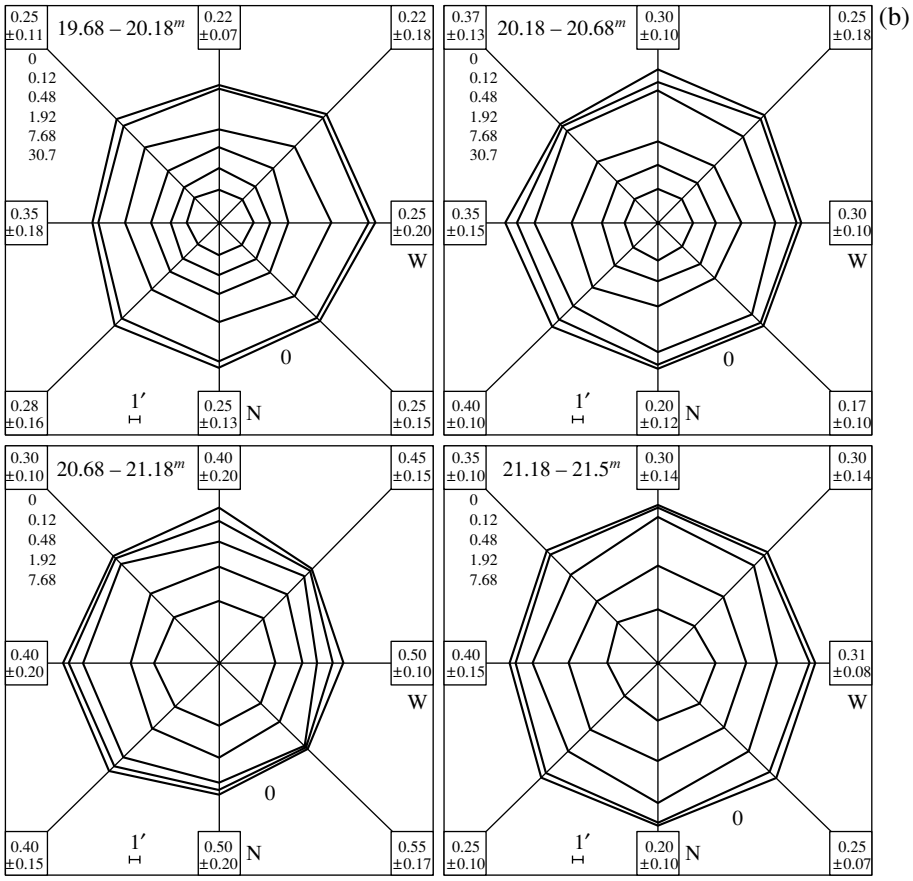

Fig. 4. (Contd.)

Since our density curves do not reach the cluster center, it is impossible to identify the first central core zone of radius R_1. Kholopov [11] gives $R_1 = 0.5'$, derived for a subsystem of stars to limiting magnitude $m_{\rm pg} \leqslant 16.6^m$.

Table 2 gives the mean radii R_i (i is the zone number) together with their standard deviations (in arcmin). A colon indicates data that are uncertain due to the smaller number of estimates used. Figure 5 compares radii the R_i for each zone with the corresponding B limiting magnitudes for stars of the given subsystem. The table gives the radii R_i (in arcmin and pc), as well as the apparent B band magnitudes and absolute magnitudes M_B. We have adopted the cluster distance $r_{\rm c}$, distance modulus $\mathrm{Mod}_{\rm app}V$, and color excess E_{B-V} from the catalog of Kukarkin [17].

5.2. Layered Structure of M15

Another interesting feature that we established by analyzing ΔF and Δf curves is that the densities in the inner parts of most of the zones lie above the mean-gradient curve, while the opposite is true at the zone boundaries. This situation is manifest as steps and waves in the curves in Fig. 2. The effect can be seen most clearly near the cluster corona and is gradually washed out in the transition toward fainter B magnitudes (i.e., with an increase in the number of stars). Kholopov [9] has also noted this same phenomena in other clusters.

At the same time, the width of each zone $\Delta R_i = R_i - R_{i-1}$ ($i = 3, ..., 7$) remains approximately constant or increases slightly toward outer zones (Fig. 5) for each stellar subsystem. The only exceptions are the first and second zones (R_1, R_2), whose widths are almost half those of the other zones. This is due to the fact that R_1 is the only point defined as the location where the outward density gradient df/dr abruptly increases [9], whereas the other R_i are defined as points where df/dr decreases. The central zone of the core can therefore be considered to be only the first half of the inner core zone, with the two halves together making up the entire zone.

The above considerations lead us to suggest that, in some sense, M15 possesses a layered structure in which the individual layers correspond to the spatial zones indicated above. Other clusters that we have observed [1–6] exhibit similar structures.

Table 2. Radii of spatial zones in M15

B	ΔB	R_2	R_3	R_4	R_5	R_6	R_7
15.78^m	$<15.78^m$	$2.81' \pm 0.17'$	$4.28' \pm 0.27'$	$6.02' \pm 0.26'$	$8.73' \pm 0.42'$	$10.96' \pm 0.41'$	$13.15' \pm 0.38'$
16.68	15.78–16.68	2.98 ± 0.18	4.18 ± 0.28	6.14 ± 0.50	8.96 ± 0.25	11.47 ± 0.32	13.1: –
17.68	16.68–17.68	3.04 ± 0.09	4.30 ± 0.31	6.01 ± 0.72	8.07 ± 0.61	10.79 ± 0.62	13.4: –
18.68	17.68–18.68	3.29 ± 0.22	4.39 ± 0.28	5.99 ± 0.40	8.38 ± 0.32	10.99 ± 0.46	13.5: –
19.18	18.68–19.18	3.68 ± 0.30	4.96 ± 0.39	6.98 ± 0.49	8.95 ± 0.53	11.44 ± 0.48	13.58 ± 0.25
19.25	–	1.96 ± 0.24	3.93 ± 0.47	5.95 ± 0.50	8.39 ± 0.56	11.33 ± 0.49	13.6: –
19.68	19.18–19.68	3.64 ± 0.08	4.72 ± 0.40	6.76 ± 0.81	9.20 ± 0.59	11.54 ± 0.39	13.88 ± 0.44
20.18	19.68–20.18	3.66 ± 0.10	5.03 ± 0.35	7.54 ± 0.36	10.16 ± 0.68	12.77 ± 0.51	15.37 ± 0.49
20.68	20.18–20.68	3.86 ± 0.32	5.41 ± 0.26	7.90 ± 0.58	10.69 ± 0.45	12.94 ± 0.52	15.17 ± 0.45
21.18	20.68–21.18	4.1: –	5.71 ± 0.25	8.25 ± 0.47	11.04 ± 0.65	12.89 ± 0.60	15.61 ± 0.33
21.50	21.18–21.50	4.2: –	5.85 ± 0.25	7.93 ± 0.20	10.40 ± 0.35	13.28 ± 0.26	16.25 ± 0.55

Table 3. Structural parameters of M15

i	$\tilde{r}_i$	a_i	b_i	B_{0i}	$B_{\mathrm{lim},i}$
1	0.079	–	–	–	–
2*	$0.334^* \pm 0.035$	–	–	–	–
2	0.499 ± 0.043	0.281 ± 0.043	1.88 ± 0.86	$6.69^m \pm 4.08$	17.50^m
3	0.696 ± 0.037	0.485 ± 0.050	4.62 ± 1.01	9.53 ± 3.06	18.35
4	1.0–	0.732 ± 0.075	7.40 ± 1.52	10.11 ± 3.11	18.35
5	1.418 ± 0.081	0.859 ± 0.085	7.51 ± 1.71	8.74 ± 2.86	18.65
6	1.759 ± 0.125	0.827 ± 0.072	4.39 ± 1.46	5.31 ± 2.23	18.65
7	2.045 ± 0.142	1.052 ± 0.090	6.44 ± 1.84	6.12 ± 2.27	18.70
$A = 0.547 \pm 0.042$		$B_0 = 7.43^m \pm 0.92$		$\overline{B}_{\mathrm{lim}} = 18.54^m \pm 0.26$	

* Asterisk indicates a value derived from measurements of plate no. 1824.

5.3. Dependence of the Cluster Radius and Zones on Limiting Magnitude

The first manifestation of the systematic variation of the spatial structure of M15 is an increase of the radii of the zones and of the cluster itself R_i in the transition toward fainter B magnitudes. It is evident from Table 2 and Fig. 5 that, beginning with $B = 14^m$ (the magnitude of the brightest cluster stars, shown by the vertical dashed line in Fig. 5) and continuing to $B = \overline{B}_{\mathrm{lim}} = 18.54^m \pm 0.26^m$, the zone radii remain virtually constant ($R_i(B) = \mathrm{const}$), while they systematically increase at $B > \overline{B}_{\mathrm{lim}}$. This increase is stronger for the outer than for the inner layers. A comparison with the $(V, B-V)$ diagram (Fig. 1) shows that the limiting magnitude $\overline{B}_{\mathrm{lim}}$ at which $R_i(B)$ begins to change corresponds to the transition region between the subgiant branch and the MS turnoff, in agreement with our earlier results [1–6].

Following our technique [1–6], we obtained a least-squares fit to the systematic behavior of $R_i(B)$ as a function of B at $B > \overline{B}_{\mathrm{lim}}$ using the linear relationship

$$R_i = a_i B - b_i = a_i(B - B_{0i}), \quad i = 2, ..., 7,$$

where a_i, b_i, and $B_{0i} = b_i/a_i$ are constant for the ith radius; we then computed the relative zone radii $\tilde{r}_i = R_i(B)/R_4(B)$ normalized to $R_4(B)$. Table 3 lists a_i, b_i, B_{0i}, and $\tilde{r}_i$. The parameter $\tilde{r}_1$ was derived from the data of Kholopov [11], and the asterisk indicates a value based on plate no. 1824. We found the limiting B magnitudes to be approximately the same within the quoted errors for all $\tilde{r}_i$, $\tilde{r}_i(B) \approx \mathrm{const}$. In

Table 4. Differential and integrated stellar spatial density function near the boundaries of zones of M15

ΔB	Δf_2	Δf_3	Δf_4	Δf_5	Δf_6	Δf_7	$\Delta N\,(r > 4')$
$14.00-15.78^m$	2.0	0.100	0.004	0.001	0.003	0	58
15.78–16.68	1.4	0.144	0.020	0.002	0	–	108
16.68–17.68	4.5	0.215	0.100	0.004	0	–	179
17.68–18.68	7.4	1.00	0.090	0.020	0	–	409
18.68–19.18	2.2	0.20	0.050	0.010	0.004	0	481
19.18–19.68	4.0	1.00	0.100	0.030	0.020	0	993
19.68–20.18	3.6	1.50	0.085	0.025	0.007	0	1742
20.18–20.68	–	0.93	0.20	0.050	0.020	0	2372
20.68–21.18	–	1.20	0.29	0.040	0.020	0	2685
21.18–21.50	–	0.53	0.20	0.050	0.020	0	2029
B	f_2	f_3	f_4	f_5	f_6	f_7	$N\,(r > 4')$
16.68^m	3.2	0.230	0.017	0.005	0.005	0	166
17.68	6.7	0.470	0.090	0.015	0	–	345
18.68	15.0	1.40	0.160	0.020	0	–	754
19.18	25.0	2.00	0.290	0.080	0.015	0	1235
19.68	10.0	1.13	0.240	0.060	0.030	0	2228
20.18	19.0	1.50	0.320	0.080	0.013	0	3970
20.68	25.0	3.20	0.40	0.120	0.050	0	6342
21.18	–	4.20	0.65	0.170	0.070	0	9027
21.50	–	5.75	1.10	0.270	0.080	0	11056

other words, to a first approximation, the increase of $R_i(B)$ with B is homologous. As before [1–6], we will refer to such a cluster as a homologous cluster. The homologous structure of M15 may break down somewhat in the last two zones (nos. 6, 7; Fig. 5) for reasons that remain unclear.

Applying the least-squares technique to the a_i and b_i from Table. 3, we can find the value of B_0 for a homologous cluster:

$$b_i = B_0 a_i, \quad B_0 = 7.43^m \pm 0.92^m.$$

We obtain in absolute magnitudes (in accordance with [17]) $M_{B_0} = -7.88^m$.

We also derived the following empirical relation based on the data in Table 3:

$$a_i = A\tilde{r}_i,$$

where $A = \text{const}$. Table 3 gives the least-squares-fit value of the parameter A.

Finally, we derive a single relation for the size of the homologous cluster structure:

$$R = A\tilde{r}(B - B_0), \quad B > \overline{B}_{\text{lim}}$$

for arbitrary B and arbitrary relative distance $\tilde{r}$ from the center of the system. It remains unclear to what limiting magnitudes this relation can be extrapolated.

5.4. Dependence of the Spatial Stellar Density near the Zone Boundaries on Limiting B Magnitude

This is the second manifestation of the variation of the spatial structure of the cluster as a function of B magnitude. We determined the corresponding $f(R_i(B), B)$ and $\Delta f(R_i(B), \Delta B)$ (or equivalently $f(\tilde{r}_i, B)$, $\Delta(\tilde{r}_i, \Delta B)$) near the boundaries of the spatial zones (in stars/arcmin^3) for all limiting B magnitudes and Δ intervals based on the data for $R_i(B)$ and the f and Δf curves; the results are presented in Table 4. We also list the numbers of stars $N(B)$ and $\Delta N(\Delta B)$ in the cluster and its subsystems for $r > 4'$, which are statistically free of contamination by field stars. Figure 6 shows the $\ln[\Delta f(R_i(B), \Delta B)/\Delta B]$ dependences, $i = 2, ..., 7$ for the corresponding zones, as well as $\ln[\Delta N(\Delta B)/\Delta B]$ (with f in stars/arcmin^3 and stars/pc^3).

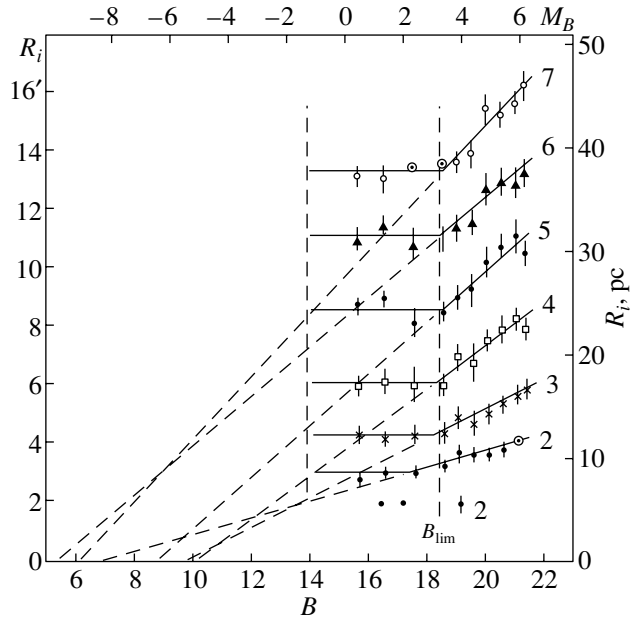

Fig. 5. Dependence of the zone radii for M15 on limiting magnitude. The zone number $i = 2$–7 is indicated.

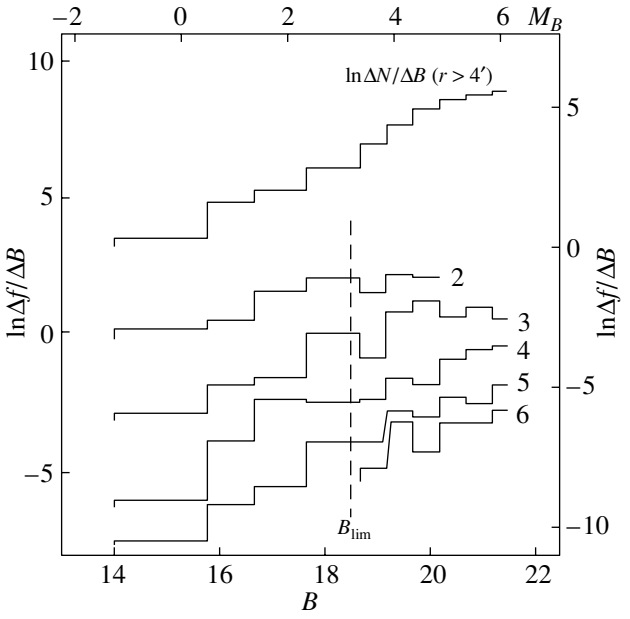

Fig. 6. Magnitude dependence of the total number of stars in M15 and of the differential stellar density at the boundary of each zone at $r > 4'$. The zone number $i = 2$–6 is indicated. (The left and right scales give Δf_i in stars/arcmin^3 and stars/pc^3, respectively.)

The function $f(R_i(B), B)$ can be considered the integrated luminosity function of M15, and $\Delta f(R_i(B), \Delta B)$ the differential luminosity function as a function of relative distance from the cluster center $\tilde{r}$, which is statistically free of the effects of field stars and of the projection of outer regions of the cluster onto inner ones. A comparison of the $\ln(\Delta f/\Delta B)$ histograms in Fig. 6 shows that here, too, we can see a systematic change in the cluster structure at $B > \overline{B}_{\rm lim}$. The mean logarithmic slopes $\dfrac{\partial}{\partial B}\left(\ln\dfrac{\Delta f(R_i(B), \Delta B)}{\Delta B}\right)$ at $B < \overline{B}_{\rm lim}$ are approximately constant for the different zones (i.e. for different $\tilde{r}_i$), whereas at $B > \overline{B}_{\rm lim}$ they increase systematically toward outer cluster zones. We conclude that the rate of increase in the number of faint stars near and below the MS turnoff is lowest in the cluster core and highest in the cluster corona. This means that faint stars are less concentrated toward the center of M15. Moreover, at $B > \overline{B}_{\rm lim}$, the cluster luminosity function itself depends on distance from the center.

6. RESULTS AND DISCUSSION

The principal manifestations of the systematic variation of the spatial structure of M15 as a function of limiting magnitude are illustrated in Fig. 1. We can see that the spatial structure of the cluster remains nearly constant above the transition region between the subgiant branch and MS turnoff, but changes systematically below this region. The radii of zones and of the cluster as a whole increase in accordance with a single law, as does the stellar density distribution in the cluster. These results are similar to those obtained earlier for other clusters [1–6].

The absence of systematic variations of the cluster structure for $B < \overline{B}_{\rm lim}$ is due to observational selection effects: we cannot observe stars with lower masses, which were located far above the present-day turnoff point when they lay on the ZAMS and have now evolved into the domain of white dwarfs and neutron stars. The cluster stars that are now observed above the MS turnoff have masses approximately equal to those of stars located near the turnoff point (i.e., their progenitors) and therefore maintain their spatial distribution. This is why the cluster displays no structural changes at $B < \overline{B}_{\rm lim}$.

Following our ideas expressed in [1–6], we suggest that the change in the structure of M15 observed at $B > \overline{B}_{\rm lim}$ is due to changes in the mean masses of stars located near or below the MS turnoff point on the $(V, B-V)$ diagram, in accordance with the mass–luminosity relation.

As in our earlier studies, we consider the observed systematic change of the cluster structure to have its origin in processes occurring during the formation of the cluster from the interstellar medium, not in the cluster's subsequent dynamic evolution due to stellar

encounters and dissipation. Support for this view can be found in King's formula for the cluster relaxation time

$$\tau = 0.35\sqrt{N\overline{R}^3/mG}/\ln(N/2),$$

which yields for M15 $\tau \approx 40.10^9$ yr (for the mean mass of a cluster star m, total cluster mass M_c, and half-mass radius $\overline{R}$ from [18]), which exceeds the age of the cluster. In addition, the structural change is especially prominent in the corona rather than the cluster core, where the effects of dynamic evolution are minimal. We suggest that, after the formation of the cluster, its subsequent dynamic evolution tends to disrupt rather than create the observed structural changes.

In view of all the above considerations, we suggest that, physically, the parameter B_0 (and, accordingly, M_{B_0}, the magnitude at which the radii of the zones and of the cluster would become zero if the $R_i(B)$ relation were extrapolated to $B < \overline{B}_{\rm lim}$, see above) represents the magnitude of the brightest stars of the cluster immediately after its formation. We also note in conclusion that the structural changes studied in this and our earlier papers are observed in clusters with different parameters and so must represent common behavior for most of these objects.

REFERENCES

1. R. M. Rusev and Z. I. Peĭkov, Astron. Zh. **63**, 483 (1986) [Sov. Astron. **30**, 288 (1986)].
2. Z. I. Peĭkov and R. M. Rusev, Astron. Zh. **65**, 41 (1988) [Sov. Astron. **32**, 21 (1988)].
3. Z. I. Peĭkov and R. M. Rusev, Astron. Zh. **65**, 317 (1988) [Sov. Astron. **32**, 161 (1988)].
4. Z. I. Peĭkov and R. M. Rusev, Astron. Zh. **67**, 694 (1990) [Sov. Astron. **34**, 349 (1990)].
5. Z. I. Peĭkov and R. M. Rusev, Astron. Zh. **76**, 514 (1999) [Astron. Rep. **43**, 445 (1999)].
6. Z. I. Peĭkov and R. M. Rusev, Astron. Zh. **76**, 571 (1999) [Astron. Rep. **43**, 494 (1999)].
7. Z. I. Peĭkov, Astron. Zh. **67**, 1141 (1990) [Sov. Astron. **34**, 575 (1990)].
8. P. N. Kholopov, Astron. Zh. **30**, 426 (1953).
9. P. N. Kholopov, *Star Clusters* (Nauka, Moscow, 1981).
10. A. R. Sandage, Astrophys. J. **162**, 841 (1970).
11. P. N. Kholopov, Astron. Zh. **40**, 523 (1963) [Sov. Astron. **7**, 399 (1963)].
12. I. R. King, Astron. J. **67**, 471 (1962).
13. I. Lehmann and R. D. Scholz, Astron. Astrophys. **320**, 776 (1997).
14. S. C. Trager, I. R. King, and S. Djorgovski, Astron. J. **109**, 218 (1995).
15. G. Piotto, A. M. Cool, and I. R. King, Astron. J. **113**, 1345 (1997).
16. C. Sosin and I. R. King, Astron. J. **113**, 1328 (1997).
17. B. V. Kukarkin, *Globular Star Clusters* (Nauka, Moscow, 1974).
18. G. Mandushev, N. Spassova, and A. Staneva, Astron. Astrophys. **252**, 94 (1991).

Translated by A. Dambis

Astronomy Reports, Vol. 46, No. 3, 2002, pp. 193–205. Translated from Astronomicheskiĭ Zhurnal, Vol. 79, No. 3, 2002, pp. 216–228.

A Catalog of Star-Forming Regions in the Galaxy

V. S. Avedisova

Institute of Astronomy, Russian Academy of Sciences, Pyatnitskaya ul. 48, Moscow, 109017 Russia

Received May 5, 2001

Abstract—This Catalog of Star-Forming Regions in the Galaxy contains coordinates and fluxes of young objects in the radio and infrared, as well as data on the radial velocities of recombination and molecular lines, for more than three thousand star-forming regions. In addition to photometric and kinematic data, we present information on diffuse and reflecting nebulae, dark and molecular clouds, and other objects related to young stars. The catalog consists of two parts. The main catalog lists star-forming regions in order of Galactic longitude and is supplemented by analogous information for star-forming regions in complexes of dark clouds with large angular sizes that are closest to the Sun. The main catalog is located at www.strasbg.-u.fr/pub/cats. In our preliminary study of the catalog data using a formal classification of the star-forming regions, we subdivided these objects into several classes and characterized them as being populated primarily by massive or low-mass stars at early or late stages of the star-formation process. We also distinguish between relatively nearby and distant complexes. © *2002 MAIK "Nauka/Interperiodica"*.

1. INTRODUCTION

Studies of star-forming regions (SFRs) began with the discovery of compact H II regions in the late 1960s [1, 2], received a strong push from the IRAS infrared survey [3], and made further progress thanks to improvements in observations of interstellar masers [4]. In SFRs, we observe young stars, protostars, and related objects and phenomena. These include H II regions, IR sources with negative spectral indices ($S \sim \nu^{\alpha}$), pre-main-sequence stars with IR excesses, non-stellar maser sources, reflecting nebulae in complexes of dark clouds, Herbig–Haro objects, and hot spots in molecular clouds. A SFR can include objects of any combination of these types. There is extensive literature on SFRs. In addition to multifaceted and detailed studies of individual SFRs, many surveys of the Galactic plane in the optical, infrared, submillimeter, millimeter, and radio have been published. However, no master list of such regions with their principal observational characteristics has been compiled.

The "Catalog of Star-Forming Regions in the Galaxy" described here (hereafter, simply "the catalog") is a list of Galactic SFRs along with a compilation of observational data on young objects in SFRs extracted from scientific journals and other catalogs. The catalog contains about 3300 SFRs and candidate SFRs, which include about 4000 IRAS sources, 500 hydroxyl masers, 700 water masers, and 700 methanol masers. The catalog also presents SFRs in dark-cloud complexes closest to the Sun, where stars of low and intermediate masses are primarily formed. It is difficult to evaluate the catalog's completeness, and we can only note that nearly all large surveys in the radio, infrared, submillimeter, and millimeter published by 1998 were included. This level of completeness was not achieved for individual SFRs.

Section 2 presents the contents of the catalog and describes its structure and format. Section 3 discusses techniques used to include observational data in the catalog and some criteria for the identification of individual sources and their assignment to SFRs. Section 4 presents a formal classification of the catalog objects and our preliminary conclusions about the physical nature of the resulting classes.

2. DESCRIPTION OF THE CATALOG

The catalog contains the following observational data: (a) photometric and kinematic characteristics of SFRs in the radio and infrared, (b) principal data on optical and dark nebulae and molecular clouds related to SFRs (coordinates, sizes, velocities), and (c) radiation fluxes and radial velocities of nonstellar maser sources (OH, H_2O, methanol (CH_3OH), etc.). The photometric data include continuum radio fluxes from H II regions formed by massive stars, stellar winds, or accretion shock waves in low-mass stars, as well as IR fluxes from the dust components of cocoons and disk structures around young stars or the dense cores of molecular clouds heated by these stars. The kinematic data include the radial velocities of recombination lines in H II regions and of numerous interstellar molecular lines in circumstellar disks and progenitor clouds.

1063-7729/02/4603-0193$22.00

The catalog consists of the main catalog, a supplement, and appendices. The supplement presents information similar to that of the main catalog for SFRs in dust–cloud complexes closest to the Sun, covering many degrees on the sky. The appendices include references, a short list of sources, and a table of source names and positions. The volume of the catalog exceeds 13 Mbytes.

2.1. Main Catalog

The main catalog is available at www.strasbg.-u.fr/pub/cats; a fragment is shown in Table 1. All SFRs and their subsystems are ordered according to increasing Galactic longitude. The first column gives the source's Galactic coordinates, treated as an "*lb*-name" of the source. The second column contains the Galactic coordinates of SFR subsystems and sources at all wavelengths. The third column gives a code for the type of data: D—data on dark nebulae and globules; O—optical data; R—radio data for continuum fluxes and velocities of recombination lines; IR—infrared data; M—data on molecular lines, including maser sources. The fourth column presents the source name corresponding to the given type of data (O, R, IR, D); for M data, the name of the molecule is also indicated. The fifth column contains the source designation in the original reference or the object type; a morphological description, such as 'ridge' 'core', 'halo', 'envelope', 'cloud', or 'globule', or a comment, such as 'diff. emission', 'peak', or 'outflow', may appear here. For ultracompact H II regions, the R data may give the morphological class of the H II region: $\langle CH\rangle$ (core–halo), $\langle SH\rangle$ (shell), $\langle I\rangle$ (irregular), $\langle SP\rangle$ (spherical), $\langle C\rangle$ (cometary), $\langle U\rangle$ (unresolved), $\langle MP\rangle$ (multiple peaks), $\langle AL\rangle$ (arch-like), $\langle P\rangle$ (partially extended), $\langle D\rangle$ (double peak), $\langle G\rangle$ (Gaussian). For IRAS sources associated with low-mass stars, the evolutionary type of the young object according to [5, 6] may be given: $\langle 0\rangle$ (class 0), $\langle 1\rangle$ (class 1), $\langle 2\rangle$ (class 2), $\langle 3\rangle$ (class 3). The sixth and seventh columns contain the right ascension and declination (1950.0). The eighth column presents the frequency in GHz for R and M data and the wavelength in μm for IR and O data. The ninth column presents the flux density in Jy for R and IR data; for masers, it gives the peak flux density in Jy or, if a square bracket "[" precedes the flux value, the integrated flux in Jy km s^{-1}. The tenth and eleventh columns give the size of the source or/and of the beam; the latter case is indicated by an asterisk after the unit of measurement. The twelfth column presents the central radial velocities of lines V_c relative to the local standard of rest (LSR, with the Sun's velocity towards the apex being 20 km/s) and the line widths in km/s. If several radial velocities are observed, they are separated by commas. The line widths follow the corresponding velocities and are separated from them by semicolons. If multiple overlapping velocities are observed, lower and upper limits for the velocity ranges are given, separated by a forward slash. The thirteenth column gives a bibliographic reference code. Galactic-center sources are presented at the end of the catalog, separate from the general list of SFRs.

The vast majority of sources have a small number of observations. For example, for more than a thousand SFRs, the observations are summarized in only five rows, four of them usually corresponding to the four IRAS bands. In the course of further detailed studies, it may become possible to merge many of these SFRs with one another or with other SFRs. More than ten rows are given for more than 1200 SFRs. For 80 SFRs, the number of rows exceeds 100, and for 12 SFRs, it exceeds 400. Well-studied extended SFRs show hierarchical structure: they consist of several subsystems that may consist of smaller subsystems, and so forth.

2.2. Supplement

Data on SFRs in extended cloud complexes closest to the Sun are presented in the supplement, which consists of 17 files with a format similar to that of the main catalog. The same complexes also appear in the main catalog, but only under the names of their principal components.

The supplement includes 15 extended cloud complexes within 1000 pc of the Sun: (1) the Canis Major complex, (2) the Cepheus complex (Cepheus Flare), (3) the Chamaeleon complex, and (4) the Coalsack, (5) the Corona Australis complex, (6) the Gum Nebula, (7) the Lupus complex, (8) the Norma cloud, (9) the Ophiuchus complex, (10) the Orion complex, (11) the Perseus complex, (12) the Serpens cloud, (13) the Taurus and Auriga complex, and (14) the Vela complex.

2.3. Bibliography

The bibliographic reference code is a five-digit number, with the first two figures corresponding to the year of publication of the original reference and the last three being the number attributed to that paper. The bibliography includes about 5800 references.

2.4. Table of Source Names and Positions

The table of source names and positions is a list of commonly used names of individual sources in the SFRs (in the optical, radio, and IR) in alphabetical order, with the Galactic coordinates of the corresponding SFR indicated. In addition to the names and positions in the first two columns of the file, the

Table 1. Fragment of the Catalog

lb-name	*lb* (source)	Type	Name	Label	RA(1950)	DEC(1950)	ν or λ	F_ν or F_λ	Size	Beam size	Velocity	Reference
1	2	3	4	5	6	7	8	9	10	11	12	13
000.00+0.19		O	RCW138		17 41 42	−28 49 00	0.6563		8	4 ′		6001
	0.02 +0.13	O	S17		17 42 00	−28 50 00	0.6562		8	4 ′	−3.3	70008
		O			17 42 00	−28 50 00	0.6563			2 ′*	−5.5; 36.3	90032
	359.98 +0.15	R		S8	17 41 49.7	−28 50 40	4.750	$0.420E+0$	2.9	2.5 ′		89061
		R		S8	17 41 51.5	−28 50 57	10.700	$0.650E+0$	2.2	2.8 ′		89061
		R		S8	17 41 49.7	−28 50 40	4.750	$0.340E+0$		2.4 ′*		89061
		R		S8	17 41 51.5	−28 50 57	10.700	$0.150E+0$		1.2 ′*		89061
	0.01 +0.14	IR	FIR26		17 41 54	−28 50 12	69	$0.800E+3$		1.25 ′*		84048
	359.971+0.170	IR	17417−2851		17 41 44.26	−28 50 53.1	100	$0.250E+4$	$\langle T \rangle$			93086
		IR	17417−2851		17 41 44.26	−28 50 53.1	60	$0.658E+3$	$\langle T \rangle$			93086
		IR	17417−2851		17 41 44.26	−28 50 53.1	25	$0.860E+1$	$\langle T \rangle$			93086
		IR	17417−2851		17 41 44.26	−28 50 53.1	12	$0.230E+1$	$\langle T \rangle$			93086
	359.971+0.170	IR	17417−2851		17 41 42.9	−28 51 07	100	$0.177E+4$		1.5 ′*		86012
		IR	17417−2851		17 41 42.9	−28 51 07	60	$0.671E+3$		1.5 ′*		86012
		IR	17417−2851		17 41 42.9	−28 51 07	25	$0.538E+2$		1.0 ′*		86012
		IR	17417−2851		17 41 42.9	−28 51 07	12	$0.107E+2$		1.0 ′*		86012
		M	CS		17 41 42.9	−28 51 07	97.981			50 ″*	−6.0; 2.8	96005
		M	NH_3		17 41 42.9	−28 51 06.9	23.694			40 ″*	−5.6; 1.11	96008
		M	NH_3		17 41 42.9	−28 51 06.9	23.723			40 ″*	−5.5; 1.14	96008
	359.977+0.168	M	H_2O−E		17 41 44.11	−28 50 50.8	22.2	I $0.930E+0$		2 ′*	−8.4, −8.4/−3.1	93086

Table 1. (Contd.)

1	2	3	4	5	6	7	8	9	10	11	12	13
	359.975+0.172	IR		IRS	17 41 44.2	−28 50 54	4.8	$0.965E+0$		9 ″*		88035
		IR		IRS	17 41 44.2	−28 50 54	3.5	$0.248E+0$		9 ″*		88035
		IR		IRS	17 41 44.2	−28 50 54	2.2	$0.205E-1$		9 ″*		88035
		IR		IRS	17 41 44.2	−28 50 54	1.65	$0.155E-2$		9 ″*		88035
000.00−0.18		R		S25	17 43 08.5	−29 00 36	10.700	$0.320E+0$	2.3	1.3 ′		89061
		R		S25	17 43 08.5	−29 00 36	10.700	$0.150E+0$		1.2 ′*		89061
	359.996−0.168	IR	17430−2900		17 43 05.3	−29 00 30	100	$< 0.254E+4$		1.5 ′*		86012
		IR	17430−2900		17 43 05.3	−29 00 30	60	$0.555E+3$		1.5 ′*		86012
		IR	17430−2900		17 43 05.3	−29 00 30	25	$0.118E+3$		1.0 ′*		86012
		IR	17430−2900		17 43 05.3	−29 00 30	12	$0.835E+1$		1.0 ′*		86012
000.01−0.55		O	S18		17 44 36	−29 12 00	0.6563		4 ′			82004
		O			17 44 36	−29 12 00	0.6563			2 ′*	+12.9; 26.5	90032
	0.05 −0.54	R			17 44 39	−29 09 18	22.2	$0.330E+1$	5.3 ′			86050
		M	CO		17 44 09	−29 12 00	115.27			2.0 ′*	+18.8; 3.3	82004
	359.970−0.458	R			17 44 09.22	−29 10 57.7	22	$< 0.500E-1$	$\langle T \rangle$	3 ″*		89009
	359.970−0.459	IR	17441−2910		17 44 09.6	−29 10 58	100	$0.369E+4$		1.5 ′*		86012
		IR	17441−2910		17 44 09.6	−29 10 58	60	$0.174E+4$		1.5 ′*		86012
		IR	17441−2910		17 44 09.6	−29 10 58	25	$0.228E+3$		1.0 ′*		86012
		IR	17441−2910		17 44 09.6	−29 10 58	12	$0.275E+2$		1.0 ′*		86012
	359.970−0.457	M	OH−E		17 44 09.13	−29 10 56.5	1.665	$0.104E+2$		7 ″*	+15.5, +14/+18	98003
		M	OH−E		17 44 09.2	−29 10 57	1.7	$0.130E+2$		5 ″*	+14.5	89009

third column indicates whether the SFR is contained in the main catalog (I) or the supplement (II). In addition to the bibliographic data for the original catalog, the list of references in the table of source names and positions includes the following catalogs and surveys: **BBW**—Galactic emission and reflection nebulae [7], **BHR**—southern Bok globules [8], **CB**—small, optically selected molecular clouds [9], **CTB**—1400 MHz H II regions [10], **DG**—reflection nebulae in the Palomar Sky Survey [11], **DR**—Cygnus X region [12], **DWB**—optically visible H II regions [13], **FIRSSE**—far-infrared sky survey [14], **G**—survey of southern H II regions [15], **GGD**—new Herbig–Haro objects [16], **GL**—dark nebulae and globules for Galactic longitudes 240°–360° [17], **GM**—new and interesting nebulae [18], **GY**—new objects resembling Herbig–Haro objects [19], **HFE**—100-micron survey of the Galactic plane [20], **IC**—2000.0 NGC catalog [21], **KR**—21-cm survey of the Galactic plane between $L = 93°$ and $L = 162°$ [22], **L**—dark nebulae [23], **LkHA**—members and candidate members of the group of Herbig Ae/Be (HAEBE) stars [24], **MWC**—Mt. Wilson catalog [24], **NGC**—2000.0 NGC catalog [21], **RAFGL**—revised catalog of the AFGL IR sky survey [25], **RWC**—Hα regions in the southern Milky Way [26], **RNO**—red and nebulous objects in dark clouds [27], **S**—H II regions [28], **Sa**—southern dark dust clouds [29, 30], **SG**—nebulae [31], **VBH**—reflecting nebulae [32], **VDB**—reflecting nebulae [33], **W**—radio survey [34].

2.5. Short List of Sources

The short list of SFRs lists all objects in the main catalog according to their *lb* names, together with other traditional names of the sources and a list of data types for the SFRs (Table 2). The data types are indicated by numbers: an absence of data for a given type is indicated by a 0, while the presence of data is indicated by a 1 for O data, a 2 for R data, a 3 for IR data, a 4 for M data, and a 5 for D data.

Table 2. Short list of SFRs

No.	*lb* name	Data types	Name
1	000.00+0.19	01234	RCW138
2	000.00−0.18	00230	
3	000.01−0.55	01234	S18
4	000.06−0.20	00030	FIR16
5	000.06−0.31	00200	
6	000.10−0.17	00234	
7	000.13−0.55	01234	S19, RCW140
8	000.17+0.15	00200	
9	000.18−0.19	00030	FIR37
10	000.22−0.16	00030	FIR17
11	000.28−0.46	00234	
12	000.30−0.36	00200	
13	000.33−0.19	01234	S20, RCW141
14	000.35−0.28	00200	
15	000.35−0.82	00230	
16	000.39−0.54	00234	
17	000.39−0.42	00200	
18	000.47−0.35	00200	
19	000.50+0.17	00234	
20	000.52+0.18	00234	
21	000.53+0.27	00200	
22	000.56−0.38	00200	
23	000.57−0.63	00234	
24	000.59−0.22	00200	
25	000.59−0.50	00234	
26	000.59−0.86	01234	S21
27	000.65+0.63	00230	
28	000.76+0.16	00200	

3. DISCUSSION OF THE METHODS

3.1. Determinations of Boundaries of Star-Formation Regions

The natural boundaries of a SFR are the edges of its parent molecular cloud or cloud complex. However, the clouds of only a small number of nearby SFRs have been mapped. For most SFRs, only the velocities of molecular clouds toward associated radio or IR sources are known. Thus, additional criteria are needed to know whether to ascribe sources to a particular SFR. We adopt closeness of the coordinates and/or radial velocities of the objects under consideration as our primary criteria.

In the case of distant regions of the inner part of the Galaxy, it is often difficult to judge if similar coordinates and velocities really correspond to spatial proximity, due to ambiguity in distance determinations. Such sources were usually taken to be independent. In the absence of radial-velocity measurements, sources can be considered to be genetically related only if their positions in various spectral ranges are very close (comparable to the sizes of the sources themselves) or coincident. Checks for common origin should be repeated each time new observations be-

come available for such sources. For this reason, the total number of SFRs in the catalog has only formal significance, and no doubt will be revised as more observations become available.

3.2. Positions and Sizes of Sources

As a rule, we adopted the positions and sizes of sources from the original references. We redetermined the coordinates and sizes using the images in the original papers only in rare cases. We also performed similar estimates based on available images to determine the sizes of molecular clouds (outflows).

3.3. Sources in the Near Infrared

The spectral flux density is always expressed in Jansky. However, the fluxes of most IR sources at 0.9–20 μm are traditionally expressed in magnitudes. Calibration data are needed to transform these into the corresponding flux densities in Jansky. We adopted the following rule for this conversion: if the original paper contains no reference to the calibration used, we applied the calibration of Wilson *et al.* [35] for data published prior to 1983 and that of Koornneef for later publications [36].

3.4. Maser Sources

Surveys of maser sources with ordinary radio telescopes (with beam widths of about 1′ or more) have low positional accuracy, and the velocity ranges for some masers reaches tens or even hundreds of km/s or more. VLA observations of masers with arcsecond resolution reveal multiple maser spots at the positions of known sources, as a rule, scattered around ultracompact H II regions or IRAS sources. Each spot is observed within a narrow range of radial velocities. The spatial distributions of maser spots are very nonuniform, and usually groups or clusters of spots can be distinguished. For most well-studied OH, H_2O, and CH_3OH masers, the mean sizes of these groups is less than 1″ [37, 38]. Forster *et al.* [36] and Caswell *et al.* [37] suggested that each maser group was connected with a single ultracompact H II region or massive protostar. Often, several such groups are observed around IRAS sources, indicating, as do groups of ultracompact H II regions, a forming star cluster or association. Accordingly, each group of maser spots can be considered an individual forming protostar, i.e., a separate source with the Galactic coordinates given in Column 2. However, since VLA observations have not been acquired for all known maser sources, and the identification of clusters of spots is a somewhat arbitrary process, the catalog considers clusters of maser spots to be individual groups only when their coordinates are separated from those of other spots by more than 5″–10″.

4. PRELIMINARY ANALYSIS

4.1. Two Types of Star-Forming Regions

One common feature of all young stars is violent atmospheric activity, which is revealed, on the one hand, by the ejection of matter in the form of wind, jets, etc., and the interactions of these outflows with the ambient medium, and, on the other hand, by the accretion of matter. One of the most remarkable manifestations of interactions are molecular outflows, visible in the optical as bipolar nebulae [39–42], which are observed near young stars of all nascent masses. At the same time, other observational characteristics differ considerably for young stars with high and low masses.

Larson [43] found a correlation between the mass of the parent cloud and the mass of the most massive star born in the cloud. Massive stars are mainly formed in giant molecular clouds in the spiral arms of the Galaxy. The high luminosity of these stars makes them observable in most parts of the Galaxy. Due to their low luminosities, intermediate- and low-mass young stars are visible predominately near the Sun, in small compact clouds outside the main spiral arms. For most SFRs, either data on massive stars or on intermediate/low-mass stars dominate. The main difference in the observational manifestations of these two types of star formation is associated with the fact that massive stars are formed very rapidly, and this process is essentially invisible in the optical, since the stars evolve to the main sequence before they emerge from their dust cocoons [44, 45], whereas intermediate- and low-mass stars become visible in the optical long before they reach the main sequence [5].

Massive, young stars are observed as compact, bright IR sources, with their maximum radiation at 100 μm, and also as ultracompact H II regions. An undetectable or low level of radio flux is usually associated with the formation of massive stars prior to the main sequence [46]. In the optically thick dust cocoon surrounding a massive protostar, all the UV radiation is reemitted in the IR flux [46]. Inside the cocoon, the star ejects a strong stellar wind at velocity up to several thousand km/s, forming a cavity inside the cocoon. The star ionizes the cavity, which is observed as an ultracompact H II region with a characteristic size of 10^{17} cm [44]. The morphological types of such regions [44] are presented in the catalog, in accordance with the original references [46–48]. The molecular flows around massive stars are poorly collimated, but their energy is much higher than that of the strongly collimated flows around low-mass stars [49]. The catalog also indicates observations of molecular flows. The stage with an ultracompact H II region inside a cocoon lasts approximately 10^5 yr.

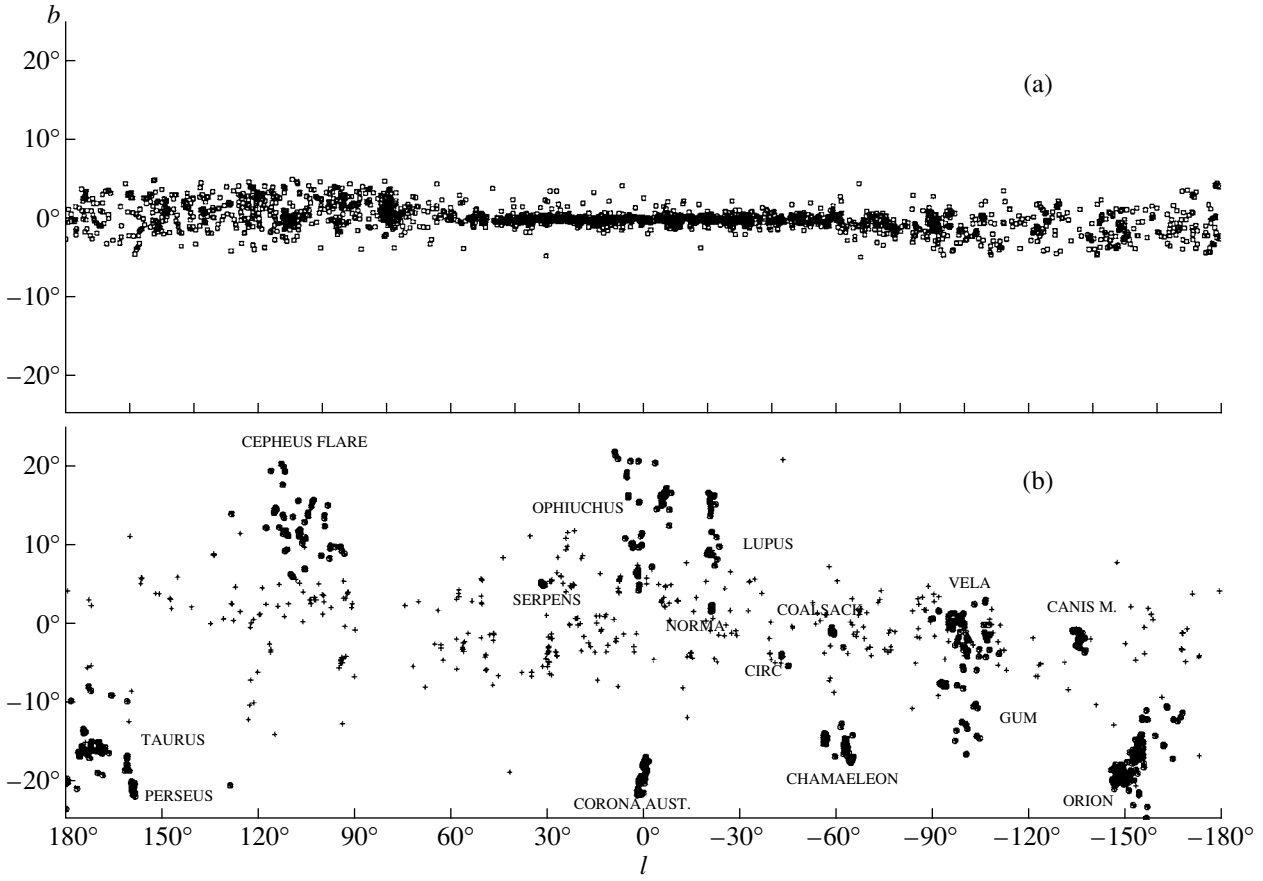

Fig. 1. (a) Distribution of SFRs in the Galaxy (sample A). (b) Distribution of IRAS sources in dark-cloud complexes closest to the Sun and in globules.

Wood and Churchwell [44] suggest that massive stars spend some 20% of their lifetime on the main sequence inside cocoons.

Massive young objects are often associated with OH, H_2O, and methanol (CH_3OH) maser sources. Due to their high luminosity, water maser emission at 22.2 GHz and methanol maser emission at 6.6 GHz are the best tracers of ultracompact H II regions [50–52]. Finding new masers can enable the discovery of new regions of formation of massive stars.

Intermediate- and low-mass stars evolving toward the main sequence can be divided into four classes according to the shape of their spectra [5, 6]. These correspond to an evolutionary sequence for the sources. Class 0 corresponds to protostellar objects deeply embedded in dust clouds, invisible in the optical near-IR, and intermediate-IR. They are sources of strong millimeter radiation, and their bolometric luminosities indicate that the mass of circumstellar material exceeds that of the central source, which is actively accreting this surrounding material. Thus far, this is the earliest observed stage in the formation of protostars. Class I corresponds to the next stage in the evolution of a protostellar object, when it remains invisible in the optical but becomes observable in the entire IR range, with a spectrum that grows rapidly toward long wavelengths. Class II corresponds to an optical star with an IR spectrum that is flat or decreases toward long wavelengths and exhibits strong Hα emission. These stars have not yet reached the main sequence (classical T Tauri stars and Ae/Be stars), and have a strong IR excess due to their circumstellar disks. Class III refers to stars with a weak IR excess relative to the star's reddened blackbody radiation. These stars are approaching the main sequence, and already have no disk (weak-line T Tauri stars and/or strong X-ray sources with relatively weak Hα emission). The evolutionary classes for low-mass stars presented in the catalog are those published in the original references. As a rule, the catalog includes predominantly Class 0 and Class I objects, with a relatively small number of Class II objects.

4.2. Galactic Distribution of the SFRs

To study the distribution of the SFRs in the Galaxy, we subdivide them into SFRs closest to the

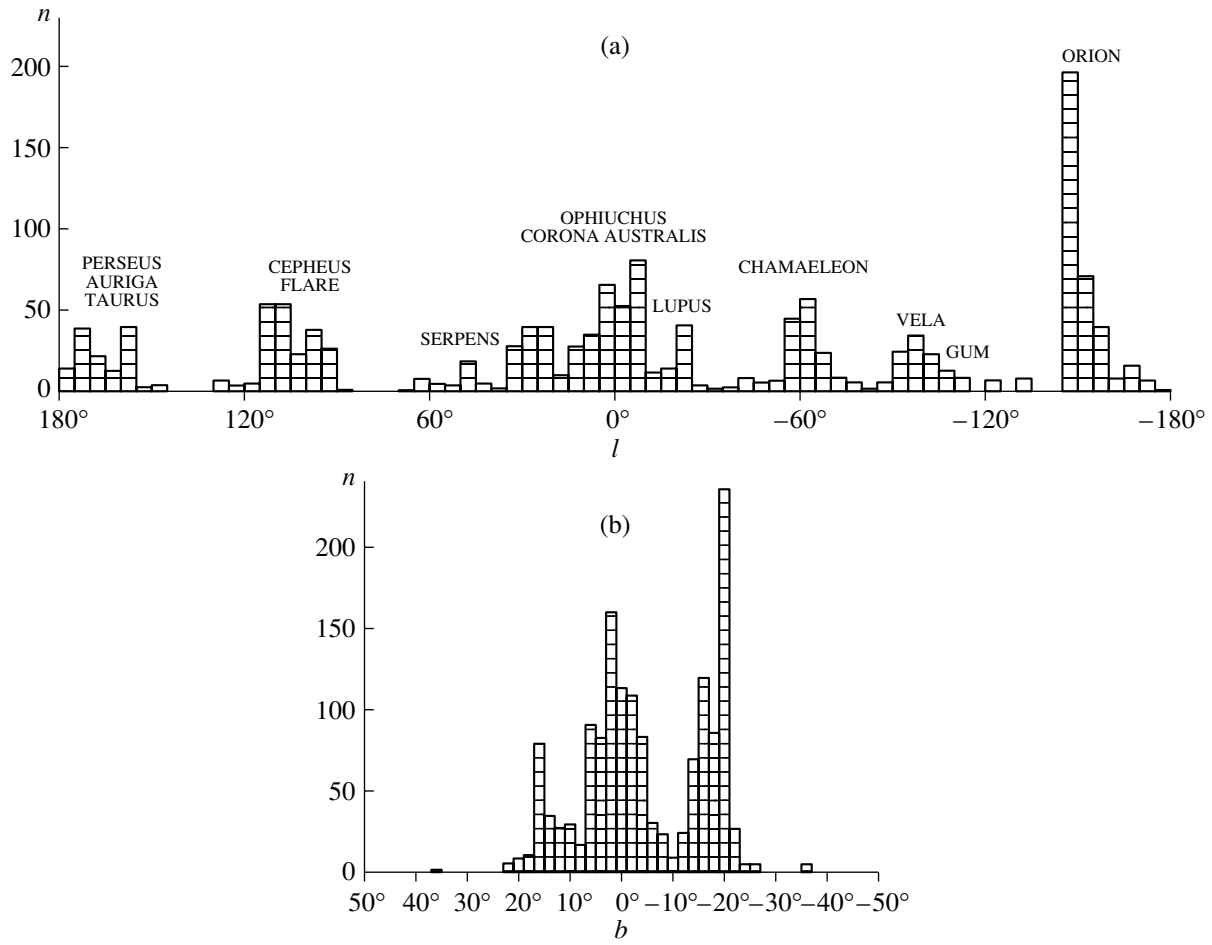

Fig. 2. The density distribution of IRAS sources (sample B) in (a) longitude and (b) latitude.

Sun, in which we observe primarily the formation of low-mass stars, and more distant SFRs, in which we observe the formation of massive stars.

We carry out this subdivision as follows. From the short list of SFRs, we exclude (i) objects connected with known dark clouds and globules (D data, $N = 423$), (ii) SFRs with Galactic latitudes in excess of $5°$ ($N = 71$), and (iii) SFRs for which no velocity data are available ($N = 530$; these regions are only candidate SFRs). We then combine the first two types of objects with SFRs in the catalog supplement. This divides the SFRs into two samples: sample A dominated by regions forming massive stars and consisting primarily of distant objects ($N = 2243$) and sample B dominated by regions forming low-mass stars and situated close to the Sun (within 1000 pc).

The sky distribution of the SFRs in sample A is shown in Fig. 1a. The density and narrowness of the central part of the distribution stands out; here, we find the main spirals and molecular disk of the Galaxy. A warp in the plane of the outer disk can clearly be seen toward the Galactic anticenter [53, 54].

The distribution of the IRAS sources in sample B is presented in Fig. 1b. Each dark-cloud complex appears as a cluster of IRAS sources (circles), while globules containing dark stellar objects are shown as crosses. The general distribution of nearby SFRs reflects the distribution of matter in Gould's belt.

Figure 2 presents histograms of the distributions of nearby young objects of sample B in longitude and latitude. These histograms are very nonuniform: the peaks of the distributions correlate with the positions of complexes of dark clouds. The large range of peak amplitudes in the histograms testify to differences in the star-formation intensity in different complexes. The latitude distribution has three maxima: at $0°$, $+18°$, and $-18°$. The central maximum corresponds to SFRs in the Galactic plane, whereas the other two provide evidence for an envelope-like distribution of the nearby dense gas.

4.3. Formal Classification of SFRs

An SFR can include forming stars, accretion disks or cocoons around young stars, H II regions around

Table 3. SFRs of various classes in sample A

SFR class	N(SFRs)	N(SFRs + M)	SFR class	N(SFRs)	N(SFRs + M)
IM	883	200	OM	21	0
RIM	651	327	R	20	0
ORIM	324	148	OI	15	0
OIM	112	9	M	13	13
RM	92	0	ORM	12	0
RI	35	0	O	10	0
ORI	30	0	OR	9	0

massive stars, jets, Herbig–Haro objects, reflection and infrared nebulae, molecular outflows, and masers, as well as dark and molecular clouds and cloud cores—the parent material from which the stars are formed.

Each of these objects corresponds to a type of information presented in the catalog: O—optical objects (stars, diffuse and reflection nebulae, Herbig–Haro objects); D—dark clouds and globules; IR—accretion disks, cocoons, and the dense cores of molecular clouds; R—H II regions and their motions; M—the molecular composition of the circumstellar gas around a star, its motion, and the presence of masers. Each SFR can be described by a set of these data types, which we will call the "class" of the SFR. Thus, class RIM means that a given SFR includes data of types R, IR, and M; class OIM includes data types O, IR, and M; and so forth.

Table 3 presents rates of occurrence of various SFR classes in sample A. Column 1 lists the SFR classes, while columns 2 and 3 give the number of SFRs in each class and the number of SFRs in each class containing H_2O masers.

Three classes in sample A—IM (883 objects), RIM (651), and ORIM (324)—are the richest and include the majority of the SFRs. Two represent the most typical SFRs. Figure 3a–3h show the Galactic distributions for each class. The appearance of a distribution provides clues to the possible physical nature of the corresponding class. RIM objects (Fig. 3a) are mainly distributed in the inner Galaxy, very close to the Galactic plane. This distribution is characteristic of SFRs in which massive stars are formed. The lack of optical data indicates large distances for these objects. RI SFRs (Fig. 3f) represent the same type of object. ORIM objects (Fig. 3c) show a fairly uniform distribution in longitude. The availability of radio and optical data suggests that these SFRs are mainly regions of the formation of massive stars relatively near the Sun (about 3 kpc). These SFRs are probably associated with the spiral arms closest to the Sun. The sparse ORI class (Fig. 3g) probably contains similar objects. The distribution of IM objects (Fig. 3b) is very similar to the overall distribution for all the SFRs (Fig. 1a). This suggests that the IM objects are not a homogeneous class, and instead represent a mixture of SFRs in which massive and low-mass stars are formed.

Two more classes of SFR contain significant numbers of objects, and may represent specific phases of star formation. These are classes OIM (Fig. 3d) and RM (Fig. 3e). Class OIM shows a fairly extended latitude distribution and appears to include nearby SFRs, with protostars and intermediate/low-mass stars that are already visible in the optical, embedded in reflection or emission nebulae and surrounded by molecular clouds.

Class RM corresponds to the final evolutionary phase of regions in which massive stars are formed, without signs of new star formation, when only an H II region and the remnants of the parent cloud remain. The absence of optical nebulae and the narrow latitude distribution testify to large distances for these objects. Among nearby H II regions, classes O, OR, OI, and OM are similar. The number of objects in these classes is an order of magnitude lower than the number of SFRs in classes RIM and ORIM, suggesting that the formation of massive stars is mainly concentrated in large complexes in which centers of star formation appear one after another, until the remains of the initial cloud dissipate under the action of the radiation and wind from the young, expanding clusters and associations that have already formed. The lifetime of such a complex exceeds that of a single H II region by at least an order of magnitude.

R objects have distributions similar to those for RIM and RM objects; further studies may make it possible to assign them to one of these two classes. The remaining poor classes (O, OM, OI) are made up of relatively nearby objects and probably correspond to evolved SFRs with both massive and low-mass stars. Class M corresponds to isolated maser sources,

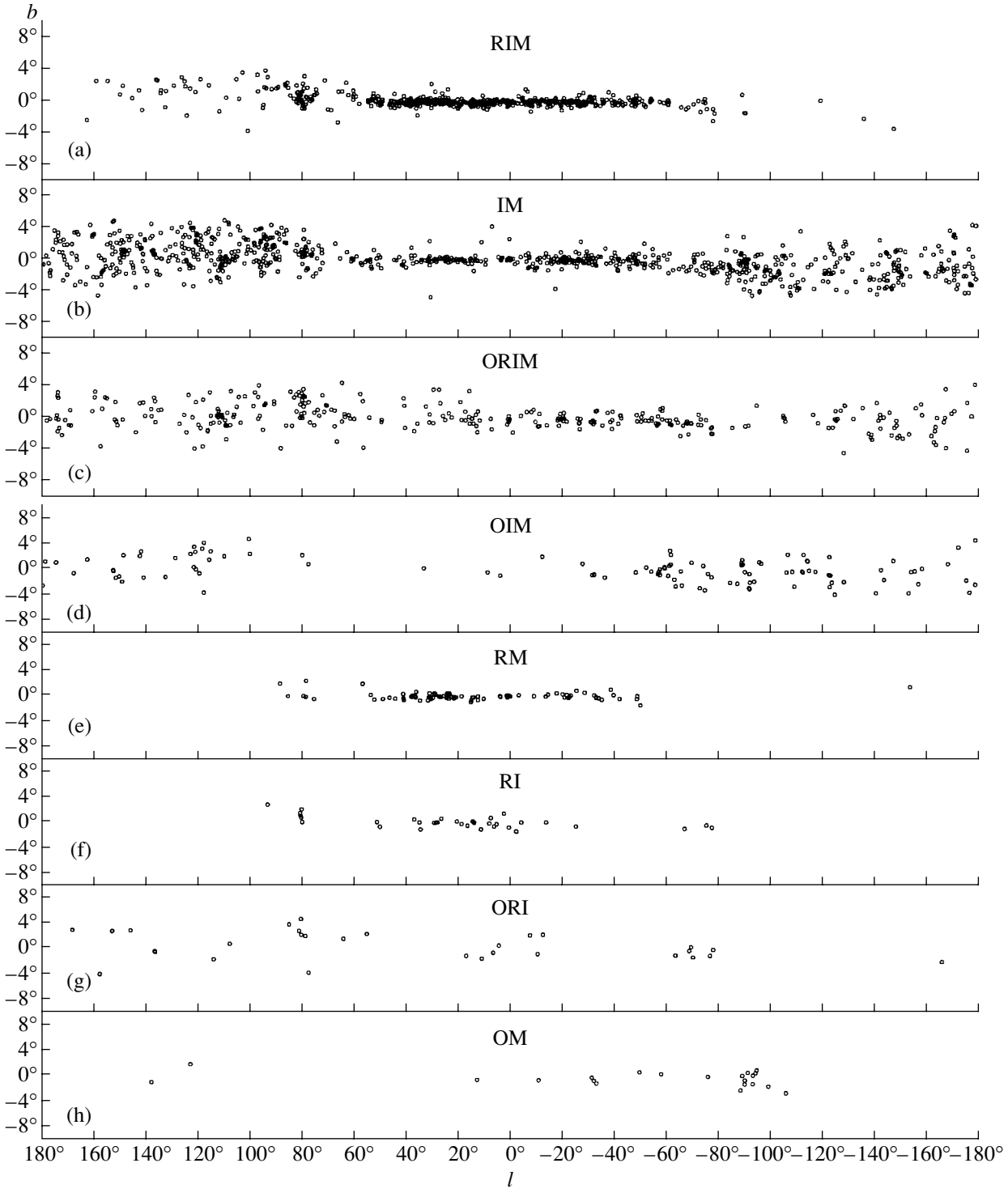

Fig. 3. Distributions of SFRs of various classes on the sky: (a) class RIM, (b) class IM, (c) class ORIM, (d) class OIM, (e) class RM, (f) class RI, (g) class ORI, (h) class OM.

which act as beacons marking new star-forming regions.

The density distributions in longitude for the three richest SFR classes (RIM, IM, and ORIM) are shown in Figs. 4a–4c. We compare each distribution with that for the subsample from the same class containing H_2O masers. For class RIM, the two distributions are well correlated (Fig. 4a); the probability of them representing the same distribution is 0.83, according to a χ^2 criterion (the calculated

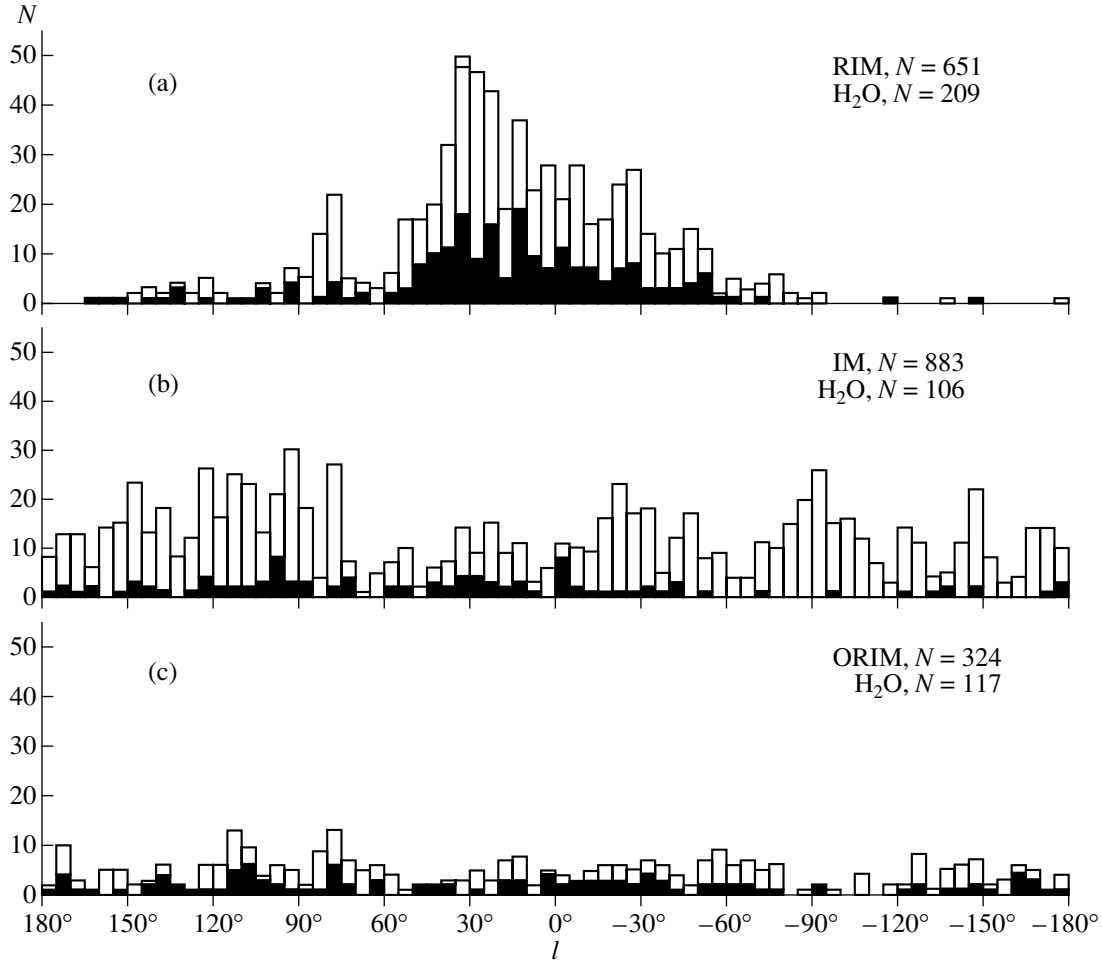

Fig. 4. Histograms of distributions in longitude for classes (a) RIM, (b) IM, and (c) ORIM, together with the corresponding distributions for subsamples containing H_2O masers.

value is $\chi^2 = 11.7$, with the number of degrees of freedom being $n = 18$). This result is equivalent to the statement that H_2O masers are good tracers of regions of formation of massive stars [55, 56]. The peaks of both distributions correspond to the tangential directions of spiral arms; the ratio of the total number of RIM objects to the number of RIM objects associated with H_2O masers is 2.8.

The distributions of all ORIM objects and of the subsample of these objects containing H_2O masers (Fig. 4c) are also similar, with the probability that they represent the same population being 0.75 ($\chi^2 = 13.6$ and $n = 18$). This supports the above suggestion that these objects correspond to regions of massive-star formation in the solar neighborhood. The ratio of the total number of the ORIM objects to the number associated with H_2O masers is 3.1, close to the ratio for the RIM objects. This supports the hypothesis that the objects in these two classes have similar natures.

The shape of the density-distribution histogram for the IM objects (Fig. 4b) is unusual. The distribution of these objects in the sky (Fig. 3b) resembles the overall distribution of all SFRs, suggesting that it includes two groups of SFRs. The first corresponds to regions of formation of massive stars, mainly between $-60°$ and $+60°$, with obvious peaks at $30°$ and $-30°$; this is supported by the narrow distribution in latitude. The second group, which is predominantly located in the outer parts of the disk, corresponds to regions of formation of low-mass stars. A comparison of the density distributions for class IM as a whole and for the subsample containing H_2O masers (Fig. 4b) yields the probability that they are the same that is close to zero. The ratio of the total number of IM objects to the number associated with H_2O masers is 4.4, nearly a factor of 1.5 larger than the ratios for the RIM and ORIM objects. This may mean that more than half of the IM objects are regions of formation of low-mass stars. If we consider subsamples of SFRs containing any masers (OH, H_2O, CH_3OH), rather than only H_2O masers, the probabilities that the maser objects and overall class of objects have

the same distributions become slightly lower: 0.65 and 0.61 for the classes RIM and ORIM, respectively. This may indicate that H_2O masers are better indicators of massive-star formation than other masers.

5. CONCLUSIONS

Our catalog presents descriptions of more than three thousand SFRs, of which of the order of 500 are candidate SFRs. The candidate objects are primarily those for which velocity data are lacking. The catalog contains data on the photometric fluxes of the SFRs and their radial velocities, as well as information on diffuse and reflection nebulae, dark and molecular clouds, and other objects associated with young stars. This is a unique catalog, with no counterpart among other catalogs. Our preliminary analysis of the catalog data based on sets of data types for each SFR enables a division of the SFRs into classes, which may correspond to regions in which predominantly massive or low-mass stars are formed. Analysis of data for these classes should ultimately make it possible to draw some conclusions concerning the relative durations of various phases of star formation. In the future, we plan to study the large-scale structure of the Galactic disk and of individual spiral arms using the catalog data, and also to continue a more detailed classification of the SFRs. Our catalog does not permit absolute statistical estimation of the total number of SFRs in the Galaxy, since existing observations cannot reveal physical associations between distant, poorly studied SFRs; however, relative statistical estimates are possible. The catalog presents the principle information for each SFR, facilitating the selection of objects for further studies and making it a useful tool for observers. It also opens a wide range of further studies in various fields of astrophysics.

ACKNOWLEDGMENTS

This study was supported by the Russian Foundation for Basic Research (project no. 01-02-16306). The author thanks G.A. Leikin for her stimulating work on this paper and for helpful discussions.

REFERENCES

1. P. G. Mezger, W. Altenhoff, J. Schraml, *et al.*, Astrophys. J. Lett. **150**, L157 (1967).
2. P. G. Mezger and A. P. Henderson, Astrophys. J. **147**, 471 (1967).
3. IRAS Point Source Catalog. Joint IRAS Science Working Group (U.S. GPO, Washington, 1986).
4. M. A. Braz and N. Epchtein, Astron. Astrophys. Suppl. **54**, 167 (1983).
5. C. J. Lada and B. A. Wilking, Astrophys. J. **287**, 610 (1984).
6. P. Andre, D. Ward-Thompson, and M. Barsony, Astrophys. J. **406**, 122 (1993).
7. J. Brand, L. Blitz, and J. G. A. Wouterloot, Astron. Astrophys. Suppl. **65**, 537 (1986).
8. T. L. Bourke, A. R. Hyland, and G. Robinson, Mon. Not. R. Astron. Soc. **276**, 1052 (1995).
9. D. P. Clemens and R. Barvainis, Astrophys. J., Suppl. Ser. **68**, 257 (1988).
10. C. R. Lynds, Publ. NRAO **1**, 43 (1961).
11. J. von Dorschner and J. Gurtler, Astron. Nachr. **287**, 257 (1963).
12. E. M. Pike and F. D. Drake, Astrophys. J. **139**, 545 (1964).
13. H. R. Dickel, H. Wendker, and J. H. Bieritz, Astron. Astrophys. **1**, 270 (1964).
14. S. D. Price, T. L. Murdock, and K. Shivanandan, ⟨AFGL-TR-83-0055⟩ (1983).
15. C. S. Gum, Mem. R. Astron. Soc. **67**, 155 (1955).
16. A. L. Gyulbudaghian, Yu. I. Glushkov, and E. K. Denisyuk, Astrophys. J. Lett. **224**, L137 (1978).
17. J. V. Feitzinger and J. A. Stuwe, Astron. Astrophys., Suppl. Ser. **58**, 365 (1984).
18. A. L. Gyul'budagyan and T. Yu. Magakyan, Astron. Tsirk., No. 953 (1977).
19. A. L. Gyul'budagyan, Pis'ma Astron. Zh. **8**, 232 (1982) [Sov. Astron. Lett. **8**, 123 (1982)].
20. W. F. Hoffmann, C. L. Frederick, and R. J. Emery, Astrophys. J. Lett. **170**, L89 (1971).
21. R. W. Sinnott, $\langle Doc.No.NSSDC/WDC-A-R\&S89-29\rangle$ (1988).
22. E. Kallas and W. Reich, Astron. Astrophys. Suppl. **42**, 227 (1980).
23. B. T. Lynds, Astrophys. J., Suppl. Ser. **7**, 1 (1962).
24. P. S. The, D. de Winter, and M. R. Perez, Astron. Astrophys., Suppl. Ser. **104**, 315 (1994).
25. S. D. Price and T. L. Murdock, $\langle AFGL-TR-83-0161\rangle$ (1983), The Revised AFGL Infrared Sky Survey Catalog.
26. A. M. Rodgers, C. T. Campbell, and J. B. Whiteoak, Mon. Not. R. Astron. Soc. **121**, 103 (1960).
27. M. Cohen, Astron. J. **85**, 29 (1980).
28. S. Sharpless, Astrophys. J., Suppl. Ser. **4**, 257 (1959).
29. A. Sandqvist, Astron. Astrophys. **53**, 179 (1976).
30. A. Sandqvist, Astron. Astrophys. **57**, 467 (1977).
31. G. A. Shaĭn and V. F. Gaze, Izv. Krym. Astrofiz. Obs. **15**, 11 (1955).
32. S. van den Bergh and W. Herbst, Astron. J. **80**, 208 (1975).
33. S. van den Bergh, Astron. J. **71**, 990 (1966).
34. G. Westerhout, Bull. Astron. Inst. Netherlands **14**, 215 (1958).
35. W. J. Wilson, P. R. Schwartz, G. Neugebauer, *et al.*, Astrophys. J. **177**, 523 (1972).
36. J. Koornneef, Astron. Astrophys. **128**, 84 (1983).
37. J. R. Forster and J. L. Caswell, Astron. Astrophys. **213**, 339 (1989).
38. J. L. Caswell, R. A. Vaile, S. P. Ellingsen, *et al.*, Mon. Not. R. Astron. Soc. **272**, 96 (1995).
39. T. Neckel and H. J. Staude, Astron. Astrophys. **131**, 200 (1984).

40. J. L. Yun and D. P. Clemens, Astrophys. J. Lett. **385**, L21 (1992).
41. Y. Fukui, T. Iwata, A. Mizuno, *et al.*, in *Protostars and Planets III,* Ed. by E. H. Levy and J. I. Lunine (Univ. of Arizona Press, Tucson, 1993), p. 603.
42. Y. Wu, M. Huang, and J. He, Astron. Astrophys., Suppl. Ser. **115**, 283 (1996).
43. H. B. Larson, Mon. Not. R. Astron. Soc. **200**, 159 (1982).
44. D. O. S. Wood and E. Churchwell, Astrophys. J., Suppl. Ser. **69**, 831 (1989).
45. M. Beech and R. Mitalas, Astrophys. J., Suppl. Ser. **95**, 517 (1994).
46. S. Molinari, J. Brand, R. Cesaroni, *et al.*, Astron. Astrophys. **336**, 339 (1998).
47. S. Kurtz, E. Churchwell, and D. O. S. Wood, Astrophys. J., Suppl. Ser. **91**, 659 (1994).
48. A. J. Walsh, A. R. Hyland, G. Robinson, *et al.*, Mon. Not. R. Astron. Soc. **291**, 261 (1997).
49. D. S. Shepherd and E. Churchwell, Astrophys. J. **472**, 225 (1996).
50. W. Batria, H. E. Matthew, K. M. Menten, *et al.*, Nature **326**, 49 (1987).
51. K. M. Menten, Astrophys. J. Lett. **380**, L75 (1991).
52. S. P. Ellingsen, R. P. Norris, and P. M. McCulloch, Mon. Not. R. Astron. Soc. **279**, 101 (1996).
53. F. J. Kerr, Astron. J. **62**, 93 (1957).
54. J. G. A. Wouterloot, J. Brand, W. B. Burton, *et al.*, Astron. Astrophys. **230**, 21 (1990).
55. F. Palla, J. Brand, R. Cesaroni, *et al.*, Astron. Astrophys. **246**, 249 (1991).
56. F. Palla, R. Cesaroni, J. Brand, *et al.*, Astron. Astrophys. **280**, 599 (1993).

Translated by N. Samus'

Astronomy Reports, Vol. 46, No. 3, 2002, pp. 206–215. Translated from Astronomicheskiĭ Zhurnal, Vol. 79, No. 3, 2002, pp. 229–239.

Microstructure of Pulsar Radio Pulses Measured with a Time Resolution of 62.5 ns at 1650 MHz

M. V. Popov[1], N. Bartel[2], W. H. Cannon[2,3], A. Yu. Novikov[3], V. I. Kondratiev[1], and V. I. Altunin[4]

[1]*Astro Space Center, Lebedev Physical Institute, ul. Profsoyuznaya 84/32, Moscow, 119991 Russia*

[2]*Department of Physics and Astronomy, York University, Toronto, Ontario, M2J 1P3 Canada*

[3]*Space Geodynamics Laboratory/CRESTech, Toronto, Ontario, M2J 2K1 Canada*

[4]*Jet Propulsion Laboratory, 4800 Oak Grove Dr., Pasadena CA, 91109 USA*

Received April 25, 2001

Abstract—We present an analysis of pulsar observations carried out on two frequency channels at 1634 MHz and 1650 MHz with a time resolution of 62.5 ns on the 70-m radio telescope of the NASA Deep Space Network in Tidbinbilla. The data were recorded using the S2 system, intended primarily for VLBI observations. Microstructure with characteristic timescales of 270, 80, and 150 μs was detected in pulsars B0833 − 45, B1749 − 28, and B1933 + 16, respectively. The distribution of microstructure timescales for the Vela pulsar (B0833 − 45) is characterized by a gradual growth with decreasing timescale to 200 μs; the distribution has a maximum at 20–200 μs and falls off sharply for timescales below 20 μs. The statistical relation between the microstructure modulation index m and the corresponding timescale τ_μ can be approximated by the power law dependence $m \propto \tau_\mu^{0.5}$; i.e., the intensity is higher for micropulses with longer durations. This contradicts the predictions of nonlinear models for the formation of micropulses by supercompact soliton wave packets. In all the pulsars studied, the time delays of the micropulses between the two frequency channels deviate from the expected dispersion laws for the interstellar plasma. In particular, the micropulses in the low-frequency channel arrive earlier than predicted by the dispersion measures derived previously from the mean pulse profiles. The deviation from the dispersion delay is determined most accurately for B0833 − 45, and is 4.9 ± 0.2 μs. Such anomalous delays are probably associated with the effects of propagation of the radio emission within the pulsar magnetosphere.

1. INTRODUCTION

The microstructure of the radio pulses of pulsars represents rapid variations in the intensities of individual pulses with characteristic timescales from several to several hundreds of microseconds. Such rapid fluctuations in the observed radio emission could arise from beam effects associated with rotation of the pulsar or the motion of the radiating region along a curvilinear trajectory (magnetic force line). Alternatively, microstructure could reflect spatial (longitudinal or radial) modulations of the electric-charge density of the radiating region. Finally, the micropulses could represent actual flares of the radio emission. It is most likely that the observed microstructure is generated by a combination of these factors, and a key task is distinguishing between these effects in order to study the geometric characteristics of the radio emission, such as the directional beam emitted by the elementary emission region and the magnetic-field structure constraining the motion of this region. It is also of interest to investigate the physics of processes underlying the radio-emission mechanism itself.

In spite of thirty years of studies of pulsars, there is no general agreement about the mechanism for their radio emission. In our view, multifrequency investigations of microstructure with submicrosecond time resolution and polarization sensitivity represent the most promising approach for obtaining new data that can improve our understanding of the radio-emission mechanism and other physical processes occurring in the neutron-star magnetosphere. Unfortunately, investigations of microstructure have received appreciably less attention than studies of certain other properties of pulsars, such as their mean profiles, fluctuation spectra, regular subpulse drift, and nulling. This is due to several circumstances.

First, in order to study the structure of individual pulses with high time resolution, it is necessary to record the received signal using a rather broad frequency bandwidth, which requires the use of rapid analog–digital converters and leads to the need to

1063-7729/02/4603-0206$22.00

record and store huge volumes of digital data. Second, dispersion of the radio waves in the interstellar medium and scattering on inhomogeneities in the interstellar plasma broadens the micropulses in time. Dispersion of the radio waves is a linear process, and its effect can be fully eliminated via digital filtering of the received signal using the predetection compensation technique proposed by Hankins [1, 2].

Interstellar scattering displays purely statistical behavior and fundamentally limits the achievable time resolution. For example, the scattering time at 111 MHz is about 10 μs, even for the nearest pulsars; it is possible to achieve a time resolution of 0.5 μs at 408 MHz for pulsars with dispersion measures less than 15 pc/cm^3, and the same time resolution can be obtained for pulsars with dispersions measures up to 90 pc/cm^3 at 1650 MHz. These estimates for the scattering time were derived using the empirical formula obtained by Cordes and presented by Hankins [3]. Thus, one factor hindering microstructure studies is the fact that reconstruction of the shape of a recorded signal via predetection compensation for the dispersion requires appreciable computational resources, and the subsequent analysis of the individual correlation functions is difficult to automate.

Finally, we should note that it is not possible to average a signal in time if we wish to analyze the structure of individual pulses with the maximum time resolution allowed by a given frequency bandwidth. The required high sensitivity can be provided only by very large radio telescopes.

The first microstructure studies were carried out by Hankins [4] for the bright pulsars B0950 + 08 and B1133 + 16 at meter wavelengths on the 300-m Arecibo telescope in 1971–1972. The time resolution in these first observations was 8 μs, and the characteristic timescales for the microstructures of the two pulsars were 175 and 575 μs, respectively. Later, Cordes [5, 6] and Boriakoff [7] discovered microstructure in B1919 + 21 and B2016 + 28 at 318 and 430 MHz, also in observations on the Arecibo telescope. Our group published several articles presenting results of microstructure studies of the three pulsars B0809 + 74, B0950 + 08, and B1133 + 16 based on observations obtained on the Large Phased Array at the Pushchino Radio Astronomy Observatory at 102.5 MHz with a time resolution of 10 μs [8–10]. All these investigations were carried out at meter wavelengths, where the radio flux densities of pulsars are maximum. It appears that the depth of modulation of microstructure is also maximum at low frequencies [11, 12]. However, later studies have shown that microstructure can be fairly well defined at decimeter wavelengths as well. Using the 100-m Effelsberg telescope, Bartel [13] discovered micropulses for B1133 + 16 at 2700 MHz; the shortest micropulses had durations of about 6 μs and had correlated intensities in a 20 MHz band. Bartel and Hankins [14] detected micropulses with a duration of 2.5 μs at 1720 MHz for this same pulsar in observations on the Effelsberg 100-m telescope with a time resolution of 100 ns.

In their comparison of microstructure parameters for B1133 + 16 measured at 102.5 and 1400 MHz, Smirnova *et al.* [15] showed that the probability of the appearance of microstructure decreases at the higher frequency, while the depth of its modulation remains roughly the same as at the lower frequency. Microstructure studies at relatively high (decimeter) frequencies have certain advantages, of which the most important is the possibility of achieving submicrosecond time resolution thanks to the decrease in the characteristic scattering time with increasing observing frequency. Johnston *et al.* [16] demonstrated the existence of microstructure at 1413 MHz for B0833 − 45 (the Vela pulsar). We have already investigated the properties of microstructure of three bright pulsars at 1650 MHz (B0950 + 08, B1133 + 16, and B1929 + 10) [17]. The current paper presents a microstructure analysis for four more pulsars based on observations carried out at 1650 MHz with a time resolution of 62.5 ns.

2. OBSERVATIONS AND DATA REDUCTION

The observations were obtained on the 70-m Tidbinbilla radio telescope in Australia. This telescope is part of the NASA Deep Space Network, but also conducts a limited number of scientific radio astronomy observations. We observed B0833 − 45, B1749 − 28, and B1933 + 16 on May 30, 1999, and B1641 − 45 on September 6, 1997, during specialized tests that were part of a program to prepare for future interferometric experiments with the HALCA orbiting antenna [18]. The data were recorded using an S2 system, intended primarily for VLBI observations [19, 20]. This system enabled continuous recording of the received signal in two frequency channels with bandwidths of 16 MHz each. The two channels were adjacent in frequency, at 1634 and 1650 MHz (these are the lower edges of each band). The signal was digitized with two-bit sampling and four-level quantization at the Nyquist frequency. The received left-circularly polarized signal was recorded in each channel.

The recorded data were subsequently copied from the S2 video cassettes to the hard disk of a SUN workstation at the Space Geodynamics Laboratory in Toronto via a specialized (TCI) data interface. A similar method was applied by Kempner *et al.* [21] and in our earlier microstructure studies using the S2 system [17]. In the first stage of the data reduction, the two-bit signal was decoded, and a crude detection

Table 1. Main data-reduction parameters: period P, dispersion measure DM and reference, number of recorded pulses N, number of strong pulses selected for microstructure analysis N_p, number of counts T in selected window used to compute CCF, mean signal-to-noise ratio SNR

PSR (B)	P, s	DM, pc/cm^3	Reference	N	N_p	T	SNR
0833−45	0.089	68.012 ± 0.007	[22]	3370	1230	131 072	0.30
1641−45	0.455	480 ± 5	[23]	2250	486	524 288	0.20
1749−28	0.562	50.88 ± 0.14	[24]	2700	685	524 288	0.06
1933+16	0.359	158.53 ± 0.05	[25]	6700	339	524 288	0.05

and averaging of the detected signal was performed with a time constant of 128 μs (essentially every count of the decoded signal was squared, and the result was averaged over 4096 points). Further, by synchronously averaging the signal with a time interval corresponding to the pulsar period, we determined the pulse phase and separated out that part of the recording (the "window") containing strong pulses exceeding a specified threshold.

The criterion used to select strong pulses was the signal-to-noise ratio SNR = (ON − OFF)/OFF, where ON and OFF are the mean signals in and outside the selected window. We selected individual pulses with SNR values exceeding 0.05 for further analysis; i.e., the increase in the antenna temperature for these pulses was at least 5% of the system noise temperature. The system noise temperature for the 70-m Tidbinbilla telescope at 1650 MHz was about 50 Jy. Thus, the flux densities of the selected pulses averaged in the window exceeded 2.5 Jy. The number of strong pulses selected for further analysis for each pulsar is indicated in Table 1. In this way, the volume of data for the full analysis was reduced by a factor of several hundred.

We again decoded the two-bit signals for the selected pulses using a specialized algorithm taking into account the current coding statistics. The decoded data were further reduced applying the method for predetection compensation of dispersion smearing of the pulses proposed by Hankins in 1971 [1, 2]. The essence of this method is that the spectrum of the analyzed signal derived by performing a fast Fourier transform of the data is corrected in both amplitude (for nonuniformity in the frequency characteristics of the received track) and in phase (for dispersion delay of the radio signal in the interstellar medium, by multiplying by a complex function computed for the corresponding dispersion measure). At this stage, narrow-band radio interference (if present) was removed from the spectrum, together with the phase-calibration tones. After correcting the spectrum, we performed a digital detection of the signal consisting of an inverse Fourier transform of the corrected spectrum, in which the complex amplitudes of harmonics corresponding to negative frequencies were assumed to be zero. As a result, the detected signal represents a sum of the squares of the real and imaginary parts of each complex number in the dataset obtained after the inverse Fourier transform. A more detailed description of the data-reduction method is given in [17]. Figure 1 presents an example of individual pulses of B0833 − 45 in the two frequency channels after removal of dispersion smearing; the correlation between the fine structure in the pulses at the two frequencies is clearly visible.

3. MICROSTRUCTURE PARAMETERS

3.1. Cross-Correlation Functions

It is traditional to analyze microstructure parameters by calculating the autocorrelation functions (ACFs) of the reconstructed signals. In our observations, we recorded the signals at 1634 MHz and 1650 MHz in two adjacent 16-MHz frequency channels, so that the relative "detuning" between the channels was about 1%. Therefore, we used the cross-correlation functions (CCFs) rather than the ACFs between the intensities reconstructed in the two channels. In contrast to ACFs, CCFs do not contain a noise peak at zero time shift, making it easier to distinguish features corresponding to the shortest timescales. The normalized CCFs $R_{1,2}(\tau)$ were calculated using the expression

$$R_{1,2}(\tau) = [R_{1,1}(0)R_{2,2}(0)]^{-1/2} \times \sum_{t=1}^{T} I_1(t)I_2(t+\tau), \quad (1)$$

where $I_1(t)$ and $I_2(t)$ are the reconstructed intensities in the two frequency channels, t is the reading number, T is the total number of readings in the selected window, and $R_{1,1}(0)$ and $R_{2,2}(0)$ are the unnormalized ACFs; zero shift in the CCF ($\tau = 0$) corresponds to the dispersion delay between the frequency channels. The calculated CCFs for each pulsar were then averaged; the averaged CCFs after smoothing over 1 μs are shown in Fig. 2. This figure has two parts:

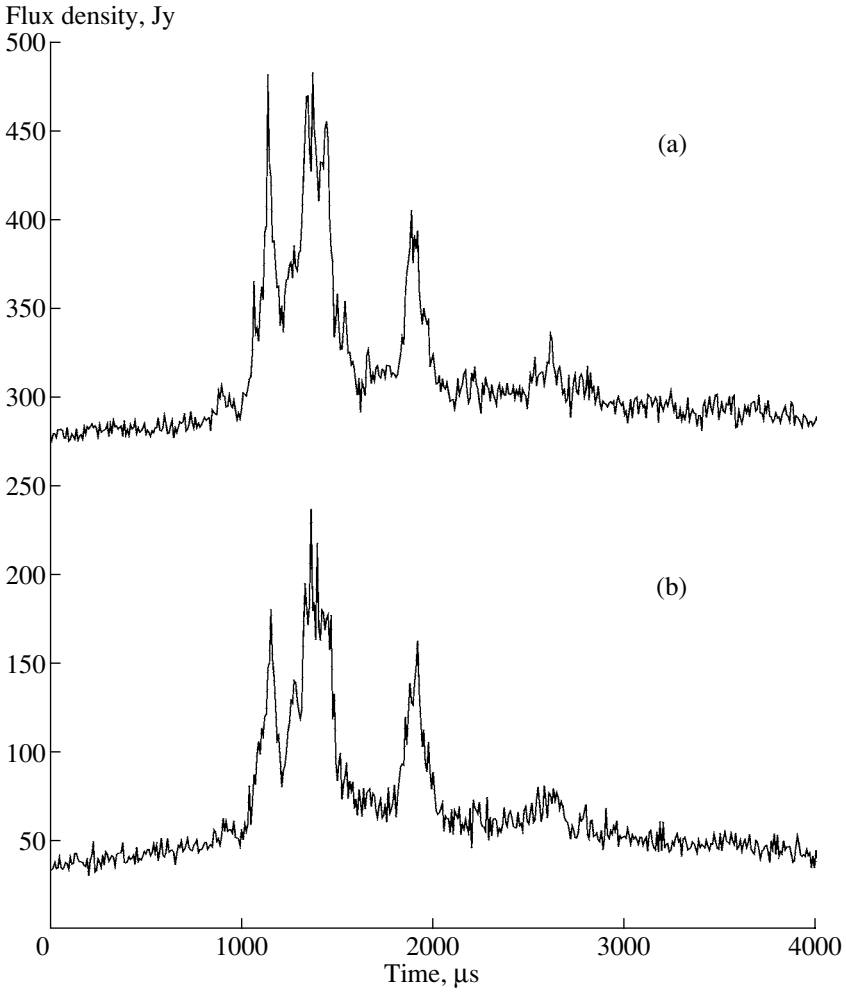

Fig. 1. Example of an individual pulse for B0833 − 45 in the frequency channels at (a) 1650 MHz and (b) 1634 MHz. Pulse smearing due to interstellar dispersion and the time dispersion delay between frequencies have been removed. The intensities shown were averaged with a time constant of 10 μs after detection.

the left panel presents sections of the mean CCFs for time shifts ±4 ms, while the right panel shows the central sections of the same CCFs within 1 ms of the maxima. Table 1 presents the parameters used when calculating and averaging the CCFs.

3.2. Characteristic Timescale for the Microstructure

The characteristic timescale for the microstructure is determined from the mean CCF, from the break where the steep falloff in the central part of the CCF makes a transition to a more gradual decrease with an increase in the time shift. We can see this break in the CCFs for pulsars B0833 − 45, B1749 − 28, and B1933 + 16 in Fig. 2. The CCF for B1641 − 45 does not show signs of the presence of microstructure. The characteristic microstructure timescales τ_μ measured from the observed CCF breaks are presented in Table 2.

This table also gives the characteristic scattering time $\tau_{\rm scat}$ derived by recalculating published data (references given in the table) to a frequency of 1650 MHz using the dependence $\tau_{\rm scat} \propto \nu^{-4}$. A comparison of the characteristic microstructure and scattering timescales for the three pulsars in which microstructure was detected indicates that the former greatly exceed the latter, so they do not require correction for scattering. The scattering time for pulsar B1641 − 45 is about 1.5 ms, and the absence of detectable microstructure in the mean CCF of this pulsar may well be due to the influence of scattering.

3.3. Depth of Modulation of the Microstructure

The depth of modulation of the microstructure can be characterized by the modulation index, which is the square root of the relative amplitude of a microstructure feature in the normalized ACF corrected

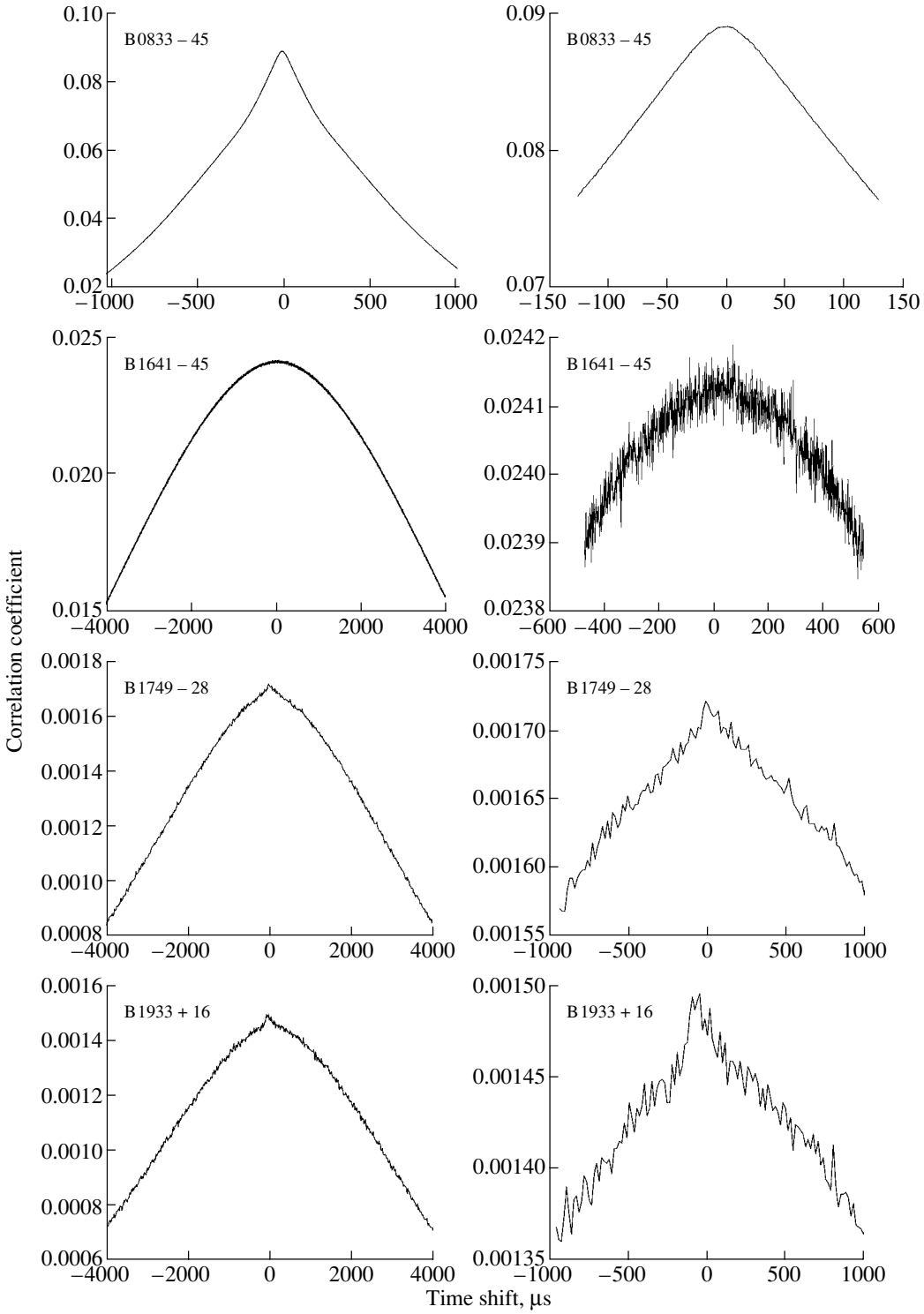

Fig. 2. Mean cross-correlation functions (CCFs) between the intensities of individual pulsar pulses reconstructed using predetection dispersion compensation in the two frequency channels (1634 and 1650 MHz). The CCFs were calculated and averaged with time steps of 31.25 ns; they are shown here after averaging with a time interval of 1 μs. The right-hand part of the figure shows the central parts of the CCFs on an expanded scale.

for noise [6]. According to the model for amplitude-modulated noise [29], the ACF of a pulsar radio pulse extrapolated to zero shift will always be equal to 0.5. Due to the influence of noise and possible decorrelation of the signal, the maxima of the CCFs in our two frequency channels are not equal to 0.5. However,

Table 2. Main parameters derived from our analysis: dispersion measure DM; difference between the observed and calculated time delays between frequency channels $\delta t_{\rm obs} - \delta t_{\rm calcd}$; characteristic microstructure scale τ_μ; characteristic scattering time at 1650 MHz $\tau_{\rm scat}$ calculated using the dependence $\tau_{\rm scat} \propto \nu^{-4}$, with references in the neighboring column; microstructure modulation index m_μ

PSR (B)	DM, pc/cm^3	$\delta t_{\rm obs} - \delta t_{\rm calcd}$, μs	τ_μ, μs	$\tau_{\rm scat}$, μs	Reference	m_μ
0833−45	67.85 ± 0.01	-4.9 ± 0.2	270 ± 10	8	[26]	0.25
1641−45	479.0 ± 0.1	-31.2 ± 2.0		1500	[27]	
1749−28	50.5 ± 0.2	-11.4 ± 7.0	80 ± 10	0.07	[28]	0.07
1933+16	156.7 ± 0.5	-55 ± 15	150 ± 10	2	[28]	0.09

we can determine a multiplicative factor to apply to all the CCF values such that their maxima become equal to 0.5. When determining the microstructure modulation indices, we multiplied the measured amplitudes of microstructure features in the measured CCFs by this factor. The resulting modulation indices are presented in Table 2.

The microstructure modulation index for B0833 − 45 is 0.25, typical also for other pulsars displaying microstructure with timescales of hundreds of microseconds. For example, the modulation indices for B0950 + 08 and B1929 + 10 measured by us earlier at this same frequency (1650 MHz) [17] were 0.31 and 0.26. The microstructure modulation of the radio pulses of B1749 − 28 and B1933 + 16 appear to be the weakest of those measured earlier. Note, however, that the characteristic microstructure timescales for these pulsars are appreciably shorter than that for B0833 − 45, and microstructure with a shorter timescale is also expected to have a lower modulation index. This last assertion will be considered further in Section 3.5. Note also that the short microstructure timescales (about 10 μs) detected earlier for B1133 + 16 and B1929 + 10 [17] have fairly low modulation indices (0.10 and 0.13, respectively).

3.4. Time Delay Between Frequency Channels

The dispersion delay between the 1634 and 1650 MHz frequency channels is about 30 μs for a dispersion measure of 1 pc/cm^3; the dispersion smearing of the pulses in the receiver band is comparable. Realization of the maximum achievable time resolution (62.5 ns) requires knowledge of the dispersion measure to within 0.002 pc/cm^3. None of the dispersion measures of the pulsars studied here were known to this accuracy. When we used the previously determined dispersion measures in Table 1 in the data reduction, the position of the CCF maxima did not correspond to the expected dispersion delay between the frequency channels. The differences between the observed delays and the delays calculated using the previously determined dispersion measures are presented in Table 2, together with the implied corrected values for the dispersion measures.

We estimated the rms error in the position of the CCF maxima using the formula

$$\Delta\delta t_{\rm obs} \sim \frac{4\tau}{\rm SNR}(N_{\rm p}T)^{-1/2},$$

proposed by Chasheĭ and Shishov [30]. Here, τ is the CCF half-width, $N_{\rm p}$ the number of averaged pulses, T the number of points used to calculate the CCF, and SNR the mean signal-to-noise ratio for the given pulsar. For all four pulsars, the observed delays were less than the calculated values, which formally implies the need to decrease the previously determined dispersion measures. For B1749 − 28 and B1933 + 16, which had relatively low SNR values, the measured deviations in the delay lie within $\pm 2.2\sigma$ and $\pm 3.7\sigma$, respectively, while the deviations for B0833 − 45 and B1641 − 45 appreciably exceed the estimated rms errors (24.5σ and 15.6σ, respectively). The dispersion measure for B1641 − 45 was only poorly known (± 5 pc/cm^3), so in principle it is possible to ascribe the deviation in the pulse time delay between channels to the required correction to the dispersion measure. This is not true of B0833 − 45, whose dispersion measure was accurately measured by Manchester [22] based on the positions of the mean pulse profile at 660 and 1700 MHz at epochs (January–March 1999) close to that for our observations (May 1999). Therefore, we conclude that the microstructure in B0833 − 45 with characteristic timescale 270 μs does not follow a strict dispersion smearing law corresponding to the dispersion measure derived earlier from the position of the mean pulse profile. The observed deviation between 1634 and 1650 MHz is -4.9 ± 0.2 μs; i.e., the micropulses arrive 4.9 μs earlier at the lower frequency. Similar deviations implying a need for lower dispersion delays were derived by us earlier for two other pulsars, B0950 + 08 and B1133 + 16 [17], for which the deviations were about 2 μs.

The expectation that the times for the appearance of micropulses at different frequencies should strictly follow the dispersion-delay law for the interstellar

plasma is based on measurements carried out with lower time resolution and a larger difference between frequencies than in our observations. In 1983, Boriakoff [31] showed that the delay in the appearance of micropulses in B1133 + 16 at 196.3 and 318 MHz corresponded to the delay derived from the mean pulse profile to within about 100 μs. The same conclusion was drawn by Popov *et al.* [32] based on their observations of B0809 + 74, B0950 + 08, and B1133 + 16 simultaneously at three frequencies from 67–102 MHz using the DKR-1000 cross radio telescope in Pushchino, for which the accuracy in the time-delay measurements was about 70 μs.

Thus, we believe that the derived deviation in the micropulse arrival times for B0833 − 45 at our two frequencies from the expected interstellar dispersion law is real and reflects the conditions under which the micropulses were formed and propagated through the pulsar magnetosphere.

3.5. Analysis of Individual CCFs for B0833 − 45

Many bright pulses were recorded for B0833 − 45, making it possible to analyze the CCFs for individual pulses in addition to the mean CCF. The individual pulses for B1641 − 45 are not much weaker than those for B0833 − 45; however, in this case, the CCFs for individual pulses do not show any signs of microstructure, which is apparently smeared by scattering on inhomogeneities in the interstellar plasma. The vast majority of individual pulses for B1749 − 28 and B1933 + 16 are not sufficiently strong to enable reliable identification of microstructure features in the individual CCFs against the background noise. The rms noise fluctuations for the cross-correlation functions are $\sigma = 1/\sqrt{Nt}$, where N is the number of points used to calculate the CCF and t is the number of points over which the CCF values were averaged. We chose $N = 524\,288$ for the calculation of the CCFs (Table 1) and averaged the CCFs over 1 μs intervals ($t = 32$); in this case, $\sigma = 0.0002$. We can see in Fig. 2 that the maxima of the CCFs ($A_{\max}$) for B1749 − 28 and B1933 + 16 are about 0.0015, and that the microstructure modulation index m for the mean CCFs for these pulsars is roughly 0.08; in this case, the expected amplitudes of microstructure features in individual CCFs are $m^2 A_{\max} \approx 0.00001$, which is less than σ. Therefore, we limited our analysis of individual CCFs to B0833–45.

Figure 3 presents the central sections of the CCFs for three strong individual pulses for B0833 − 45 as examples. Microstructure is clearly visible in these CCFs: there is a microstructure feature corresponding to a timescale of 20 μs in the left panel, two microstructure scales (50, 300 μs) can be distinguished in the center panel, and the presence of quasi-periodic microstructure with a period of about 500 μs can be seen in the right panel. We measured the microstructure parameters for individual CCFs interactively using a screen display by placing the cursor over the CCF break points. In all, we analyzed 919 CCFs containing 1360 microstructure features (many pulses display several microstructure scales). Some pulses had smooth, structureless CCFs without breaks indicating the presence of microstructure on a particular timescale; this was true of 67 of the 919 pulses analyzed.

The distribution of the characteristic microstructure timescales is presented in the left panel of Fig. 4. We can see that the probability for detecting microstructure with a specified timescale grows for shorter micropulses down to timescales of about 200 μs. Further, the distribution shows a flat maximum from 200 to 20 μs, after which there is a sharp drop toward shorter timescales. The distributions of microstructure timescales analyzed by us earlier for B0950 + 08, B1133 + 16, and B1929 + 10 [17] were characterized by a growth in the probability of detecting microstructure for shorter micropulses right to the shortest timescales measured for these three pulsars—7, 6, and 5 μs, respectively. It is quite possible that the presence of a flat maximum in the microstructure timescale distribution for B0833 − 45 is associated with the influence of scattering on inhomogeneities in the interstellar plasma.

The right panel of Fig. 4 presents the dependence of the microstructure modulation index on the microstructure timescale. The tendency for the modulation index to decrease with decreasing timescale was discovered by us earlier for B0950 + 08, B1133 + 16, and B1929 + 10 [17]. The dependence for B0833 − 45 can be described fairly well by the power-law relation $m \propto \tau_\mu^{0.5}$.

4. DISCUSSION

We have analyzed the time structures of individual pulses for four pulsars with a time resolution of 62.5 ns at 1634 and 1650 MHz. We have detected microstructure for B0833 − 45, B1749 − 28, and B1933 + 16 for the first time and measured its parameters. Only B1641 − 45 did not show any signs of microstructure; however, this pulsar has a very high dispersion measure, and the corresponding characteristic scattering time is about 1.5 ms. Therefore, it is probable that this pulsar's microstructure has been smeared by scattering on inhomogeneities in the interstellar plasma. In our earlier study [17], we presented results for microstructure analyses for the three additional pulsars B0950 + 08, B1133 + 16, and B1929 + 10, obtained using a similar method, with the same resolution, and at the same frequency. All

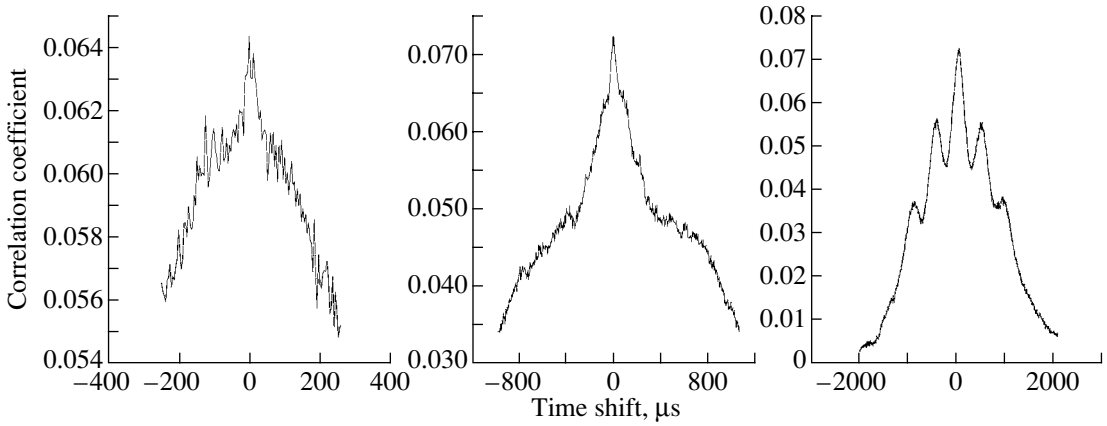

Fig. 3. Examples of CCFs for individual pulses of B0833 − 45. All CCFs were averaged in time over intervals of 1 μs.

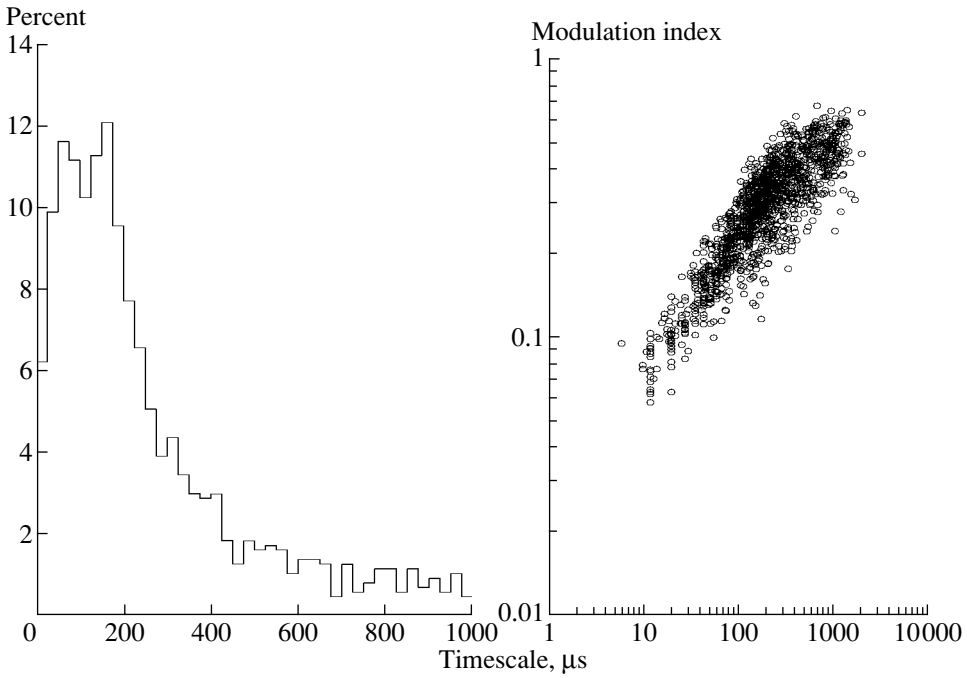

Fig. 4. Distribution of characteristic microstructure scales (left) and the dependence of the microstructure modulation index on the characteristic scale (right) for B0833 − 45.

three pulsars showed well-defined microstructure. We conclude that the presence of microstructure in individual pulses at 1650 MHz is typical of the radio emission of pulsars.

Usually, microstructure is manifest in the mean ACF (CCF) as a break at one or more timescales characteristic of the given pulsar. However, the absence of such a break in the mean ACF does not necessarily testify to an absence of microstructure. Our analysis of individual pulses indicates that each pulsar shows a wide range in its distribution of microstructure scales, and there may not be a dominant scale that gives rise to a break in the mean ACF.

In all the pulsars we have studied, the distributions of microstructure timescales grow toward shorter timescales, then fall off sharply at some minimum timescale. Likewise, all these pulsars display a tendency for the microstructure modulation index (i.e., the amplitude of micropulses) to decrease with decreasing timescale. This behavior is shown most clearly by B0833 − 45 (Fig. 4, right panel).

We have detected deviations in the delays of micropulses between our two frequency channels from the expected dispersion law corresponding to the dispersion measures derived from the mean pulse profiles; the micropulses arrive at the lower frequency

earlier than the calculated time. The deviation for B0833 – 45 is 4.9 ± 0.2 μs. All these properties of the microstructure must be taken into account when developing theoretical models for pulsar-radiation mechanisms and the propagation of the radio emission through the neutron-star magnetosphere. For example, in their study of some aspects of the propagation of the radio emission in the pulsar magnetosphere, Lyutikov and Parikh [33] showed that the time delay due to refraction could reach 10 μs.

Possible mechanisms for the generation of pulsar radio emission can be divided into three groups [34]: coherent curvature radiation by clumps of plasma, intrinsic plasma mechanisms, and maser mechanisms. Models for the formation of short micropulses are based on nonlinear effects arising during interactions between streams of charged relativistic particles and plasma waves in the pulsar magnetosphere. Asseo and coauthors [35, 36] suggest that two-stream instabilities could give rise to a growth in strong plasma turbulence, leading to the formation of compact wave packets forming so-called Langmuir microstructures with timescales of several microseconds. Another interpretation is based on nonlinear models describing the formation of self-consistent instabilities during the propagation of a very strong electromagnetic wave through an electron–positron plasma [37–40]. These models show that self-consistent modulational instabilities can lead to a steady state due to a balance between nonlinear effects and dispersion. Possible steady-state solutions corresponding to the relevant nonlinear equations describe isolated wave packets—solitons—which could be identified with the observed micropulses. Weatherall [41] attempted a numerical simulation of the generation of micropulses based on nonlinear wave dynamics; this model can form micropulses with durations from 1 to 10 ns.

One characteristic feature of these nonlinear models is the prediction of a dependence between the duration and intensity of micropulses such that shorter micropulses are stronger. Our analysis has revealed the opposite dependence: shorter micropulses have lower amplitudes than longer ones (Fig. 4, left panel). Therefore, we are forced to conclude that, at least in their current form, nonlinear models do not provide an adequate description of some of the observed properties of micropulses. In our view, the characteristics of microstructure reflect the spatial (radial) flow structure of the turbulent relativistic plasma in the regions in which the radio emission is generated and through which it propagates.

5. ACKNOWLEDGMENTS

This work was supported by the Russian Foundation for Basic Research (project no. 01-02-16871). The Deep Space Network radio telescopes are operated by the Jet Propulsion Laboratory of the California Institute of Technology under contract to the National Aeronautics and Space Administration.

REFERENCES

1. T. H. Hankins, Astrophys. J. **169**, 487 (1971).
2. T. H. Hankins, Astron. Astrophys., Suppl. Ser. **15**, 363 (1974).
3. T. H. Hankins, *Pulsars: Problems and Progress,* Ed. by S. Johnston, M. A. Walker, and M. Bailes, Astron. Soc. Pac. Conf. Ser. **105**, 197 (1996).
4. T. H. Hankins, Astrophys. J. Lett. **177**, L11 (1972).
5. J. M. Cordes, Astrophys. J. **195**, 193 (1975).
6. J. M. Cordes, Astrophys. J. **208**, 944 (1976a).
7. V. Boriakoff, Astrophys. J. Lett. **208**, L43 (1976).
8. N. S. Kardashev, A. D. Kuzmin, N. Ya. Nikolaev, *et al.*, Astron. Zh. **55**, 1024 (1978) [Sov. Astron. **22**, 583 (1978)].
9. V. A. Soglasnov, T. V. Smirnova, M. V. Popov, and A. D. Kuzmin, Astron. Zh. **58**, 771 (1981) [Sov. Astron. **25**, 442 (1981)].
10. V. A. Soglasnov, M. V. Popov, and O. A. Kuzmin, Astron. Zh. **60**, 293 (1983) [Sov. Astron. **27**, 169 (1983)].
11. J. M. Cordes, Astrophys. J. **210**, 780 (1976b).
12. J. M. Cordes, J. M. Weisberg, and T. H. Hankins, Astron. J. **100**, 1882 (1990).
13. N. Bartel, Astron. Astrophys. **62**, 393 (1978).
14. N. Bartel and T. H. Hankins, Astrophys. J. Lett. **245**, L35 (1982).
15. T. V. Smirnova, S. A. Tul'bashev, and V. Boriakoff, Astron. Astrophys. **286**, 807 (1994).
16. S. Johnston, W. van Straten, M. Kramer, and M. Bailes, Astrophys. J. Lett. **549**, L101 (2001).
17. M. V. Popov, N. Bartel, W. H. Cannon, *et al.*, submitted to Astron. Astrophys.
18. H. Hirabayashi and H. Hirosawa, Adv. Space Res. **26**, 589 (2000).
19. W. H. Cannon, D. Baer, G. Feil, *et al.*, Vistas Astron. **41**, 297 (1997).
20. R. D. Wietfeldt, W. van Straten, D. Del Rizzo, *et al.*, Astron. Astrophys., Suppl. Ser. **131**, 549 (1998).
21. J. C. Kempner, D. R. Stinebring, M. Bailes, *et al.*, in *Meeting of the American Astronomical Society, 1997,* Vol. 191, No. 111.19.
22. R. N. Manchester, private communication (2001).
23. S. Johnston, A. G. Lyne, R. N. Manchester, *et al.*, Mon. Not. R. Astron. Soc. **255**, 401 (1992).
24. A. G. Lyne and B. J. Rickett, Nature **218**, 326 (1968).
25. R. N. Manchester, Astrophys. J. **172**, 43 (1972).
26. J. A. Roberts and J. G. Ables, Mon. Not. R. Astron. Soc. **201**, 1119 (1982).
27. J. M. Cordes, J. M. Weisberg, and V. Boriakoff, Astrophys. J. **288**, 221 (1985).
28. J. M. Cordes, Astrophys. J. **311**, 183 (1986).
29. B. J. Rickett, Astrophys. J. **197**, 185 (1975).
30. I. V. Chasheĭ and V. I. Shishov, Pis'ma Astron. Zh. **1**, 18 (1975) [Sov. Astron. Lett. **1**, 9 (1975)].
31. V. Boriakoff, Astrophys. J. **272**, 687 (1983).

32. M. V. Popov, T. V. Smirnova, and V. A. Soglasnov, Astron. Zh. **64**, 1013 (1987) [Sov. Astron. **31**, 529 (1987)].
33. M. Lyutikov and A. Parikh, Astrophys. J. **541**, 1016 (2000).
34. D. B. Melrose, *The Magnetospheric Structure and Emission Mechanisms of Radio Pulsars,* Ed. by T. H. Hankins, J. M. Rankin, and J. A. Gil (Pedagogical Univ. Press, Zielona Gora, 1992), p. 306.
35. E. Asseo, G. Pelletier, and H. Sol, Mon. Not. R. Astron. Soc. **247**, 529 (1990).
36. E. Asseo, Mon. Not. R. Astron. Soc. **264**, 940 (1993).
37. A. C. L. Chian and C. F. Kennel, Astrophys. Space Sci. **97**, 9 (1983).
38. O. G. Onishchenko, in *Proceedings of the Joint Varenna–Abastumani–ESA–Nagoya–Potsdam Workshop on "Plasma Astrophysics," 1990,* ESA SP-311, p. 251.
39. A. C. L. Chian, *The Magnetospheric Structure and Emission Mechanisms of Radio Pulsars,* Ed. by T. H. Hankins, J. M. Rankin, and J. A. Gil (Pedagogical Univ. Press, Zielona Gora, 1992), p. 356.
40. R. T. Gangadhara, V. Krishan, and P. K. Shukla, Mon. Not. R. Astron. Soc. **262**, 151 (1993).
41. J. C. Weatherall, Astrophys. J. **506**, 341 (1998).

Translated by D. Gabuzda

Astronomy Reports, Vol. 46, No. 3, 2002, pp. 216–223. Translated from Astronomicheskiĭ Zhurnal, Vol. 79, No. 3, 2002, pp. 240–248.

A Magnetized Disk around an O Star: Polarization of the OH Maser Emission

V. I. Slysh[1], I. E. Val'tts[1], and V. Migenes[2]

[1]*Astro Space Center, Lebedev Physical Institute, Russian Academy of Sciences, Profsoyuznaya ul. 84/32, Moscow, 117810 Russia*

[2]*University of Guanajuato, Department of Astronomy, Apdo Postal 144, Guanajuato, GTO, CP36000 Mexico*

Received April 15, 2001

Abstract—W75N is one of the first OH masers in which 100% linear polarization has been observed in several spots. Two spots contain Zeeman pairs, corresponding to magnetic fields of 5.2 and 7.7 mG. Another Zeeman pair consisting of two linearly polarized components was tentatively detected in one spot. The linearly polarized spots are σ components for the case when the magnetic field is perpendicular to the line of sight. For these spots, the magnetic field is perpendicular to the plane of the circumstellar disk, though a correction for Galactic Faraday rotation may considerably modify this conclusion.

1. INTRODUCTION

OH maser emission is strongly polarized, usually circularly, though some masers have an admixture of linear polarization, which is a component of elliptic polarization. The importance of polarized OH-maser features lies in the physics of maser excitation and saturation properties. Modern theories for the polarization of OH masers require the presence of a magnetic field of a few milligauss in the emission region. This value is three orders of magnitude greater than the intensity of the magnetic field in the Galaxy, but is comparable to that estimated for a density of 10^6–10^7 cm^{-3} if the interstellar gas and magnetic field are compressed. Determining the intensity and direction of the magnetic field would help us to understand its role in the formation of interstellar disks or shock fronts at interfaces between compact H II regions and surrounding molecular clouds.

The polarization properties of OH maser emission are predicted in theoretical models based on Zeeman splitting [1]. If the Zeeman splitting exceeds the linewidth ($B > 0.5$ mG), three 100%-polarized components should be observed: a nonshifted π component, linearly polarized parallel to the direction of the magnetic field projected onto the celestial sphere, and two 100% elliptically polarized σ components, displaced in frequency and located on either side of the π component. The relative intensity of the π component and degree of ellipticity depend on the angle θ between the line of sight and magnetic field. If $\theta = \pi/2$, the π component is maximum and the σ components are linearly polarized and are perpendicular to the magnetic field. If $\theta = 0$, the π-component intensity is zero and the σ components have opposite circular polarizations. If $0 < \theta < \pi/2$, the π component is linearly polarized, is aligned with the magnetic field, and has an intermediate intensity, while the σ components are elliptically polarized with the major axis of the ellipse being perpendicular to the magnetic field. Such a pattern, with all the features described above, has never been observed in OH masers. Usually, strong circular polarization with only one sense is observed in individual maser spots. In some cases, circular polarization with opposite senses has been observed from a single maser spot, in which case the line components were interpreted as a Zeeman pair. Linear polarization has been observed only rarely, and usually only as a component of elliptically polarized emission. The best studied source of polarized OH emission is the maser W3(OH), in which García-Barreto *et al.* [2] found several dozen circularly polarized features, 16 of them elliptically polarized. Only three features had a higher degree of linear than circular polarization; the maximum degree of linear polarization was 46%. Five Zeeman pairs were identified. García-Barreto *et al.* [2] concluded that none of the features detected could be identified as a π component. The majority of the features were single and circularly polarized. In a similar polarization study of G35.02–0.74N with lower angular resolution, Hutawarakorn and Cohen [3] found 25 circularly polarized spectral features; four were Zeeman pairs and five features showed linear polarization, with

1063-7729/02/4603-0216$22.00

the maximum degree of the linear polarization being 63%. These were interpreted as σ components.

W75N is another well-studied OH maser, associated with a star-forming region and ultracompact H II region at a distance of 2 kpc [4]. VLBI mapping in the main OH line at 1665 MHz revealed nine maser spots in an extended region 1.5″ in size [5]. Single-dish polarization measurements [5] detected polarization from several of the maser spots in the VLBI map and isolated two Zeeman pairs with circular polarizations of opposite senses in the spectrum. Polarization studies of W75N with high angular resolution were carried out using the MERLIN array [6]. Baart *et al.* [6] also detected several Zeeman pairs that were circularly polarized with opposite senses, which were cospatial within the errors. In addition, Baart *et al.* [6] suggested that seven linearly polarized components were present in the spectrum, based on the fact that some spectral features represented circularly polarized pairs with opposite senses formed in the same region and having identical line-of-sight velocities, in contrast to pairs in which the velocities are different. However, no cross-correlation measurements were done in these observations, which are required to estimate the degree of linear polarization. The prevalence of circular polarization and the low level of linear polarization is a problem that have long existed in the theory of maser polarization. Goldreich *et al.* [1] suggested that Faraday rotation in the emission regions may destroy linear polarization so that only circular polarization remains. If the linear polarization detected by Baart *et al.* [6] is real, this result can be used to test polarization models. The polarization structure of OH masers may be smeared by poor spectral and spatial resolution if several adjacent features are blended. Baart *et al.* [6] observed with an angular resolution of 280 mas and spectral resolution of 0.3 km/s, which is not sufficiently high, as will be clear from our results.

In the current paper, we report new polarization studies of W75N with higher angular and spectral resolution and with a full polarization analysis including all the Stokes parameters. This makes it possible to exclude any mutual influence of spectral features. In addition, we have mapped W75N for the first time in the other main OH line at 1667 MHz.

2. POLARIZATION MAP OF W75N

2.1. Polarization of Maser Spots

All maser spots whose parameters are listed in Table 1 [7] were mapped in all Stokes parameters. This enabled us to determine the full polarization properties of the maser spots. The degree of circular polarization in percent in Table 1 was calculated as

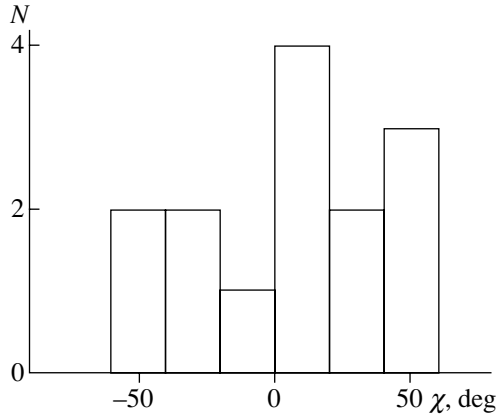

Fig. 1. Distribution of position angles χ of the linear polarization for maser spots in W75N. $\bar{\chi} = 4^\circ \pm 17^\circ$.

$$m_C = 100\frac{V}{I}. \quad (1)$$

Positive V corresponds to right-hand circular polarization. The degree of linear polarization was calculated as

$$m_L = 100\frac{\sqrt{Q^2 + U^2}}{I} \quad (2)$$

and the position angle of the electric vector of linear polarization was calculated as

$$\chi = \frac{1}{2}\arctan\frac{U}{Q} \quad (3)$$

with the position angle increasing from the north toward the east. The quantities I, Q, U, and V are the Stokes parameters at the peak of the map of the corresponding maser spot (in Jy/beam). In some cases, the degree of polarization exceeds 100%. This could be due to position offsets of the peaks in different Stokes parameters, and also to errors in the intensity measurements.

It follows from the table that all the maser spots are strongly polarized, up to 100%. There are two types of maser spots. The first includes spots that are strongly linearly polarized ($m_L > 70\%$): E, F, G, H, J, K. The polarization of the spots in this group is not purely linear, and includes a small admixture of circular polarization, making the overall polarization elliptical. The degree of circular polarization varies from less than 0.3 to 80%. Baart *et al.* [6] proposed some candidate linearly polarized components based on the small positional differences and identical velocities for some pairs with opposite circular polarizations. Here, we have a full polarization information and much higher accuracy for the spot positions,

making it possible to confirm or reject the candidate features of Baart *et al.* [6]. Our analysis confirms five of the seven candidates initially identified in MERLIN data: J = A, A; G = F, C; F = G, D; E = H, E; A, B = N, K. The first letter is the designation in Table 1 from [7], and the last letter the designation of Baart *et al.* [6]. The other two candidates, D, B and M, J, are not present in our data. Spot A, B = N, K is polarized, mainly circularly, with a degree of linear polarization of only 9.3%. There is also a pair of oppositely polarized spectral features at a velocity of 9.35 km/s in the spectrum, which resembles a linearly polarized feature suitable for calibration, but it is absent from the cross-correlation spectrum (see Fig. 2a in [7]). This means that the left- and right-hand circular (LHC and RHC) polarizations come from different, spatially separated condensations, as is confirmed by mapping (feature B, C in Table 1 [7]). Two independent maser spots with opposite circular polarizations have coincident radial velocities by chance. Their blended line could be interpreted as a linearly polarized feature in the absence of a full polarization analysis and high-resolution mapping. Only one linearly polarized spot is present in the 1667-MHz transition, with a degree of linear polarization of 41.6% and degree of circular polarization of 23%.

For the spots of this group, the position angle of the linear polarization vector lies in the interval from $-23°$ to $+23°$, with the average value $3.9° \pm 17°$ (Fig. 1). This vector is perpendicular to the major axis of the maser spots, which have an average position angle of $93° \pm 28°$. This correlation between the direction of the major axis and the linear polarization vector makes it more probable that the alignment of the maser spots has an internal origin and is closely associated with the direction of the magnetic field responsible for the polarization of the maser-spot emission. Figure 2 presents maps of the polarized and total intensities for some of the linearly polarized spots.

Another group of spots includes those whose emission is strongly circularly polarized, with an admixture of linear polarization (spots A–D, I, M, N, O). The degree of circular polarization in these spots is close to 100%, while the degree of linear polarization is less than 5–17.9%; only spot L has intermediate linear and circular polarizations.

2.2. Identification of Zeeman Pairs

Spots A and B at 1665 MHz as well as M and O at 1667 MHz are observed at the same position. The offsets between them are 0.8 and 1.1 mas respectively, which is less than the beamwidth and spot size. Figure 3 shows the total-intensity map of spot A (grey scale) and the difference of the intensities of the RHC and LHC polarization maps; the peak intensity in the LHC polarization is made equal to the peak intensity in the RHC polarization by multiplying by an appropriate factor. In this figure, positive values are shown by solid contours and negative values by dashed contours. The difference between the two circular-polarization intensities is zero at the total-intensity peak. Small residual intensities toward the northeast (positive) and southeast (negative) of the peak have appeared due to a 0.6-mas offset in right ascension and declination of the beam in RHC polarization relative to the beam in LHC polarization; this is a consequence of small calibration errors. This map illustrates the spatial coincidence of the RHC and LHC polarizations of spots with different radial velocities within the errors, which are of the order of 1 mas, and confirms the Zeeman origin of the splitting into two oppositely polarized spectral features.

The polarization of the features is circular, with two opposite senses in each spot with velocity differences within the pairs of 3.07 and 2.7 km/s, respectively. Based on these properties, we can identify the two pairs as $\sigma\pm$ Zeeman components with magnetic fields of 5.2 and 7.7 mG, respectively (a positive sign corresponds to field directed away from the Earth). Both pairs are elliptically polarized and the position angles of the polarization are approximately the same, as is required for σ components. Nevertheless, there are differences from the theoretically expected pattern for Zeeman pairs. For example, the intensities of the RHC and LHC polarized emission are not equal. The ratio of the intensities of the circularly polarized features is 5 for pair A, B and 1.8 for pair M, O. The linearly polarized intensities are also different, with the ratio being 2.2 for pair A, B and 1.2 for pair M, O.

Another important deviation from the theoretical Zeeman pattern is the complete absence of the π component. In a Zeeman pair, the π component should be present at the average velocity of the pair. We carried out careful searches for π components in the two Zeeman pairs and detected no emission exceeding the noise level between the σ components in the two Zeeman pairs—A, B at 10.9 km/s and M, O at 7.3 km/s. In addition, the π components should be linearly polarized, and we have found the emission from each maser spot to be elliptically polarized. The only spot in which circular polarization was not found is spot E. Therefore, we conclude that there is no π component in the Zeeman spectrum of the OH maser W75N. Baart *et al.* [6] suggested the presence of several Zeeman pairs, which is not confirmed in our study. For the pair at radial velocities of 3.8 km/s (LHC) and 6.5 km/s (RHC) proposed

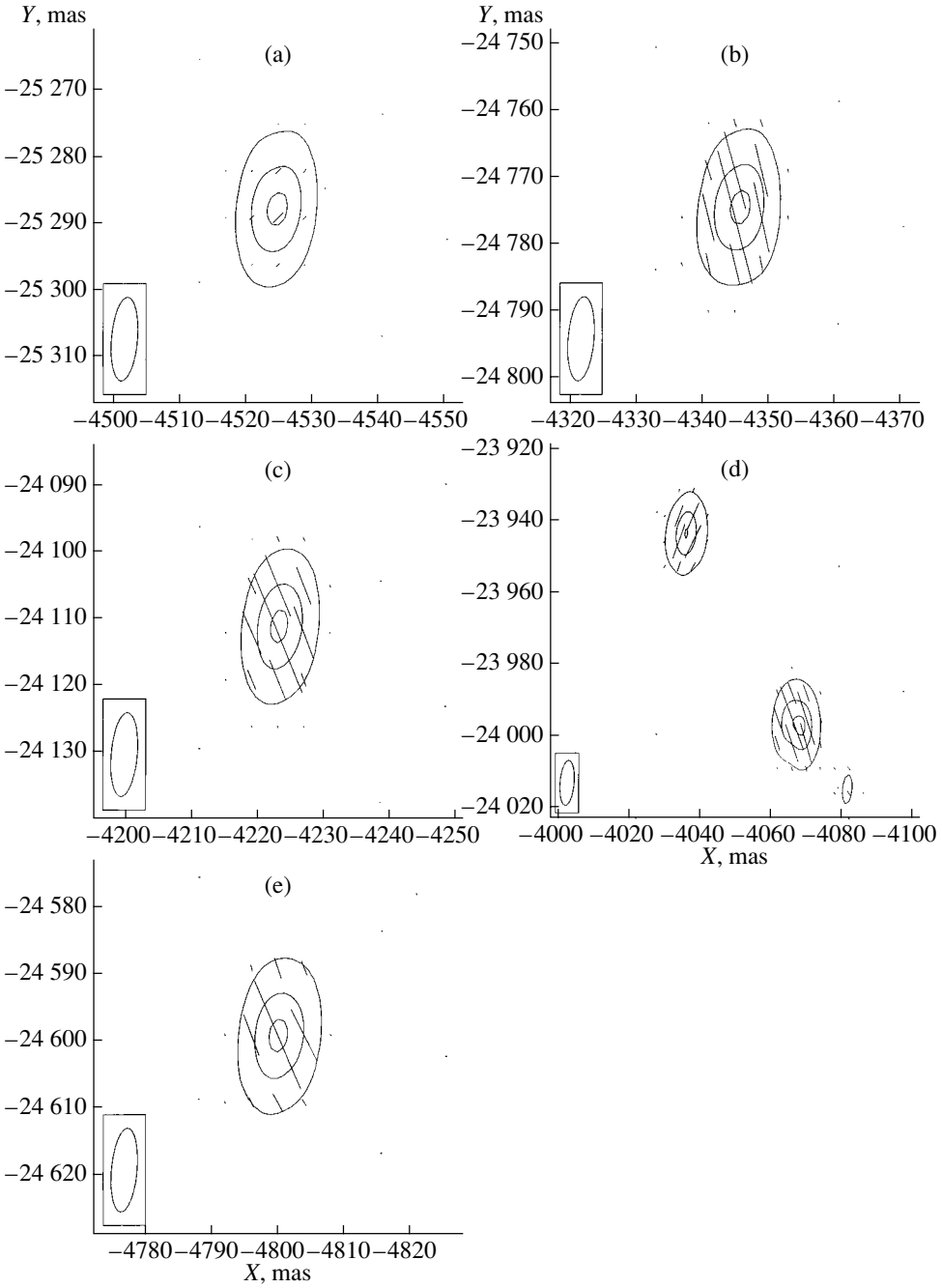

Fig. 2. Maps of the linearly-polarized and total intensity of maser spots in W75N. The sticks show the linear polarization, with their being proportional to the linearly-polarized intensity and their orientation corresponding to the position angle of the linear polarization. The contours show the total intensity at levels 0.1, 0.5, and 0.9 × the peak intensity. (a) Spot A, peak value $\sqrt{Q^2+U^2} = 1.6$ Jy/beam, $I = 16.9$ Jy/beam; (b) spot E, $\sqrt{Q^2+U^2} = 5.4$ Jy/beam, $I = 5.8$ Jy/beam; (c) spot F, $\sqrt{Q^2+U^2} = 9.9$ Jy/beam, $I = 10.2$ Jy/beam; (d) spots G and H, $\sqrt{Q^2+U^2} = 3.0$ Jy/beam, $I = 3.3$ Jy/beam (G), $\sqrt{Q^2+U^2} = 2.0$ Jy/beam, $I = 29$ Jy/beam (H); (e) spot L, $\sqrt{Q^2+U^2} = 8.9$ Jy/beam, $I = 21.3$ Jy/beam.

by Baart *et al.* [6], we have confirmed only the LHC component, with the LHC/RHC ratio exceeding 28; the LHC/RHC ratio in the pairs of Baart *et al.* [6] is five. For another Zeeman pair proposed by Baart *et al.* [6], with velocities of 4.8 km/s (LHC) and 9.6 km/s (RHC), we could not find the corresponding LHC component, implying a RHC/LHC ratio greater than 350, while Baart *et al.* [6] give RHC/LHC = 12.

Haschick *et al.* [5] suggested the presence of two other Zeeman pairs, which are also absent from

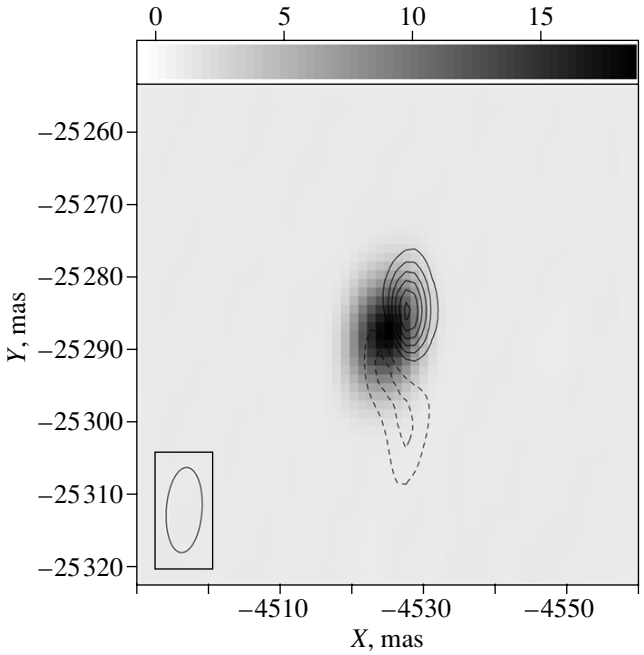

Fig. 3. Superposition of the maps of spots A and B: RCP(A) × 0.226 − LCP(B). Positive and negative values are shown by solid and dashed contours, respectively. The grey scale shows the total intensity I of spot A, whose peak value is 18.5 Jy/beam.

our spectra. The discrepancy between our data and the earlier results may be due to variability of the Zeeman-component intensities. In no pair did we see identical intensities of the σ components, and the intensity ratio may vary appreciably. If the intensity ratio of the σ components is very large, the weaker component becomes undetectable. This may explain the presence of only one circularly polarized spectral feature in the OH masers.

2.3. Polarization Status

Figure 4 shows the degree of circular polarization as a function of the degree of linear polarization for all the spots. The spots are labeled with the same letters as in Table 1 [7]. The dashed curve shows the circle on which completely polarized features should lie. Most spots are located near this 100% polarization curve. An obvious exception is spot L (1667 MHz), which is polarized 47%. A clearly trend is that the spots are either mainly circularly polarized and located in the top and bottom left corners of the diagram, or are mainly linearly polarized and are located to the right, in the middle of the diagram. The numbers on the dashed curve correspond to the angle θ between the line of sight and the magnetic field according to the relations

$$m_L = 100\frac{\sin^2\theta}{1+\cos^2\theta}, \quad m_C = \pm 100\frac{\cos\theta}{1+\cos^2\theta}. \quad (4)$$

These equations describe the polarization of the σ components in the theory of Goldreich *et al.* [1] for the case when the Zeeman splitting exceeds the linewidth (see also [8]). Most of the maser spots occupy two regions in the diagram: $\theta < 30°$ and $80° < \theta < 90°$. If all the spots are σ components, this means that the line of sight is either parallel or perpendicular to the magnetic field, and that there are no intermediate cases. The spots that are mainly circularly polarized are almost definitely σ components, though frequently without the second member of the pair. The spots that are mainly linearly polarized are either σ components for which $\theta \approx 90°$ or π components. It is very important to determine the direction of the magnetic field correctly: it is parallel to the E vector for π components and perpendicular to the E vector for σ components. As noted in Section 1, an admixture of a small amount of circular polarization makes these components elliptically polarized, so they should be σ components, since π components can have no contribution from circular polarization.

The single linearly polarized spot L at 1667 MHz is clearly not polarized 100% and is an exception among the maser spots in W75N. In a model with a weak magnetic field, the degree of linear polarization for $\sin^2\theta > 1/3$ is [1]

$$m_L = 100\frac{3\sin^2\theta - 2}{3\sin^2\theta}. \quad (5)$$

For this spot, $m_L = 41.6\%$ with $\theta = 43°.4$. The degree of circular polarization changes across the line

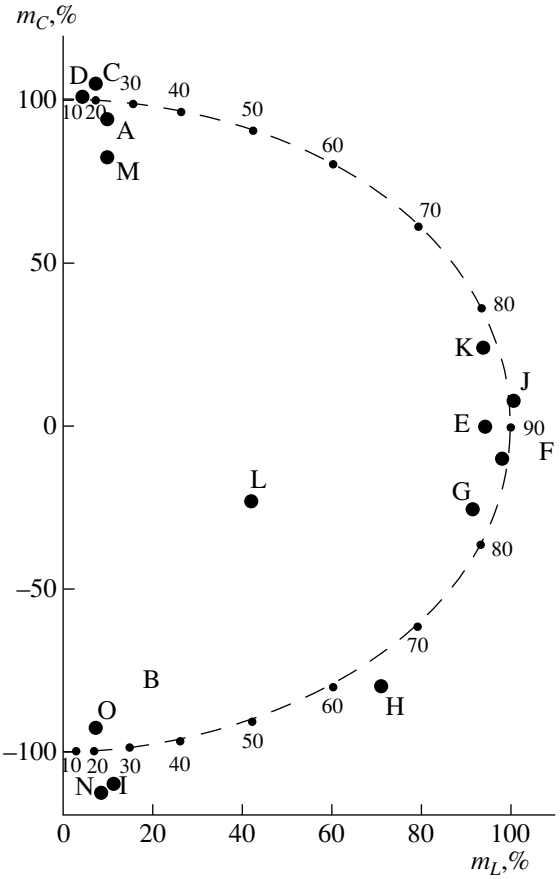

Fig. 4. Degree of circular polarization m_C of maser spots in W75N as a function of the degree of linear polarization m_L. Completely polarized features should lie on the dashed curve. Negative values of m_C indicate LHC polarization or elliptical polarization, and correspond to negative values of V in Table 1 from [7].

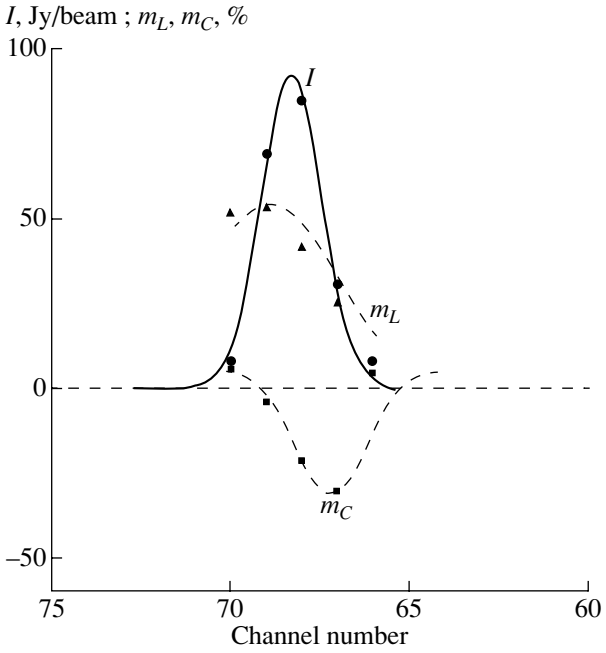

Fig. 5. 1667-MHz OH line profile for spot L. The solid curve and circles show the total intensity I, dashed curve and triangles the degree of linear polarization m_L, and dashed curve and squares the degree of circular polarization m_C.

profile (Fig. 5), reversing its sign, as predicted by the theory for the case of small splitting [8]. However, the circular-polarization profile is shifted and strongly distorted in comparison with the theoretical profile, probably due to nonlinear mode competition in the maser. The linear polarization grows toward the red side of the line profile, whereas the circular polarization is greater on the blue side.

3. DISCUSSION

3.1. Linear Polarization

The most important result of this work is the discovery of several linearly polarized maser spots having degrees of polarization of almost 100%. The existence of linear polarization in both these spots and circularly polarized spots means that Faraday rotation, proposed as a mechanism suppressing π components [1], does not play an important role in the OH maser W75N. The linearly polarized components are σ components in Zeeman groups. This conclusion can be verified if the second σ component of the Zeeman pair, with linearly polarized emission displaced in radial velocity by the necessary amount, is detected. We have tentatively found the Zeeman counterpart for linearly polarized feature F. It is displaced in radial velocity by 6.3 km/s (corresponding to a magnetic field intensity of 10.7 mG) and is almost completely linearly polarized, with a position angle close to that of spot F. This suggests an interpretation of these two features as σ components of spots F and F1. However, this must be confirmed by more sensitive measurements, since the detection of component F1 is not reliable; its intensity is only 0.003 of the intensity of component F. This is not surprising, since Zeeman pairs always have unequal component intensities, but component F1 has also been detected at the edge of the receiver spectral band, in the last (128th) channel. The linearly polarized Zeeman counterparts may be too weak to be detectable. A difference in the intensities of the Zeeman σ components may be a common property of OH masers, possibly associated with gradients of the velocity and magnetic field [9]. It is more difficult to explain the absence of the π component. As we emphasized above, internal Faraday rotation cannot be responsible for this result. In the model calculations of masers carried out by Gray and Field [10], both π and

σ components are obtained, and the σ components dominate over π components at angles $\theta = 0°–55°$, where the σ components are polarized circularly or elliptically. At angles $\theta = 55°–90°$, π components dominant and are linearly polarized. The effects of saturation due to mode competition strongly suppress the intensity of the weaker component; i.e., the π component for angles $\theta = 0°–55°$ and the σ component for angles $\theta = 55°–90°$. Gray and Field [10] noted that suppression of the σ component is much less efficient than suppression of the π component by σ components. The model of Gray and Field [10] contradicts our conclusion that linearly polarized spots in W75N radiate as σ components at angles θ close to 90°; the model predicts the dominance of linearly polarized π components for angles θ close to 90°. Our identification of the linearly polarized spots as σ components is based on the presence of some degree of circular polarization in all spots except for spot E. This is a very strong argument that these features are σ components, at least until another scenario allowing a contribution of circular polarization to π components can be found.

An alternative explanation of the observed linear polarization is that it results from saturated maser amplification in a weak magnetic field, where the Zeeman splitting is smaller than the linewidth. For $\sin^2\theta \leq 1/3$, or $\theta \leq 35.^\circ5$, there is only one 100% linearly polarized line with its E vector parallel to the magnetic field (case 2a in [1]). For $\theta > 35.^\circ5$, the linear polarization will be weaker, and circular polarization will be visible in the line wings (see Section 2.7). This model could explain the linear polarization in W75N, but the observed admixture of circular polarization remains unexplained, as in the π components of the Zeeman splitting. This model imposes a constraint on the magnetic-field intensity, which should not exceed 0.5 mG; this is much smaller than the value obtained for spots A, B, F, F1 and M, O (see Section 2). It is more likely that this explanation is applicable to the observed linear polarizations of methanol and H_2O masers. Finally, if confirmed, the detection of the Zeeman counterpart F1 for spot F will testify that linearly polarized features can be interpreted as σ components of Zeeman groups.

3.2. Nature of the Maser Spots

In W75N, we have mapped 14 maser spots (see Fig. 5 in [7]), of which two or possibly three have coincident Zeeman components. Each maser spot has its own radial velocity, distinct from those of other spots, and corresponds to a narrow feature with a width of about 0.2–0.3 km/s. The spots radiating at 1667 MHz are not positionally coincident with those radiating at 1665 MHz. Nearly every spot has 100% elliptical polarization. We interpret them as the σ components of Zeeman groups. The magnetic field in the Zeeman pairs is from 5 to 11 mG, the same value derived for other OH masers [2]. We suggest that the magnetic-field intensity is of the same order in other spots, in which the second σ component is not seen. Maser spots in W75N are partially resolved in VLBA observations, with typical sizes of 5–10 mas, or 10–20 AU at a distance of 2 kpc. The spots are elongated, with the dominant position angle of the major axis of the structural ellipse being about 90°, whereas the position angle of the polarization electric vector is about 0°; i.e., it is perpendicular to the major axis of the structural ellipses of the spots. The axis ratio is ten or greater; i.e., the spots form long, thin filaments. If they are σ components, the linear polarization vector should be perpendicular to the magnetic field, and the direction of the magnetic field coincides with that of the filaments' major axis.

This is valid for all the maser spots, as follows from the histograms given in Fig. 6 of [7] and in Fig. 1 of this paper. Unfortunately, the direction of the magnetic field cannot be reliably determined from linear polarization measurements, due to uncertainty in the Galactic Faraday rotation in the direction of the maser sources. The OH masers are located in the Galactic disk, where the Faraday rotation is maximum. The total Faraday rotation in the Galactic plane measured for extragalactic sources follows the formula

$$\mathrm{RM}(l) = \mathrm{RM}_0 \sin(l_0 - l), \qquad (6)$$

where $\mathrm{RM}_0 = 1607$ rad m^{-2} and $l_0 = 62.1°$ [11]. The Galactic longitude of W75N is $l = 81.9°$, and we obtain from (6) RM $= -544$ rad m^{-2}, with an uncertainty of 10%.

At the wavelength of the OH emission ($\lambda =$ 18 cm), the Faraday rotation is $(-544) \times (0.18)^2 = -17.6 \pm 1.8$ rad. This is the total Faraday rotation in the Galactic disk; the distance to W75N (2 kpc) is probably about half the total effective path through the disk. Therefore, the Faraday rotation in W75N could be half this value, or about -9 ± 0.9 rad. This is a large rotation, roughly three complete revolutions, and correction of the position angle of the linearly polarized components could introduce a large uncertainty. Therefore, it is not possible to determine the direction of the magnetic field in the OH maser spots.

3.3. Model of the W75N region

The OH maser spots in W75N are located around the ultracompact H II region VLA1. Spots J and K may be associated with the ultracompact region VLA2 (see Fig. 5 in [7]). In one model, the OH masers lie at a D-type ionization front [13] or in

a photodissociation zone [14] surrounding the H II region. The geometry of the maser spots in W75N is consistent with this model, though the model does not predict the observed radial-velocity gradient along the chain of maser spots—from 10 km/s in spots A, B to 3.7 km/s in spot I. This gradient is more consistent with outflow or disk models. Based on the elongated shape of the ultracompact H II region VLA1 and the fact that the chain of H_2O and OH maser spots is oriented parallel to the bipolar flow observed in W75N on larger scales, Torrelles *et al.* [15] proposed that the masers trace the the outflow on scales of about 1″ and that VLA1 is the energy source of the bipolar outflow. Our higher precision measurements of the absolute positions of the OH masers show that they are not projected onto VLA1 (Fig. 7 in [15]) but are instead shifted, forming an arch around VLA1. The H_2O masers appear to form an arch closer to VLA1. This geometry is better described by a disk around VLA1, in which the OH maser spots are located about 2000 AU from VLA1, and the H_2O masers are a factor of two to five closer. Such a disk model was first proposed by Haschick *et al.* [5]. VLA1 marks the position of the ionization source and center of gravity of the system. We suggest (Section 3.2) that there may be an O9 star with a mass of $20M_\odot$ at the center of VLA1, which gravitationally confines a disk with a radius of 2000 AU. In this model, the elongated shape of VLA1 reflects the distribution of matter in the disk, which becomes visible at radio wavelengths due to ionization by the central star. The OH maser spots are also elongated, and their orientation is approximately perpendicular to the disk. We cannot determine the direction of the magnetic field in the disk from the linear-polarization data due to uncertainty in the Faraday rotation in the Galaxy (see Section 3.2), but we can establish that the orientation of the magnetic field is not random and that the field is well organized in some direction, as follows from the histogram in Fig. 6 in [7].

4. CONCLUSIONS

One result of this study is the discovery of several linearly polarized maser spots, having degrees of polarization of almost 100%.

We have obtained the first polarization map of W75N in the second main line of OH at 1667 MHz.

Spots A and B at 1665 MHz and spots M and O at 1667 MHz have the same coordinates. They are circularly polarized in opposite directions, and their position offset is smaller than the measurement error. Based on these properties, we identify the two pairs as $\sigma\pm$ components of Zeeman groups. Both pairs are elliptically polarized and have very similar polarization position angles, as is required for σ components. The two maser spots to which these Zeeman pairs belong have magnetic fields of 5.2 and 7.7 mG.

In linearly polarized maser spots, σ components arise if the line of sight is perpendicular to the magnetic field. We have tentatively detected a Zeeman pair consisting of linearly polarized components with a magnetic field of 10.7 mG. The magnetic-field direction uncorrected for Galactic Faraday rotation is perpendicular to the disk plane, as determined from the linearly polarized spots.

ACKNOWLEDGMENTS

V.I.S. and I.E.V. gratefully acknowledge partial support from the Russian Foundation for Basic Research (project no. 01-02-16902) and INTAS (grant no. 97-11451).

REFERENCES

1. P. Goldreich, D. A. Keeley, and J. Y. Kwan, Astrophys. J. **179**, 111 (1973).
2. J. A. Garcia-Barreto, B. F. Burke, *et al.*, Astrophys. J. **326**, 954 (1988).
3. B. Hutawarakorn and R. J. Cohen, Mon. Not. R. Astron. Soc. **303**, 845 (1999).
4. H. J. Habing, W. M. Goss, H. E. Mattews, and A. Winnberg, Astron. Astrophys. **35**, 1 (1974).
5. A. D. Haschick, M. J. Reid, B. F. Burke, *et al.*, Astrophys. J. **244**, 76 (1981).
6. E. E. Baart, R. J. Cohen, R. D. Davies, *et al.*, Mon. Not. R. Astron. Soc. **219**, 145 (1986).
7. V. I. Slysh, I. E. Val'tts, and V. Migenes, Astron. Zh. **78**, 1073 (2001) [Astron. Rep. **45**, 942 (2001)].
8. M. Elitzur, Astrophys. J. **457**, 415 (1996).
9. A. H. Cook, Nature **211**, 503 (1996).
10. M. D. Gray and D. Field, Astron. Astrophys. **298**, 243 (1995).
11. A. W. Clegg, J. M. Cordes, J. K. Simonetti, and S. R. Kulkarni, Astrophys. J. **386**, 143 (1992).
12. V. I. Slysh, I. E. Val'tts, S. V. Kalenskiĭ, and G. M. Larionov, Astron. Zh. **76**, 751 (1999) [Astron. Rep. **43**, 657 (1999)].
13. M. Elitzur and T. de Jong, Astron. Astrophys. **67**, 323 (1978).
14. T. W. Hartquist and A. Sternberg, Mon. Not. R. Astron. Soc. **248**, 48 (1991).
15. J. M. Torrelles, J. F. Gomez, L. F. Rodriguez, *et al.*, Astrophys. J. **489**, 744 (1997).

Translated by G. Rudnitskiĭ

Astronomy Reports, Vol. 46, No. 3, 2002, pp. 224–232. Translated from Astronomicheskiĭ Zhurnal, Vol. 79, No. 3, 2002, pp. 249–258.

Intermediate-Brightness Equatorial Spectrophotometric Standards

V. M. Tereshchenko

Fesenkov Astrophysical Institute, Academy of Sciences of Kazakhstan, Kamenskoe Plato, Almaty, 480068 Kazakhstan

Received May 5, 2001

Abstract—We have obtained spectral energy distributions for 41 7^m–8^m stars near the celestial equator ($\delta = \pm 3°$). The $\lambda\lambda$3100–7600 Å spectral range is studied with a spectral resolution of 50 Å. The relative rms error in the visible is 1–2%, increasing to 3–5% towards the edges of the wavelength interval studied. All stars are referenced to a single standard, the circumpolar star HD 221525. The synthetic colors of common stars are compared with those observed in four photometric systems: UBV, $WBVR$, $uvby$, and that of the TYCHO catalog. The program stars are recommended as secondary spectrophotometric standards. © *2002 MAIK "Nauka/Interperiodica".*

1. INTRODUCTION

This is the last in a short series of papers concerned with the compilation of a uniform system of intermediate-brightness (7^m–9^m) regional spectrophotometric standards. In the first two papers [1, 2], we presented spectral energy distributions for stars in two zones of the celestial sphere: with declinations $\delta > 85°$ (circumpolar standards) and near 40° declination (intermediate-declination standards). Here, we present our spectral energy distributions for stars located in the equatorial zone, with declinations from $-3°$ to $+3°$. The value of equatorial standards is obvious. They can be used both in the northern and southern hemispheres, leading to better uniformity in observational results. This is especially important for catalogs and various surveys. It was not a coincidence that Oke [3] and Hayes [4] selected stars along the celestial equator for their spectrophotometric standards and that the $UBVRI$ standards established by Landolt [5] are especially popular among photometrists.

2. CHOICE OF STARS

Initially, we selected 44 stars as equatorial intermediate-brightness spectrophotometric standards. These are more or less uniformly distributed along the equator, with declinations from $-3°$ to $+3°$. Our photometric requirements for these stars were the usual ones: absence of variability, multiplicity, or peculiarities. Unfortunately, when we chose the candidate standards (late 1992), only sparse and crude data were available for most of the selected stars, and it later became clear that some did not satisfy the above requirements and had to be excluded from our final list of standards. In the end, 41 stars remained on this list. Like the intermediate-declination standards [2], these are 7^m–8^m stars of luminosity classes IV to V, belonging to spectral types either B8–A2 (early types) or G0–G5 (late types). As a rule, early- and late-type standards alternate in right ascension. Most users tend to prefer early-type stars as standards. Low-resolution spectra of such stars appear relatively smooth far from Balmer lines, making them well suited for instrumental calibration or the reduction of spectra of other objects. We included G stars in our list of standards for the following reasons. First, the integrated spectra of most galaxies are most similar to G-star spectra. Second, the spectra of G stars are smooth at 4400–9000 Å making them very suitable for standardization when using ordinary (not sensitized) CCD chips. It is also important that, in contrast to the spectra of early-type stars, their spectra show no strong flux gradient in this range. Finally, the resulting spectrophotometric data for the G stars can be used to search for photometric solar analogs.

The list of our program stars is presented in Table 1, together with their principal characteristics. These data are taken from the compiled sky catalog [9]. Note that the photometric data in [9] are very uncertain.

3. INSTRUMENTATION, PRIMARY STANDARD, AND OBSERVATION METHODS

All our observations were carried out in 1993–1994 at the former Tien Shan mountain observatory of the Sternberg Astronomical Institute ($h =$ 2800 m above the sea level). We used the 1-m Karl Zeiss (Jena) telescope ($D/F = 1/13$) with a single-channel, concave, diffraction grating, photoelectric

1063-7729/02/4603-0224$22.00

spectrometer. The general description of the spectrometer can be found in [10], and some of its operational features are discussed in [1]. Here, we present only basic information concerning the instrument and the observation method.

The spectrometer's design corresponds to the Seya–Namioka scheme, and the reciprocal dispersion in the studied wavelength range varies from 24–28 Å/mm. The spectra are scanned with uniform rotation of the grating and a scanning rate of 28 Å/s. The detector was a FEU-79 photomultiplier with analog recording. The width of the spectrometer exit slit was 0.8–1.1 mm and was not changed during a night. The spectral resolution was coarsened to the standard 50 Å when measuring the recorded spectra, by dividing them into intervals for averaging. When observing early-type stars, including the standard, the readings at red wavelengths were artificially increased by switching to a different amplification regime. The change in the amplifier sensitivity occurred near 6000 Å, simultaneous with the insertion or removal of a dividing filter. The overall sensitivity of the receiving and recording path was checked using an artificial light source.

As in [1, 2], all the equatorial standards were referenced to a single standard, the circumpolar star HD 221525 ($V = 5.58$; F0IV). Its spectral energy distribution was derived by us earlier [11]. Note that our energy distribution for HD 221525 is expressed on the energy scale defined by Vega in accordance with the work of Hayes [12], and the star itself was used as one of the primary standards when creating the photometric $WBVR$ catalog [13]. HD 221525 was found to be among the best primary spectrophotometric standards in the study [14].

We used a differential observation technique—the method of equal altitudes. When reducing the data to extraatmospheric values, we used the mean transparency for the Earth's atmosphere. Note that the atmospheric transparency at Tien Shan deteriorated during our observations due to the eruption of Pinatubo (the Philippines) in Summer 1991. The specialized measurements of [15] indicate that the transparency coefficient at the Tien Shan Observatory worsened by 10–12% during that period.

For three years, from 1991 to 1994, a large aureola (several tens of degrees in size) remained visible around the Sun independent of season or weather, testifying to the presence of a large amount of dust in the stratosphere. This may also be responsible for the abnormally low number of clear nights in those years. In our reduction, we used the transparency coefficient derived in [15]. Each star was observed from four to six times on different nights, with a single observation usually consisting of four (less often, two) scans in

Table 1. Equatorial standards and their main characteristics

No.	HD	α_{2000}	δ_{2000}	V	$B-V$	Sp
1	2830	$00^h31^m.7$	$-01°48'$	$7^m.03$	$0^m.08$	A0
2	3628	00 39.2	03 08	7. 32	0. 63	G2V
3	9716	01 35.1	−02 20	7. 5	0. 1	A0V
4	13043	02 07.6	−00 37	6. 91	0. 61	G2V
5	17808	02 51.4	−03 00	8. 0	0. 1	A0V
6	20619	03 19.0	−02 51	7. 04	0. 65	dG2
7	23009	03 41.6	−00 10	7. 8	0. 1	A0V
8	27063	04 16.5	−00 34	7. 8	0. 7	G0V
9	29788	04 41.6	00 34	8. 0	0. 0	B9.5V
10	36117	05 29.5	−00 03	7. 97	0.10	A0
11	39833	05 55.0	−00 30	7. 8	0. 7	G0V
12	46090	06 31.4	02 55	7. 70	0. 7	G0V
13	47221	06 37.7	01 49	7. 9	0. 0	B9.5V
14	59688	07 31.2	02 10	7. 5	0. 7	G0V
15	71431	08 27.5	00 50	7. 8	0. 7	G0V
16	75620	08 51.1	00 28	8. 01	0. 08	A0V
17	80916	09 22.5	−01 05	8. 00	0. 1	A0V
18	83290	09 37.4	01 53	7. 9	0. 7	G0V
19	88725	10 14.1	03 09	7. 76	0. 60	G1V
20	90212	10 24.8	−00 47	7. 9	0. 1	A0V
21	100237	11 32.0	−01 47	7. 6	0. 1	A0V
22	102844	11 50.4	−02 25	7. 90	0. 7	G0V
23	108228	12 26.0	02 03	7. 6	0. 1	A0V
24	109098	12 32.1	−01 46	7. 6	0. 7	G0V
25	121513	13 55.8	01 31	8. 0	0. 1	A0V
26	126053	14 23.3	01 14	6. 27	0. 63	G1V
27	133409	15 04.4	−00 54	8. 0	0. 1	A0V
28	138369	15 31.7	00 53	7. 7	0. 6	G0V
29	147470	16 22.9	00 30	7. 7	0. 1	A0V
30	152391	16 53.0	−00 02	6. 64	0. 76	G6V
31	158509	17 29.6	01 33	7. 9	0. 0	B9.5V
32	169225	18 23.8	−01 09	7. 5	0. 0	B9.5V
33	172233	18 39.2	00 06	8. 04	0. 61	G0
34	185198	19 37.9	01 30	7. 5	0. 0	B9.5V
35	186104	19 42.5	01 35	7. 7	0. 6	G0V
36	193559	20 20.7	01 23	8. 0	0. 0	B9.5V
37	194764	20 27.4	−01 34	7. 1	0. 7	G0V
38	203993	21 25.5	02 03	7. 53	0. 01	A0
39	212837	22 27.1	−01 19	6. 8	0. 6	G0
40	216261	22 51.6	−01 49	7. 90	0. 1	A0V
41	219018	23 12.6	02 41	7. 72	0. 63	G5

Table 2. Spectral energy distributions of the equatorial standards (in 10^{-6} erg cm^{-2} s^{-1} cm^{-1})

$\overline{\lambda}$, Å	Standard No. (from Table 1)									
	1	2	3	4	5	6	7	8	9	10
3175	477	188	294	261	283	238	164	91	252	201
3325	478	240	296	357	271	315	156	109	247	194
3475	466	241	293	357	261	316	157	104	242	187
3625	471	260	296	384	252	333	159	119	246	181
3775	552	268	381	410	322	333	207	116	301	227
4025	1283	439	819	690	657	538	459	197	621	486
4225	1166	435	764	690	579	523	404	197	588	437
4425	1022	463	674	733	498	579	360	216	546	390
4625	936	501	636	788	446	623	329	238	504	352
4775	822	489	564	770	394	616	294	234	470	314
5025	735	465	510	714	348	574	262	217	417	282
5175	673	435	479	677	325	546	243	206	386	259
5375	611	462	437	715	290	563	217	218	362	241
5575	562	462	407	703	269	579	205	223	339	222
5775	510	445	375	685	242	564	191	215	320	201
6025	464	430	344	655	219	555	175	212	292	183
6225	416	407	310	624	200	526	160	200	267	168
6425	373	392	281	597	179	507	143	190	242	152
6675	329	370	254	568	162	482	131	185	220	140
6925	299	357	231	539	147	456	121	172	206	126
7175	264	333	207	511	137	440	107	171	186	115
7375	238	321	195	473	127	422	101	160	178	113
7575	218	298	188	436	113	386	90	154	169	102
λ, Å	11	12	13	14	15	16	17	18	19	20
3175	132	171	550	178	168	200	101	84	165	240
3325	167	235	510	223	190	195	97	95	177	227
3475	155	221	479	213	193	197	99	88	189	217
3625	173	245	444	240	205	189	102	98	197	218
3775	180	266	475	249	226	226	120	96	199	279
4025	304	433	663	406	341	496	252	160	295	594
4225	295	421	567	397	339	445	237	158	281	526
4425	317	471	484	422	359	396	211	168	304	466
4625	345	530	424	458	380	368	200	181	323	423
4775	344	509	375	445	366	331	178	177	306	373
5025	312	480	331	419	345	287	160	167	298	333

Table 2. (Contd.)

λ, Å	11	12	13	14	15	16	17	18	19	20
5175	296	445	302	397	339	267	149	159	283	305
5375	317	482	271	422	344	241	134	164	297	279
5575	318	488	245	414	347	226	131	166	295	260
5775	314	493	220	410	331	203	118	162	287	239
6025	300	489	197	395	316	187	110	158	276	214
6225	287	456	177	373	302	170	103	152	265	191
6425	278	440	157	355	294	153	94	136	251	171
6675	265	439	140	346	274	138	85	137	245	157
6925	255	411	135	327	266	128	75	132	229	134
7175	236	393	116	310	255	121	73	125	217	127
7375	225	394	106	298	240	116	69	115	212	115
7575	209	375	93	280	235	109	59	108	190	100
λ, Å	21	22	23	24	25	26	27	28	29	30
3175	440	113	389	188	181	510	141	186	250	244
3325	409	145	363	226	176	698	146	216	245	339
3475	397	138	358	221	173	696	141	207	239	324
3625	388	149	343	251	171	747	146	215	244	359
3775	512	159	448	259	222	792	180	239	334	368
4025	030	255	980	431	501	1213	375	390	682	655
4225	892	253	882	418	453	1192	350	388	609	651
4425	775	263	762	458	397	1273	322	422	541	772
4625	691	286	681	490	362	1347	304	456	485	879
4775	613	278	608	485	328	1327	274	441	426	881
5025	525	262	540	450	285	1239	251	402	388	820
5175	491	253	501	429	271	1137	231	381	360	741
5375	436	264	451	466	247	1216	215	414	324	842
5575	395	266	417	454	228	1182	203	410	301	846
5775	350	264	369	436	207	1164	191	401	270	845
6025	304	250	333	440	190	1120	173	392	246	820
6225	273	242	306	405	176	1068	160	361	224	784
6425	238	230	283	390	157	1032	149	356	201	759
6675	215	225	248	373	146	1021	135	338	184	730
6925	190	219	217	343	135	967	125	316	165	695
7175	167	209	199	335	125	933	114	305	147	656
7375	143	203	186	325	119	945	109	294	139	643
7575	124	198	167	320	111	847	99	280	128	620

Table 2. (Contd.)

λ, Å	31	32	33	34	35	36	37	38	39	40	41
3175	271	236	115	632	133	239	173	393	265	154	140
3325	255	230	138	591	175	232	237	396	361	159	174
3475	244	231	129	559	160	225	234	391	364	155	167
3625	229	235	144	536	181	217	265	375	408	151	182
3775	264	331	150	575	184	250	294	459	443	193	189
4025	432	637	243	771	312	465	494	868	728	424	315
4225	394	575	248	710	308	413	502	767	742	390	313
4425	342	515	258	632	343	360	543	683	780	346	329
4625	310	466	271	592	366	326	596	634	838	325	360
4775	283	425	264	543	361	290	583	568	826	288	360
5025	250	392	246	520	330	257	542	483	776	265	333
5175	232	363	225	493	311	235	519	435	742	242	310
5375	217	339	244	472	335	214	553	395	785	223	335
5575	201	320	237	449	335	196	559	367	764	211	330
5775	190	294	237	421	333	179	535	343	756	195	316
6025	168	255	220	375	320	160	524	313	730	176	302
6225	152	235	206	352	302	146	487	283	692	158	283
6425	141	215	198	322	289	130	467	256	666	143	275
6675	125	196	188	293	272	119	450	239	648	133	261
6925	115	180	175	273	261	110	435	210	604	124	252
7175	111	168	170	249	250	100	417	190	580	115	245
7375	93	150	163	233	237	95	391	172	545	108	237
7575	87	141	148	210	225	88	370	152	507	98	228

different directions. The standard was observed in the north, while the program stars were observed in the south, near the meridian, leading to the danger of instrumental and atmospheric azimuthal effects. Instrumental effects were removed using an artificial light source. The situation is not so simple for transparency. Although no difference in transparency between the northern and southern directions was apparent visually, this does not exclude the possibility of such differences. Extensive specialized observations would be required to detect and quantify possible differences of the atmospheric transparency toward the celestial pole; we have not performed such observations. We expected the danger of an azimuthal effect to be low for observations at zenith distances not exceeding 45°–48°. Of course, this can be considered a weak point in our technique. We took into account the sky background only for nights near the full Moon; it was negligible for program stars on all other nights. The entire program has taken thirty full or partial nights.

In our numerical reduction, we used well-known formulas for differential observations. However, in contrast to the observations for the catalog [10], we applied readings corresponding to the integrated spectrum rather than the integrated envelope curve for the primary standard. This was necessitated by the spectral energy distribution of HD 221525, which is not suitable for plotting a trustworthy envelope curve.

After the numerical computer reduction, we derived large-scale $E(\lambda)$ plots for each star. These were used to apply final corrections to $E(\lambda)$ at some points. From five to ten such corrections were made for the entire spectrum (90 points). Usually, corrections were needed for points at the very edges of the studied wavelength range and also near 6000 Å where the filter was introduced and the amplification regime changed. Note that we did not apply strong smoothing, as can be seen from the data presented. Our final results—the extra-atmospheric monochromatic illuminations from the equatorial standards—are presented in Table 2. The first line gives the star numbers from Table 1 and the first column the central wavelengths of the averaged intervals (in Angstroms). As in [1, 2], the data on the energy distribution was obtained in a "continuous" form. However, because of their large volume, they are presented in Table 2 in a discrete form, for 23 of the 90 spectral points studied. The data will be completely presented in electronic form at the Astronomical Data Center.

4. INTERNAL ACCURACY AND AGREEMENT WITH BROAD-BAND PHOTOMETRY

A traditional measure of accuracy is the relative rms error, though, strictly speaking, it reflects internal consistency rather than overall accuracy. The relative rms error of our data in the visible is 1–2%, rising to 3–5% near the edges of the wavelength interval studied. Despite the fact that the fluxes of the secondary standards are one to two orders of magnitude lower than those of stars of the catalog [10], the internal consistency shown by the secondary standards is better by a factor of 1.5–2. This increased accuracy is due to the larger aperture of the telescope, better guiding, better and more stable transparency (compared to Kamenskoe Plateau), the use of a single standard, and the larger number of observations. The origin of the scatter in our final results is mainly instrumental. As expected in this case, the errors increase with increasing ambient temperature and decreasing stellar brightness and are virtually independent of the air mass difference between the program star and standard.

It is impossible to directly determine the external agreement for the program stars, since no similar data obtained by other authors are available. However, there is an indirect method that can be applied to check our results, which we have used from the very beginning of our large-scale spectrophotometric observations [16]. We are referring to comparisons between color indices computed from energy distributions (sometimes called "synthetic" color indices) and those directly observed. Such comparisons are possible for the vast majority of stars for which spectrophotometric measurements are available, since the total number of stars with photometric data is higher by a factor of a hundred. Note that this same approach is used by theorists for model-atmosphere comparisons (see, for instance, [17]). Obviously, this comparison will be more significant if we use a larger number of photometric systems and increase the number of observations in one of these. Experience shows that candidate standard stars should be observed many times, by different observers using different instrumentation at different sites. Otherwise, there exists the danger of obtaining "standard" data with hidden systematic and random errors; it also cannot be ruled out that a standard star proves to be variable.

We included the four most reliable and widely used photometric systems in our comparison: the Johnson UBV, Sternberg Astronomical Institute $WBVR$, and Strömgren $ubvy$ systems, as well as the system of the TYCHO catalog. By definition,

$$m_i - m_j = -2.5\log[\Sigma E(\lambda)\varphi_i(\lambda)\Delta\lambda/\Sigma E(\lambda)\varphi_j(\lambda)\Delta\lambda] + C_{ij},$$

where m_i and m_j are the i and j magnitudes, $E(\lambda)$ is the spectral energy distribution of the star, $\varphi_i(\lambda)$ and $\varphi_j(\lambda)$ are the response curves for the i and j bands, and C_{ij} is a constant that depends on the zero point of the magnitude scale and the choice of measurement units.

Table 3. δV, $\delta(U-B)$, and $\delta(B-V)$ deviations for the UBV system

No.	HD	$V_{\rm obs}$	δV	$\delta(U-B)$	$\delta(B-V)$
1	2830	7.03	0.04	–	0.01
2	3628	7.32	0.05	–	0.01
3	13043	6.91	0.10	0.05	0.01
4	20619	7.04	0.02	0.03	0.01
5	36117	7.97	−0.04	−0.02	0.01
6	75620	8.01	0.02	0.03	0.00
7	88725	7.76	0.01	0.05	0.00
8	126053	6.27	0.04	0.09	0.05
9	152391	6.64	0.02	0.04	0.02
10	172233	8.04	0.06	0.09	0.04
11	219018	7.72	0.08	–	0.02
Mean			0.036	0.045	0.016

Table 4. δV, $\delta(W-B)$, and $\delta(B-V)$ deviations for the $WBVR$ system

No.	HD	$V_{\rm obs}$	δV	$\delta(W-B)$	$\delta(B-V)$
1	2830	7.058	0.067	−0.014	−0.010
2	13043	6.883	0.074	−0.035	0.005
3	20619	7.025	0.028	0.012	−0.018
4	126053	6.266	0.039	−0.004	0.033
5	152391	6.625	0.010	−0.032	0.006
6	194764	7.117	0.040	−0.018	0.001
7	212837	6.781	0.075	−0.021	0.005
Mean			0.048	−0.016	0.003

Thus, the computed color indices depend on the spectral energy distribution, the system response curves, and the constants C_{ij}. Naturally, the computation of synthetic colors requires continuous data on the energy distribution in the integrated spectrum, in the form of an uninterrupted histogram, which are not always available. We adopted the response curves for the photometric systems from [13, 18–20].

Although the technique used for computing color indices has been described numerous times in the literature (for example, cf. [21]), we wish to discuss our determination of the constants in somewhat more detail. Two approaches are found in the literature: the first is based on the use of data for a single star, and the second on the use of data for many stars. The first method is less resource-intensive and more transparent, but requires very accurate photometric and spectrophotometric data for the chosen star. Obviously, any random error in the data becomes a source of systematic errors in this case. Most often, the main primary spectrophotometric standard Vega is used to determine the constants; this was done, for example, in [14, 18]. Kharitonov *et al.* [22] preferred the second method, since they felt this made it possible to avoid systematic errors. We do not agree with this point of view. Although the agreement between the spectrophotometric and photometric data may be better in this case, the results of the comparison will not necessarily be more reliable: the second approach implicitly assumes the absence of systematic errors in the spectrophotometric data, which is not always the case. Moreover, the main goal of the photometric comparison is precisely to reveal systematic errors or demonstrate their absence. Note that, in the first method, we actually determine to what extent the spectrophotometric data are homogeneous with respect to the primary standard. In the process, it is assumed that the scale of the photometric system is linear, as is the case for most well-known systems. For these reasons, we decided to use the first approach. Because the primary standard for all our program stars was HD 221525, it was natural to use this star when determining the constants as well, also having in mind the lack of data for Vega in the TYCHO catalog. We determined the constants for the TYCHO and *uvby* systems using HD 221525, and for the UBV and $WBVR$ systems using Vega. In this procedure, we assume that the computed and directly observed color indices should be equal for the chosen star. Remember that $E(\lambda)$ for HD 221525 was derived for the Vega system, in accordance with the work of Hayes [12].

Proceeding as described above, we computed color indices for all the intermediate-brightness standards in three broad-band (UBV, $WBVR$, and TYCHO) photometric systems and one intermediate-band (the Strömgren) system. We then calculated deviations for common stars, i.e., differences in the directly observed color indices and those computed from the energy distributions. The photometric data for the Strömgren system were taken from the electronic version of the catalog [23]. It is known that, instead of ordinary color indices, the *uvby* system uses combinations of color indices, also called indices. To make the comparison data more uniform, we transformed these indices into color indices. The TYCHO catalog contains B_T and V_T magnitudes; we formed the $B_T - V_T$ color indices via simple subtraction. Note that this is the first time the

TYCHO catalog has been used for comparison with spectrophotometric data.

The deviations in the various systems are presented in Tables 3–6. These tables show that the deviations for most stars are within one or two hundredths of a magnitude, which is quite satisfactory, even for standards. However, several cases of relatively large deviations are present.

For 11 of the 41 stars on our list, there exist UBV photoelectric data (the catalog of Nicolet [24]), and $WBVR$ data are available for seven [13]. The corresponding color differences (deviations) are collected in Tables 3 and 4. We computed the V magnitudes in accordance with the $WBVR$ response curves. Note that they coincide with the analogous UBV magnitudes to within 0.01^m, and we did not recompute them for the latter system. We conclude that the agreement of the $WBVR$ color indices is excellent ($\delta(W-B) = -0.016$ and $\delta(B-V) = 0.003$), being somewhat worse for the UBV indices ($\delta(U-B) = 0.045$ and $\delta(B-V) = 0.016$). This discrepancy between the mean deviations found for the two similar systems is surprising, especially since five of the seven stars in Table 3 are also in Table 4. For example, the deviations in the ultraviolet for the Johnson UBV system indicate that the spectrophotometric measurements in this range are too high (too blue), whereas the deviations in the $WBVR$ system indicate them to be too low. This discrepancy is difficult to explain for two such similar systems. The same is true of the relatively high deviation for the V magnitudes. Elucidation of the origin of these discrepancies requires additional observations, including spectrophotometry.

In the TYCHO catalog system, five stars of the 41 show $\delta(B_T - V_T)$ deviations within 0.030–0.045, while the values for the remaining stars are below 0.030, within the combined photometric and spectrophotometric errors. Unfortunately, a systematic deviation of up to 0.01 is present whose origin remains unclear. Note that some stars show discrepant results for different comparisons of photometric systems. In these cases, the deviations in one of the systems must clearly be due to photometric errors for that system. Several stars demonstrate discrepancies between the computed color index and the mean value for the corresponding spectral type. This is especially true of the G5IV stars. This is probably due to errors in their spectral classification.

The results of our comparison with photometric data in the intermediate-band $uvby$ system are presented in Table 6. In general, the deviations are within the expected range, but the $\delta(u-v)$ values for three of the 26 stars in common (marked with "!") are high. However, the most surprising thing is that the sum of the deviations is the lowest for $v-b$; the next lowest sum is for $u-v$ (even including the three discrepant points), and the sum is highest for $b-y$. In addition, as for our comparison with the TYCHO catalog, this last color index demonstrates a systematic offset. On average, the computed color indices are 0.015 bluer than the directly observed values. Our analysis again confirms that, if we wish to identify reliable standards

Table 5. $\delta(B_T - V_T)$ deviations for the TYCHO catalog system

No.	HD	$B_T - V_T$	$\delta(B_T - V_T)$
1	2830	−0.088	−0.027
2	3628	0.693	−0.012
3	9716	0.189	−0.003
4	13043	0.700	0.011
5	17808	0.027	−0.019
6	20619	0.721	−0.007
7	23009	0.118	−0.018
8	27063	0.749	0.013
9	29788	0.214	−0.035
10	36117	0.115	−0.025
11	39833	0.687	−0.029
12	46090	0.782	0.008
13	47221	−0.137	−0.045
14	59688	0.705	0.007
15	71431	0.659	−0.007
16	75620	0.123	−0.012
17	80916	0.152	−0.027
18	83290	0.707	0.001
19	88725	0.694	0.025
20	90212	0.079	−0.014
21	100237	−0.002	0.009
22	102844	0.701	0.002
23	108228	0.059	−0.022
24	109098	0.712	−0.003
25	121513	0.141	0.001
26	126053	0.708	0.043
27	133409	0.229	−0.020
28	138369	0.686	−0.010
29	147470	0.100	0.022
30	152391	0.856	−0.030
31	158509	0.060	−0.020
32	185198	0.191	−0.020
33	186104	0.726	−0.009
34	193559	0.042	0.001
35	194764	0.746	−0.007
36	203993	0.035	−0.023
37	212837	0.697	−0.011
38	216261	0.165	−0.028
39	219018	0.693	−0.034
Mean			−0.0096

Table 6. Deviations in the Strömgren *uvby* system

No.	HD	$\delta(u-v)$	$\delta(v-b)$	$\delta(b-y)$
1	2830	−0.020	+0.002	−0.013
2	3628	−0.021	−0.008	−0.018
3	13043	−0.028	−0.008	−0.011
4	20619	+0.012	−0.007	−0.022
5	23009	−0.007	+0.001	−0.011
6	27063	−0.015	−0.016	−0.013
7	36117	+0.025	−0.006	−0.010
8	39833	+0.015	−0.002	−0.033
9	46090	+0.022	−0.004	−0.009
10	59688	+0.040	0.000	−0.022
11	71431	+0.078!	0.000	−0.026
12	80916	−0.030	+0.007	−0.013
13	83290	+0.086!	−0.011	−0.026
14	88725	+0.025	−0.029	−0.027
15	90212	+0.023	−0.003	−0.028
16	100237	+0.020	+0.001	+0.001
17	102844	+0.067!	−0.011	−0.028
18	109098	−0.003	−0.014	−0.037
19	126053	−0.007	+0.015	+0.014
20	133409	+0.019	−0.015	−0.013
21	138369	+0.017	+0.002	−0.016
22	152391	−0.003	−0.012	−0.019
23	169225	+0.016	−0.010	−0.024
24	172233	+0.017	−0.001	+0.004
25	186104	+0.019	+0.005	−0.012
26	194764	−0.016	−0.015	−0.015
Mean		+0.0042*	−0.0054	−0.0159

Note: * Without the three values marked with "!."

of any kind, we must observe candidate stars many times. However, it also follows that the vast majority of our data on the spectral energy distributions of the program stars can be used for standardization. Tables 3–6 demonstrate that virtually all of these data are accurate and trustworthy.

ACKNOWLEDGMENTS

This study was supported by the European Southern Observatory (grant B-06-007 for 1995). Staff members of the Sternberg Astronomical Institute's Almaty Laboratory, especially A.V. Mironov, provided important assistance during the observations. I am also grateful to T. Bobryashova, L. Knyazeva, O. Kolykhalova, and N. Morozova for their help during the data reduction and to the referee for helpful remarks.

REFERENCES

1. V. M. Tereshchenko, Astron. Zh. **71**, 468 (1994) [Astron. Rep. **38**, 410 (1994)].
2. V. M. Tereshchenko, Astron. Zh. **78** (2001).
3. J. B. Oke, Astrophys. J. **140**, 689 (1964).
4. D. S. Hayes, Astrophys. J. **159**, 165 (1970).
5. A. U. Landolt, Astron. J. **88**, 439 (1983).
6. V. V. Biryukov, G. V. Borisov, and I. N. Glushneva, Astron. Astrophys. Trans. **16**, 83 (1998).
7. G. V. Borisov, I. N. Glushneva, and V. I. Shenavrin, Astron. Astrophys. Trans. **17**, 309 (1999).
8. J. B. Oke, Astron. J. **99**, 1621 (1990).
9. A. Hirshfeld and R. W. Sinnot, *Sky Catalogue 2000.0* (Cambridge Univ. Press, Cambridge, 1982), Vol. 1.
10. A. V. Kharitonov, V. M. Tereshchenko, and L. N. Knyazeva, *Spectrophotometric Catalogue of Stars* [in Russian] (Nauka, Alma-Ata, 1988).
11. V. M. Tereshchenko and E. A. Glushkova, Astron. Zh. **69**, 436 (1992) [Sov. Astron. **36**, 218 (1992)].
12. D. S. Hayes, in *Calibration of Fundamental Stellar Quantities (IAU Symposium 111),* Ed. by D. S. Hayes, *et al.* (D. Reidel, Dordrecht, 1985).
13. V. G. Kornilov, I. M. Volkov, A. I. Zakharov, *et al.*, *Catalog of WBVR Quantities of Bright Northern Stars* [in Russian] (Mosk. Gos. Univ., Moscow, 1991).
14. A. V. Mironov and V. G. Moshkalev, Astron. Zh. **72**, 80 (1995) [Astron. Rep. **39**, 70 (1995)].
15. V. M. Tereshchenko, Astron. Tsirk. **1556**, 41 (1994).
16. V. M. Tereshchenko and A. V. Kharitonov, *Zonal Spectrophotometric Standards* [in Russian] (Nauka, Alma-Ata, 1972).
17. R. I. Kurucz, in *Precision Photometry: Astrophysics of the Galaxy,* Ed. by A. G. D. Philip, A. R. Upgren, and K. A. Janes (L. Davis Press, Schenectady, 1991), p. 27.
18. A. Azusienis and V. Straizys, Astron. Zh. **46**, 402 (1969) [Sov. Astron. **13**, 316 (1969)].
19. S. Matsushima, Astrophys. J. **158**, 1137 (1969).
20. M. A. C. Perryman, E. Hog, J. Kovalevsky, L. Lindegren, and C. Turon, *The Hipparcos and Tycho Catalogues,* ESA SP-1200 (1997).
21. V. Straizys, *Multicolor Stellar Photometry* (Mokslas, Vil'nyus, 1977; Pachart Publ. House, Tucson, 1992).
22. A. V. Kharitonov, I. N. Glushneva, and L. N. Knyazeva, Astron. Zh. **71**, 657 (1994) [Astron. Rep. **38**, 583 (1994)].
23. B. Hack and M. Mermilliod, Astron. Astrophys., Suppl. Ser. **86**, 107 (1990).
24. B. Nicolet, Astron. Astrophys., Suppl. Ser. **34**, 1 (1978).

Translated by N. Samus'

Astronomy Reports, Vol. 46, No. 3, 2002, pp. 233–245. Translated from Astronomicheskiĭ Zhurnal, Vol. 79, No. 3, 2002, pp. 259–271.

Studies of Intermediate-Mass Stellar Models Using Eclipsing Binaries

D. A. Kovaleva

Institute of Astronomy, Pyatnitskaya ul. 48, Moscow, Russia

Received May 5, 2001

Abstract—Evolutionary computations for intermediate-mass stars are analyzed using observed parameters for eclipsing SB2 binaries and theoretical parameters based on evolutionary tracks. Modern observations cannot be used to distinguish between models with and without convective overshooting for stars in the vicinity of the main sequence. Statistically significant discrepancies between the observed and computed stellar parameters are associated with systematic errors in photometric effective temperatures. After taking into account systematic effects, the theoretical computations fit the observational data uniformly well throughout the entire mass interval studied. Empirical and semiempirical (i.e., reduced to the ZAMS and with solar elemental abundances) formulas for the mass–luminosity, mass–effective temperature, and mass–radius relations are proposed. © *2002 MAIK "Nauka/Interperiodica"*.

1. INTRODUCTION

One fundamental problem in which the mass–luminosity relation (MLR) plays an important role is the determination of the form of the initial mass function (IMF) dN/dm. The general form of the IMF is often described by a power-law dependence $dN/dm = m^{\gamma}$, where $\gamma = -2.35$ for a Salpeter IMF.

It is virtually impossible to derive the initial mass function from direct star counts within a magnitude interval $m, m + dm$. The principal technique used to determine the IMFs of field stars is to obtain the distribution of the stars in some well-known observational parameter (in most cases, the magnitude) and then transform this into a stellar-mass distribution using the appropriate MLR and evolutionary corrections [1].

The most important quantity for precise determination of the IMF is not the MLR itself but its derivative. If we are interested in the IMF, the accuracy of the usual power-law approximations of empirical MLRs becomes insufficient. In addition, we must assume that the available observational data are uniform in evolutionary status and chemical composition, which is certainly not true for the field stars on which empirical MLRs are usually based. The true behavior of MLRs can only be understood using accurate stellar models.

Empirical MLRs based on a limited number of relatively reliable determinations of the masses and luminosities of components of spectral binaries with observed eclipses and of visual binaries provide a powerful tool for estimating the masses of main-sequence (MS) stars with known magnitudes and distances [2–5].

However, as noted in [6], we have already reached a fundamental limit in the accuracy of such MLRs for some classes of objects, and it is impossible to obtain more detailed information about the form of the corresponding relations by averaging a larger number of more accurate data [3].

However, it is not desirable to base analyses of MLRs solely on theoretical models. The results of theoretical computations can be subject to biases due to the adopted assumptions or simplifications. Therefore, the characteristic features of a theoretical MLR can differ from its real features; combined with the existence of nonmonotonic portions of the luminosity function, this can lead to erroneous conclusions about the IMF. The aim of the current study is to determine if there are systematic discrepancies between modern stellar models and observational data and, if there are, identify the origins of these discrepancies using observations of eclipsing binaries. This will enable us to draw conclusions concerning the overall adequacy of various modern models and differences between them on the basis of high-precision data, which are seldom [8] used to address such problems.

Section 2 describes the observational and computational results used in this work. In Section 3, we present our formulation of the problem and the method we have used to attack it. Section 4 analyzes the results obtained. Section 5 presents empirical and semiempirical mass–luminosity, mass-effective temperature, and mass–radius relations. We summarize our conclusions in Section 6.

2. SEMIEMPIRICAL LUMINOSITIES, TEMPERATURES, AND RADII

In [6], we obtained uniform estimates of the ages and metallicities of 43 double-line eclipsing binaries

1063-7729/02/4603-0233$22.00

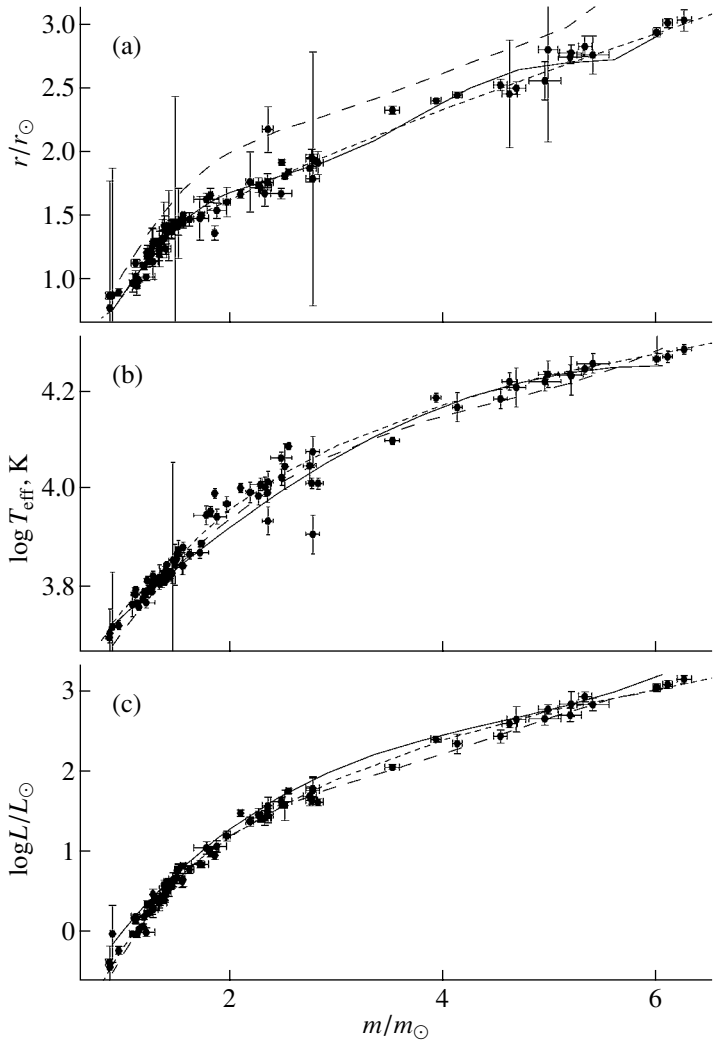

Fig. 1. Distribution of the components of the 43 eclipsing binaries studied on the following diagrams (corrected for evolutionary effects and differences in chemical composition): (a) mass–radius; (b) mass–effective temperature, and (c) mass–bolometric luminosity. Shown for comparison are theoretical ZAMS relations corresponding to the Geneva models for solar metallicity, $Z = 0.02$ (short dashed curves), the empirical relations (long dashed curves), and the semiempirical relations (solid curves).

using two independent grids of evolutionary tracks (computed by the Geneva and Padova groups). We tested the results for stability and estimated their accuracy based on the errors for the observational data (the masses and radii of components). The ages and metallicities estimated using the two grids of evolutionary tracks were in good agreement, within the quoted errors. We also found a reasonable agreement with the data obtained in [8] and with independent estimates of the metallicities and ages based on photoelectric measurements and membership of the binaries in clusters with known parameters.

The observational parameters of the stars studied are listed in Tables 2 and 3 of [6]. We can easily compute how these data (for example, the radii) would change if, other conditions being equal, all the observed stars had the same (for example, solar) chemical composition and were at the same evolutionary stage [for example, on the zero-age main sequence (ZAMS)]:

$$R^{\text{semi-obs}}(m^{\text{obs}}, a_{\text{ZAMS}}, Z_\odot) = R^{\text{obs}} + [(R(m^{\text{obs}}, a_{\text{ZAMS}}, Z_\odot) - R(m^{\text{obs}}, a, Z)]), \quad (1)$$

where R^{obs} is the observational radius; $R(m^{\text{obs}}, a, z)$ is the radius derived from tracks for the observed mass and the computed age and chemical composition; and $R(m^{\text{obs}}, a_{\text{ZAMS}}, Z_\odot)$ is the radius computed for the observed mass, age, and solar chemical composition. The semiempirical radii $R^{\text{semi-obs}}(m^{\text{obs}}, a_{\text{ZAMS}}, Z_\odot)$ (and the corresponding effective temperatures and luminosities) computed in this way are listed in Table 1 (for the Geneva models). We computed the errors of

Table 1. Observational masses (see Tables 1, 2 in [6]), as well as the radii, effective temperatures, and luminosities of components reduced to the ZAMS for solar chemical composition

Name/HD No.	$m(\mathrm{A})/m_\odot$ $m(\mathrm{B})/m_\odot$	$r(\mathrm{A})/m_\odot$ $r(\mathrm{B})/m_\odot$	$\log T_{\mathrm{eff}}(\mathrm{A})$, K $\log T_{\mathrm{eff}}(\mathrm{B})$, K	$\log L_{\mathrm{bol}}(\mathrm{A})/L_\odot$ $\log L_{\mathrm{bol}}(\mathrm{B})/L_\odot$
GG Lup	4.129 ± 0.044	2.292 ± 0.024	4.168 ± 0.030	2.34 ± 0.12
HD 135 876	2.515 ± 0.024	1.659 ± 0.019	4.045 ± 0.047	1.57 ± 0.19
ζ Phe	3.930 ± 0.045	2.237 ± 0.017	4.187 ± 0.010	2.39 ± 0.04
HD 6882	2.551 ± 0.026	1.679 ± 0.023	4.087 ± 0.007	1.75 ± 0.03
IQ Per	3.53 ± 0.06	2.243 ± 0.031	4.099 ± 0.007	2.05 ± 0.03
HD 24 909	1.72 ± 0.04	1.439 ± 0.020	3.888 ± 0.006	0.82 ± 0.03
PV Cas	2.81 ± 0.05	2.038 ± 0.091	4.011 ± 0.011	1.61 ± 0.04
HD 240 208	2.76 ± 0.06	2.079 ± 0.068	4.011 ± 0.010	1.63 ± 0.04
V451 Oph	2.776 ± 0.063	1.835 ± 0.038	4.076 ± 0.032	1.78 ± 0.13
HD 170 470	2.356 ± 0.052	1.656 ± 0.030	4.014 ± 0.022	1.44 ± 0.09
RX Her	2.75 ± 0.06	1.867 ± 0.107	4.047 ± 0.030	1.68 ± 0.12
HD 170 757	2.33 ± 0.05	1.669 ± 0.100	4.004 ± 0.020	1.41 ± 0.09
TZ Men	2.487 ± 0.025	1.904 ± 0.020	4.023 ± 0.017	1.60 ± 0.07
HD 39 780	1.504 ± 0.010	1.401 ± 0.015	3.856 ± 0.018	0.66 ± 0.07
AR Aur	2.480 ± 0.098	1.604 ± 0.041	4.063 ± 0.012	1.61 ± 0.05
HD 34 364	2.294 ± 0.093	1.649 ± 0.040	4.008 ± 0.013	1.41 ± 0.05
V1031 Ori	2.473 ± 0.018	1.837 ± 4.359	3.906 ± 0.039	1.76 ± 0.17
HD 38 735	2.286 ± 0.016	2.234 ± 0.179	3.934 ± 0.027	1.56 ± 0.11
β Aur	2.355 ± 0.028	1.924 ± 0.062	3.991 ± 0.019	1.49 ± 0.08
HD 40 183	2.271 ± 0.025	1.893 ± 0.056	3.985 ± 0.019	1.45 ± 0.08
V1647 Sgr	2.189 ± 0.037	1.669 ± 0.238	3.992 ± 0.020	1.37 ± 0.05
HD 163 708	1.972 ± 0.033	1.522 ± 0.116	3.968 ± 0.016	1.19 ± 0.06
VV Pyx	2.101 ± 0.022	1.801 ± 0.035	4.001 ± 0.009	1.47 ± 0.04
HD 71 581	2.099 ± 0.019	1.802 ± 0.035	4.001 ± 0.009	1.47 ± 0.04
CM Lac	1.88 ± 0.09	1.476 ± 0.060	3.942 ± 0.015	1.06 ± 0.07
HD 209 147	1.47 ± 0.04	1.366 ± 0.061	3.854 ± 0.200	0.64 ± 0.09
RS Cha	1.858 ± 0.016	1.036 ± 0.056	3.990 ± 0.010	0.94 ± 0.05
HD 75 747	1.821 ± 0.018	1.266 ± 0.055	3.954 ± 0.010	0.97 ± 0.05
V477 Cyg	1.79 ± 0.12	1.414 ± 0.051	3.946 ± 0.019	1.04 ± 0.07
HD 190 786	1.35 ± 0.07	1.133 ± 0.047	3.818 ± 0.025	0.35 ± 0.09
ZZ Boo	1.72 ± 0.08	1.605 ± 0.172	3.868 ± 0.012	0.83 ± 0.05
HD 121 648	1.72 ± 0.08	1.605 ± 0.172	3.868 ± 0.012	0.83 ± 0.05
TX Her	1.62 ± 0.04	1.509 ± 0.053	3.866 ± 0.010	0.77 ± 0.05
HD 156 965	1.45 ± 0.03	1.429 ± 0.050	3.826 ± 0.010	0.56 ± 0.05
PV Pup	1.565 ± 0.011	1.446 ± 0.018	3.842 ± 0.019	0.64 ± 0.08
HD 62 863	1.554 ± 0.013	1.409 ± 0.018	3.842 ± 0.019	0.62 ± 0.08
V442 Cyg	1.564 ± 0.024	1.495 ± 0.034	3.879 ± 0.010	0.81 ± 0.03
HD 33 4426	1.410 ± 0.023	1.403 ± 0.034	3.844 ± 0.006	0.61 ± 0.03
CW Eri	1.52 ± 0.015	1.443 ± 0.276	3.875 ± 0.019	0.77 ± 0.07
HD 19 115	1.28 ± 0.01	1.295 ± 0.100	3.821 ± 0.010	0.45 ± 0.07
RZ Cha	1.518 ± 0.021	1.469 ± 0.072	3.869 ± 0.012	0.76 ± 0.06
HD 93 486	1.509 ± 0.027	1.493 ± 0.030	3.866 ± 0.010	0.76 ± 0.04

Table 1. (Contd.)

Name/HD No.	$m(\mathrm{A})/m_\odot$ $m(\mathrm{B})/m_\odot$	$r(\mathrm{A})/m_\odot$ $r(\mathrm{B})/m_\odot$	$\log T_{\mathrm{eff}}(\mathrm{A})$, K $\log T_{\mathrm{eff}}(\mathrm{B})$, K	$\log L_{\mathrm{bol}}(\mathrm{A})/L_\odot$ $\log L_{\mathrm{bol}}(\mathrm{B})/L_\odot$
BW Aqr	1.49 ± 0.020	1.467 ± 2.208	3.843 ± 0.042	0.65 ± 0.06
BD - 16 6074	1.39 ± 0.020	1.436 ± 0.187	3.826 ± 0.014	0.57 ± 0.06
DM Vir	1.454 ± 0.008	1.427 ± 0.066	3.825 ± 0.009	0.56 ± 0.03
HD 123423	1.448 ± 0.008	1.419 ± 0.064	3.826 ± 0.020	0.56 ± 0.03
CD Tau	1.442 ± 0.016	1.246 ± 0.041	3.832 ± 0.003	0.47 ± 0.02
HD 34335	1.368 ± 0.016	1.296 ± 0.030	3.809 ± 0.003	0.41 ± 0.02
V1143 Cyg	1.391 ± 0.016	1.265 ± 0.023	3.808 ± 0.007	0.39 ± 0.03
HD 185 912	1.347 ± 0.013	1.238 ± 0.023	3.804 ± 0.007	0.35 ± 0.03
TV Cet	1.39 ± 0.05	1.399 ± 0.112	3.821 ± 0.010	0.52 ± 0.07
HD 20173	1.27 ± 0.04	1.197 ± 0.062	3.801 ± 0.007	0.31 ± 0.05
BS Dra	1.37 ± 0.03	1.330 ± 0.150	3.809 ± 0.012	0.43 ± 0.03
HD 190 020	1.37 ± 0.03	1.330 ± 0.150	3.809 ± 0.012	0.43 ± 0.03
HS Hya	1.34 ± 0.05	1.240 ± 0.140	3.810 ± 0.007	0.38 ± 0.09
HD 90 242	1.28 ± 0.05	1.136 ± 0.140	3.801 ± 0.007	0.27 ± 0.10
BK Peg	1.27 ± 0.01	1.251 ± 0.150	3.788 ± 0.005	0.29 ± 0.09
BD +255 003	1.43 ± 0.02	1.425 ± 0.275	3.817 ± 0.008	0.53 ± 0.09
UX Men	1.238 ± 0.006	1.124 ± 0.022	3.792 ± 0.007	0.22 ± 0.03
HD 37 513	1.198 ± 0.007	1.086 ± 0.020	3.787 ± 0.007	0.17 ± 0.03
VZ Hya	1.23 ± 0.03	1.175 ± 0.087	3.811 ± 0.008	0.33 ± 0.04
HD 72 257	1.12 ± 0.03	1.016 ± 0.045	3.793 ± 0.007	0.13 ± 0.04
FL Lyr	1.221 ± 0.016	1.159 ± 0.031	3.787 ± 0.009	0.22 ± 0.03
HD 179 890	0.960 ± 0.012	0.916 ± 0.030	3.719 ± 0.009	-0.24 ± 0.054
UV Psc	1.22 ± 0.08	0.967 ± 0.026	3.765 ± 0.010	-0.01 ± 0.05
HD 7700	0.87 ± 0.03	0.871 ± 0.030	3.694 ± 0.010	-0.38 ± 0.055
EW Ori	1.194 ± 0.014	1.106 ± 0.011	3.773 ± 0.007	0.06 ± 0.03
HD 287 727	1.158 ± 0.014	0.987 ± 0.011	3.757 ± 0.007	0.01 ± 0.03
WZ Oph	1.12 ± 0.04	1.114 ± 0.030	3.783 ± 0.005	0.18 ± 0.03
HD 154 676	1.12 ± 0.04	1.114 ± 0.030	3.783 ± 0.005	0.18 ± 0.03
UV Leo	1.105 ± 0.012	0.942 ± 0.073	3.764 ± 0.006	-0.04 ± 0.03
HD 92 109	1.105 ± 0.012	0.965 ± 0.073	3.762 ± 0.025	-0.03 ± 0.03
HS Aur	0.900 ± 0.019	0.883 ± 9.352	3.715 ± 0.113	-0.03 ± 0.35
BD +47 1350	0.879 ± 0.017	0.782 ± 1.677	3.703 ± 0.050	-0.44 ± 0.25
V539 Ara	6.24 ± 0.07	3.324 ± 0.085	4.286 ± 0.010	3.14 ± 0.05
HD 161 783	5.31 ± 0.06	3.118 ± 0.080	4.246 ± 0.010	2.92 ± 0.06
CV Vel	6.100 ± 0.044	3.317 ± 0.036	4.271 ± 0.012	3.08 ± 0.05
HD 77 464	5.996 ± 0.035	3.240 ± 0.036	4.267 ± 0.012	3.04 ± 0.05
AG Per	5.36 ± 0.16	2.769 ± 0.150	4.258 ± 0.020	2.83 ± 0.08
HD 25 833	4.90 ± 0.15	2.566 ± 0.150	4.221 ± 0.020	2.65 ± 0.08
U Oph	4.93 ± 0.05	2.990 ± 0.064	4.233 ± 0.040	2.84 ± 0.16
HD 156 247	4.56 ± 0.04	2.702 ± 0.050	4.209 ± 0.040	2.64 ± 0.16
DI Her	5.185 ± 0.108	2.528 ± 0.046	4.236 ± 0.020	2.70 ± 0.08
HD 175 227	4.534 ± 0.066	2.339 ± 0.045	4.185 ± 0.020	2.43 ± 0.08
V760 Sco	4.69 ± 0.17	2.781 ± 0.726	4.236 ± 0.027	2.77 ± 0.06
HD 147 683	4.42 ± 0.14	2.439 ± 0.423	4.221 ± 0.018	2.59 ± 0.05

these quantities using the formula

$$\Delta R^{\rm obs}(m^{\rm obs}, a_{\rm ZAMS}, Z_\odot) = [((\Delta R(m^{\rm obs}, a, Z))^2 + (\Delta R^{\rm obs})^2])^{1/2}, \quad (2)$$

where $\Delta R^{\rm obs}$ is the observational error of the radius and $\Delta R(m^{\rm obs}, a, Z) = F(m^{\rm obs}, a, Z, \Delta a, \Delta Z)$ is the error of the radius computed using the age and chemical composition computed in [6]. Figure 1 shows how Fig. 1 of [6] changes after introducing these evolutionary and metallicity corrections.

3. $(O-C)$ DIFFERENCES

Observations of binary stars (in contrast to clusters) are seldom used to test theoretical models. The Cambridge group [8] applied data for SB2 eclipsing systems to their computations and concluded that it was possible to fit the components of a single system using coeval models having the same chemical composition. They also evaluated their results with statistical tests (comparing the computed and predicted numbers of stars at various evolutionary stages). We use a different approach here.

Of the various observational parameters for the sample of 86 stars presented in Tables 2 and 3 of [6], we chose the masses and radii for our computations. We selected the age and metallicity of each system so that the computed masses and radii would be as close as possible to the corresponding observed values. The effective-temperature data can be used to compare the computations with observations, since the method used to derive them ensures that they are independent of both mass and radius. The luminosities were calculated from the observational radii and temperatures and are therefore less suitable for this purpose.

We now compute for each star the quantity

$$(O-C)_T = \log T_{\rm eff}^{\rm obs} - \log T_{\rm eff}(m^{\rm obs}, a, Z), \quad (3)$$

where $T_{\rm eff}^{\rm obs}$ is the observational effective temperature from Tables 2 and 3 of [6] and $T_{\rm eff}(m^{\rm obs}, a, Z)$ is the effective temperature calculated for the observational mass $m_{\rm obs}$ and computed a, Z. We can evaluate the agreement between the computations and observations using the overall characteristics of the $(O-C)$ values. The $(O-C)$ differences are equal to the distances of the points in Fig. 1 from the constant-mass ZAMS relations for solar chemical composition in the same figure [cf. (1) and (3)]. Therefore, these differences can also be viewed as deviations of the monometallic, semiempirical temperatures for the ZAMS from the corresponding theoretical values.

The errors are computed analogously to formula (2), i.e., as combinations of the errors of the observed and computed values. Note that, in most cases, the error of a computed quantity does not exceed the observational error, and, in more than half the cases, it is much lower than the observational error.

Table 2. Properties of the $(O-C)_T$ distributions: coefficient r for correlation with mass (the confidence interval is ± 0.11 in all cases) and validity of the hypothesis that the distributions are normal $P(\chi^2 \geq \chi_0^2)$

$O-C$	r	P
$(O-C)_T^0$	0.50	≤ 0.05
$(O-C)^{\rm G}$	0.18	0.38
$(O-C)^{\rm P}$	0.05	0.57
$(O-C)^{\rm Covs}$	0.18	0.82
$(O-C)^{\rm Cstd}$	0.14	0.35

To compare various models, we computed the quantities $(O-C)_T$ (and similarly $(O-C)_L$ for luminosities) based on the tracks computed by the Padova (P) and Geneva (G) groups. Because the theory of convective overshooting is now being widely discussed in connection with stellar evolutionary computations, we also used two models computed by the Cambridge group [9], which differ only in their treatment of this question. These are a so-called standard model with a Schwartzschild convective core (Cstd) and a convective-overshoot model (Covs). We propose, first, to assess differences between the tracks with and without overshooting (Cstd, Covs) for the observed parameters of MS stars and, second, to compare the results obtained with different overshoot models (G, P, Covs). We computed a, Z for the systems studied using the Covs and Cstd tracks (in a way similar to that described in [6]), then determined $(O-C)$.

In addition to $(O-C)^{\rm G}$, $(O-C)^{\rm P}$, $(O-C)^{\rm Covs}$, and $(O-C)^{\rm Cstd}$, we construct for comparison a number of other quantities, which we refer to by analogy as $(O-C)^0$:

$$(O-C)_T^0 = \log T_{\rm eff}^{\rm obs} - \log T_{\rm eff}(m^{\rm obs}, a_{\rm ZAMS}, Z_\odot), \quad (4)$$

which are the distances from the observational data points to the mass–effective temperature relation (MTR) at a given mass. We now analyze the distributions of these quantities.

Note that $(O-C)_T^0$ shows some correlation with mass (see the linear correlation coefficients in Table 2), as is quite natural, whereas there is virtually no correlation for the other $(O-C)_T$ relations. The χ^2 values in Table 2 show the probability that the $(O-C)_T$ distributions are normal. We can seen from the table that this hypothesis can be refuted in none of

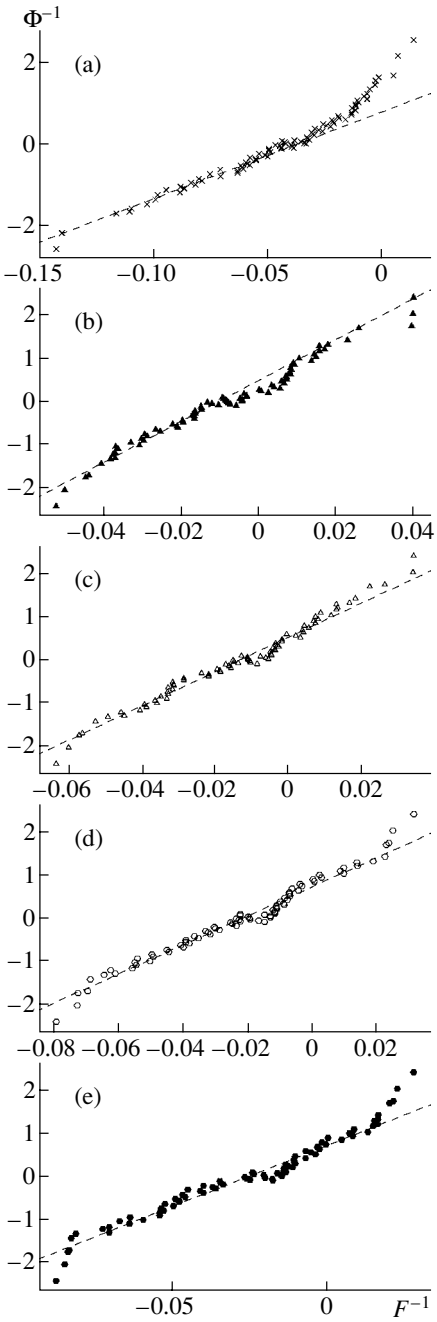

Fig. 2. Distributions of $(O-C)_T$ in the inverse sample distribution function–inverse Laplace function plane (a eyeball test that the distributions are normal): (a) $(O-C)^0_T$, (b) $(O-C)^{\mathrm{Cstd}}_T$, (c) $(O-C)^{\mathrm{Covs}}_T$, (d) $(O-C)^{\mathrm{P}}_T$, (e) $(O-C)^{\mathrm{G}}_T$. Approximating lines fit to the first half of the samples are also drawn.

the cases except $(O-C)^0_T$. Figure 2 shows the distributions of $(O-C)_T$ in the inverse sample function–inverse Laplace function plane (providing a so-called eyeball test of whether the distributions are normal [10]). The deviations of the data points in these figures from straight lines correspond to deviations from a normal distribution. Figure 2a (the inverse $(O-C)^0_T$ sampling distribution function) shows the presence of systematic deviations, which are not apparent in any of the other cases (although there are a few outliers, especially at the maximum values along the horizontal axes, which were not used in our subsequent analysis).

Given the normal nature of the series on the whole, we discarded stars with large $(O-C)$ values using the criterion of Chauvenet; this excluded three stars for the P and G tracks and seven for the Cstd and Covs tracks. The larger fraction of unsatisfactory fits for the Cstd and Covs models may be due to their relatively narrow metallicity range: in [9], models without overshooting were computed only for $Z = 0.01$, 0.02, and 0.03. We accordingly restricted our computations with the Covs models to the same chemical compositions to facilitate a trustworthy comparison with our results.

We thus have the four series $(O-C)^{\mathrm{G}}$, $(O-C)^{\mathrm{P}}$, $(O-C)^{\mathrm{Covs}}$, and $(O-C)^{\mathrm{Cstd}}$, which have approximately normal distributions and do not depend directly on the mass. In the ideal case, $(O-C)$ forms a series of random observational errors without any systematic component due to evolution or the dispersion in chemical composition. In all four cases, the distributions of $(O-C)$ prove to be biased. These small biases are due to the existence of a lower bound for the age (ZAMS) and the fact that a considerable number of stars in our sample are close to this boundary (the upper bound for the age can be taken to be infinitely remote for all the objects studied and all models considered). This inevitable byproduct of this type of computation is also present in the results of [8] when the observed luminosities are compared with those corresponding to the computed a, Z values. The mean $(O-C)$ bias is determined by the technical details of the method employed; it appears to be unrelated to the degree of agreement between the observations and computations and has no effect on our subsequent discussion. We will analyze the uniformity of the closeness of the computed and observed parameters; i.e., how the distribution of $(O-C)$ behaves in different mass intervals.

4. SMOOTHING OF $(O-C)$

To establish the behavior of $(O-C)$ as a function of mass, we used a smoothing technique similar to a moving average [10]. We made a transformation from the initial series values to their arithmetic means over mass intervals. The number of data points was the same in each interval, so that the lengths of the intervals varied significantly. After testing using various numbers of data points per interval, we chose

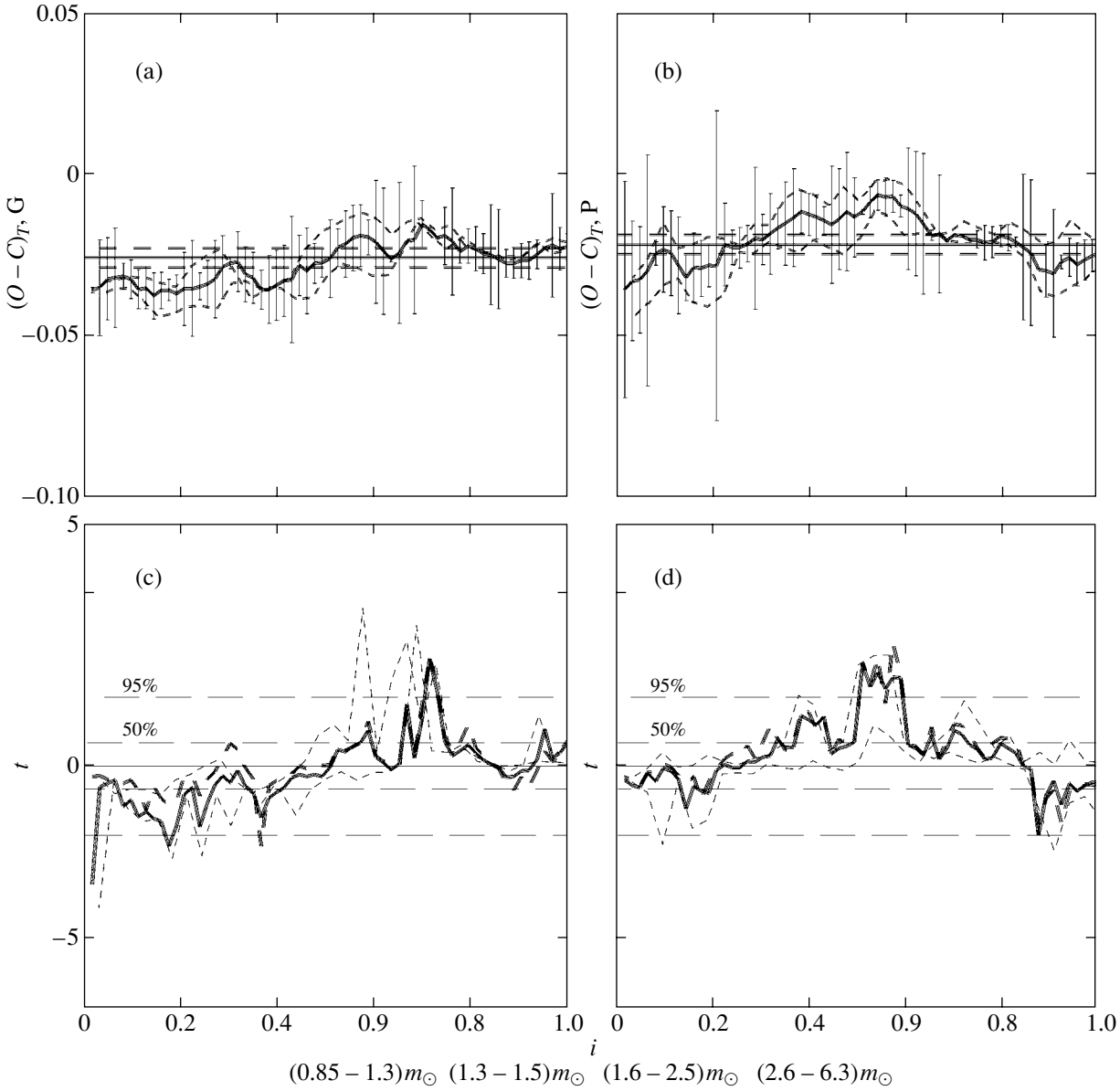

Fig. 3. Smoothed $(O-C)_T$ (a, b, e, g) and the probability of a nonrandom deviation of the mean $(O-C)_T$ for the ith interval from the mean over the entire range (b, d, f, h) for the G, P, Covs, and Cstd models, respectively. The horizontal axis plots the number of the mass interval normalized to unity ($i = n/N$). The negative shift of the mean $(O-C)_T$ throughout the entire mass range is due to the asymmetric nature of the stellar-age distribution (see Section 3). The solid curves show $(O-C)_T$ values smoothed over 20 data points, and the dashed curves show smoothed $(O-C)_T$ for even and odd numbers of the stellar series sorted by mass. The solid horizontal line shows the mean $(O-C)_T$ for the ensemble, and the long dashed lines, its standard deviation. Plots b, d, f, and h also show the probability of a nonrandom deviation of the mean $(O-C)_L$ (bold dashed lines).

$N = 20$ (making N too large would inevitably smooth out all features, whereas making it too small would make it impossible to neglect statistical fluctuations. Our estimates show that varying N within reasonable limits (± 10) does not affect our conclusions).

The $(O-C)$ distributions in smoothed intervals remain close to normal, making it possible to compute the probability of nonrandom deviations of the mean for each interval from the mean for the entire distribution. Figure 3 shows smoothed $(O-C)_T$ curves for all the tracks studied, together with these probabilities. It is clear that even the behavior of the smoothed curve is, to some extent, determined by the chosen sample of stars. To assess the influence of our choice of objects on the behavior of the smoothed curve, we subdivided the $(O-C)$ series into two parts

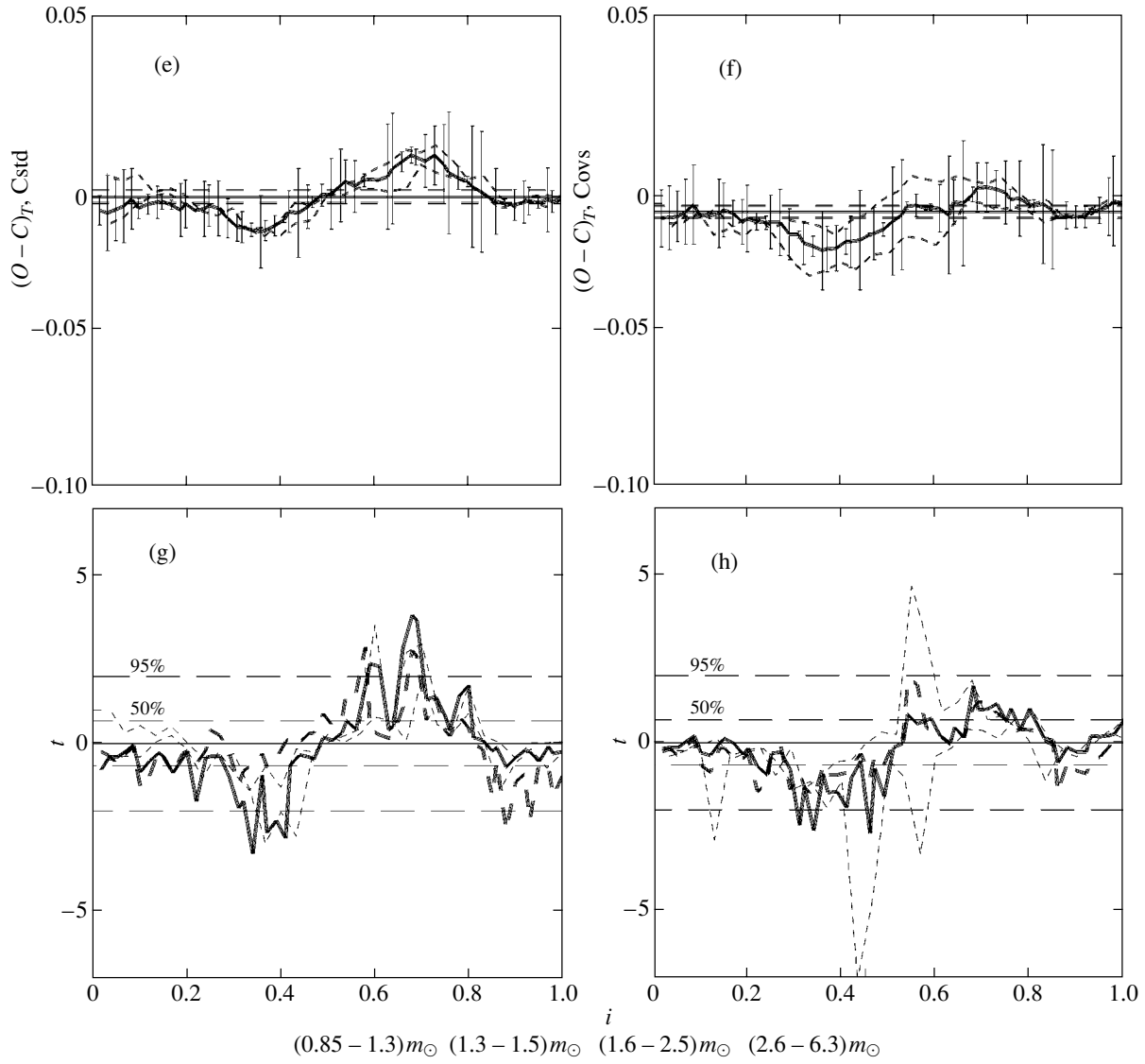

Fig. 3. (Contd.)

by numbering $(O-C)_T^i$ in order of increasing stellar mass and dividing the sample into even- and odd-numbered data points. The smoothed $(O-C)_T$ for the even ($(O-C)_T$(e)) and odd ($(O-C)_T$(o)) points are also shown in Fig. 3. On the whole, the two series exhibit very similar behavior (the linear-correlation coefficients (e) and (o) for the different models range from 0.87 to 0.96 for a confidence interval of 0.13). However, of the two main features shown by $(O-C)_T$ (a dip in the mass interval $(1.1-1.5)m_\odot$ and a rise at $m > 1.5m_\odot$), only the rising portion is present in both subsamples. The dip visible for only one half of the sample must be considered to have low statistical significance and to be a random fluctuation.

The statistically significant excess near $1.5m_\odot$ appears to have the following origin. Ribas *et al.* [11] showed that photometric effective temperatures $T_{\rm eff}^{\rm phot}$ were systematically shifted relative to temperatures derived from stellar radii using Hipparcos parallaxes ($T_{\rm eff}^{\rm Hip}$), with the shift depending on temperature. Although the parallax temperatures are constrained by the BC – $T_{\rm eff}$ relation and therefore cannot be completely independent, Ribas *et al.* [11] point out that these temperatures should be more accurate than photometric temperatures. We now analyze how our $(O-C)_T$ relations change if we introduce the corresponding correction to our observed (photometric) temperatures.

We computed the corrections to $(O-C)_T$ as follows. For 40 stars from Table 1 in [11], we computed $(O_{\rm Hip}-O_{\rm phot}) = \log T_{\rm eff}^{\rm Hip} - \log T_{\rm eff}^{\rm phot}$ (excluding the system V1647 Sgr, as in [11]) and estimated

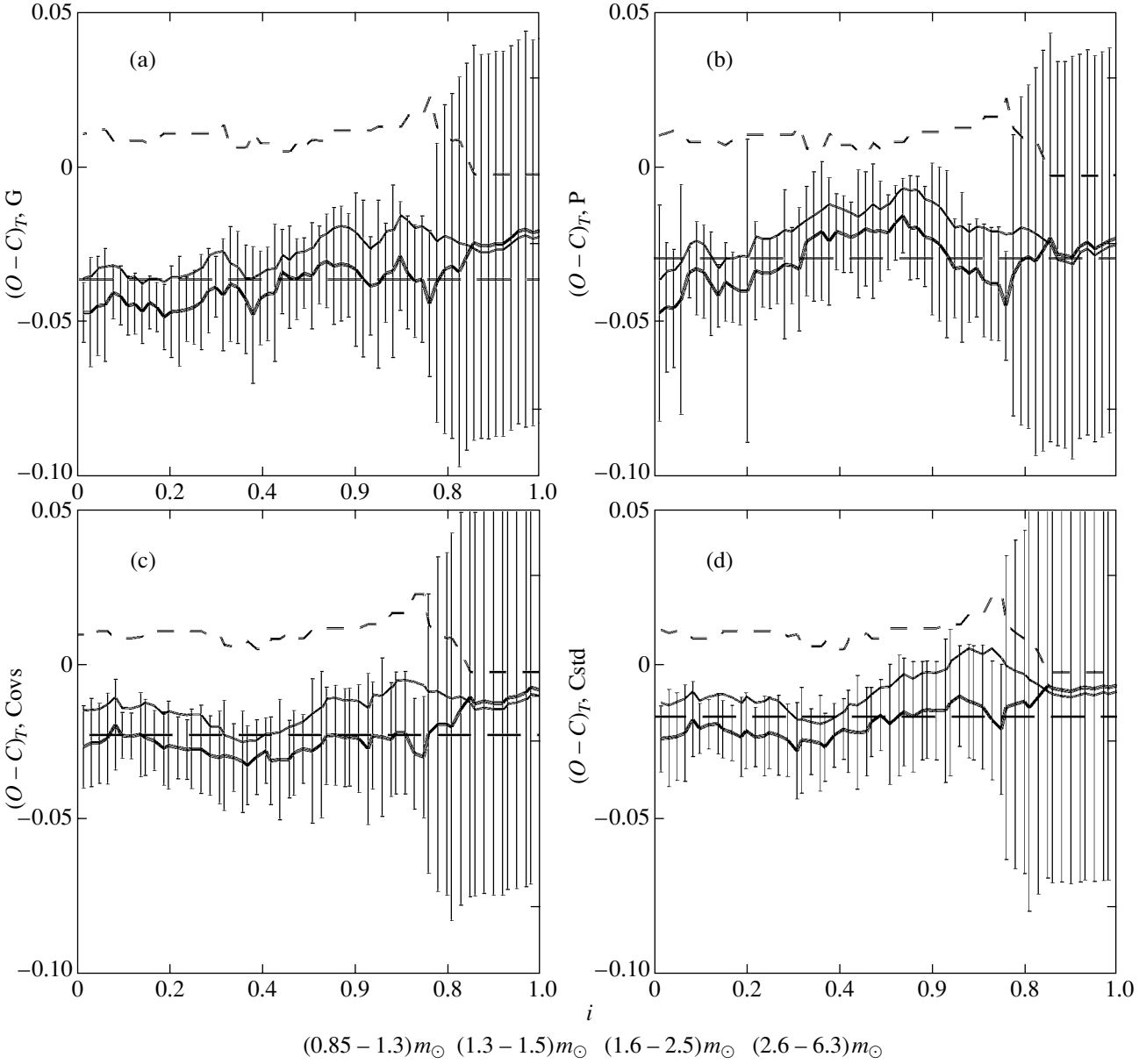

Fig. 4. Smoothed $(O-C)_T$ for models (a) G, (b) P, (c) Covs, and (d) Cstd (thin solid curves), the computed correction $(O_{\rm Hip}-O_{\rm phot})$ (dashed curves), and their sum—the smoothed $(O-C)_T$ corrected for inhomogeneity of the photometric effective-temperature estimation (bold solid curves).

the masses from the theoretical MTR. The accuracy of the resulting masses is $(0.1-0.3)m_\odot$ (based on the errors in the effective temperatures). We then smoothed the correction $(O_{\rm Hip}-O_{\rm phot})$ in the same way as for $(O-C)$ for the same mass intervals (thus the condition of constant number of data points within a mass interval for $(O_{\rm Hip}-O_{\rm phot})$ was retained, preserving the scale).

Figure 4 shows the smoothed $(O-C)_T$ and $(O_{\rm Hip}-O_{\rm phot})$ and the smoothed $(O-C)_T-(O_{\rm Hip}-O_{\rm phot})$ corrected for the photometric temperature shift for all four theoretical models. It is evident that the positions of the maxima of $(O-C)_T$ and $(O_{\rm Hip}-O_{\rm phot})$ on the Cstd and Covs tracks coincide and that the corrected relations become virtually monotonic. We found no significant differences between the results for models with and without overshooting. The maxima for models G and P are somewhat shifted relative to the maximum of $(O_{\rm Hip}-O_{\rm phot})$, so the corresponding features do not disappear altogether but become insignificant. The sharp increase in the errors in $(O-C)_T-(O_{\rm Hip}-O_{\rm phot})$ toward large masses is due to the considerable scatter of $(O_{\rm Hip}-$

Table 3. Empirical and averaged semiempirical MLR, MTR, and MRR. The mean approximation error is shown for the empirical relations

$m/m_\odot$	$\log L^{\rm emp}/L_\odot$	$\log L^{\rm semi-emp}/L_\odot$	$\log T_{\rm eff}^{\rm emp}$	$\log T_{\rm eff}^{\rm semi-emp}$	$\log r^{\rm emp}/r_\odot$	$\log r^{\rm semi-emp}/r_\odot$
0.900	-0.1633 ± 0.10	-0.522 ± 0.121	3.7186 ± 0.027	3.677 ± 0.013	-0.0425 ± 0.068	-0.125 ± 0.089
1.010	0.0176	-0.268 ± 0.099	3.7410	3.710 ± 0.011	0.0242	-0.051 ± 0.072
1.120	0.1895	-0.036 ± 0.080	3.7629	3.741 ± 0.009	0.0808	0.010 ± 0.057
1.230	0.3529	0.175 ± 0.066	3.7843	3.771 ± 0.008	0.1286	0.060 ± 0.045
1.340	0.5079	0.367 ± 0.054	3.8053	3.799 ± 0.007	0.1686	0.101 ± 0.035
1.450	0.6550	0.540 ± 0.047	3.8258	3.826 ± 0.008	0.2020	0.135 ± 0.027
1.560	0.7942	0.698 ± 0.042	3.8459	3.851 ± 0.008	0.2297	0.162 ± 0.021
1.670	0.9259	0.840 ± 0.039	3.8655	3.875 ± 0.008	0.2527	0.183 ± 0.016
1.780	1.0505	0.968 ± 0.038	3.8847	3.898 ± 0.009	0.2716	0.201 ± 0.012
1.890	1.1681	1.085 ± 0.038	3.9033	3.919 ± 0.009	0.2873	0.214 ± 0.010
2.000	1.2790	1.190 ± 0.039	3.9215	3.939 ± 0.009	0.3002	0.226 ± 0.008
2.450	1.6692	1.526 ± 0.041	3.9911	4.009 ± 0.009	0.3356	0.257 ± 0.008
2.900	1.9714	1.763 ± 0.046	4.0528	4.063 ± 0.008	0.3594	0.285 ± 0.014
3.350	2.2044	1.953 ± 0.057	4.1064	4.104 ± 0.008	0.3831	0.320 ± 0.017
3.800	2.3870	2.133 ± 0.068	4.1518	4.137 ± 0.010	0.4081	0.361 ± 0.017
4.250	2.5382	2.323 ± 0.074	4.1891	4.164 ± 0.013	0.4318	0.399 ± 0.012
4.700	2.6768	2.528 ± 0.072	4.2179	4.189 ± 0.014	0.4525	0.423 ± 0.007
5.150	2.8216	2.735 ± 0.063	4.2384	4.215 ± 0.013	0.4743	0.432 ± 0.004
5.600	2.9916	2.915 ± 0.050	4.2503	4.248 ± 0.009	0.5127	0.436 ± 0.004
6.050	3.2055	3.024 ± 0.039	4.2535	4.289 ± 0.005	0.5998	0.468 ± 0.032

$O_{\rm phot}$) in [11]. It is possible that the tendency for a small increase of $(O-C)_T - (O_{\rm Hip} - O_{\rm phot})$ with increasing mass, which is present for all the models, is due to insufficient adequacy in the computation of $(O_{\rm Hip} - O_{\rm phot})$ for bright stars (see Fig. 2 in [11]).

The coincidence of the positions of the features for $(O-C)_T$ and $(O_{\rm Hip} - O_{\rm phot})$ should not be interpreted as evidence in favor of the Cambridge models. First, after being corrected for the systematic shift of the photometric temperatures, all deviations of the corrected $(O-C)_T$ values from the corresponding mean are within the quoted errors. Second, differences between the positions of the maximum of $(O-C)$ for all tracks do not exceed $0.2m_\odot$ at the centers of the intervals averaged. This means that they are within the errors in the masses estimated from the effective temperatures for the sample [11]. Third, the tracks computed by the Cambridge group yield obviously underestimated $(B-V)$ values, and, consequently, overestimated effective temperatures in the interval $0.4 < (B-V) < 0.8$ (see, e.g., Figs. 4, 7, 8 in [9]). These color indices correspond approximately to the mass interval $1m_\odot < m < 1.5m_\odot$. In this case, the corrected relation for the Cambridge models should exhibit a minimum in the corresponding region; i.e., the maximum of $(O_{\rm Hip} - O_{\rm phot})$ should be more prominent and possibly compensate the features in models G or P. Thus, the solution of this problem requires more precise elucidation of the nature of the systematic errors in the effective temperatures, or alternatively the mass application of other methods for determining these temperatures.

The above discussion concerning $(O-C)_T$ is also fully applicable to $(O-C)_L$, since the behavior of $(O-C)_L$ is mainly determined by the form of $(O-C)_T$. The difference between the observed and computed radii $(O-C)_R$ can be minimized by choosing appropriate ages and metallicities. The sample of these quantities does not obey a normal distribution and has no systematic features, so its form has virtually no effect on $(O-C)_L$. Figure 3 illustrates this

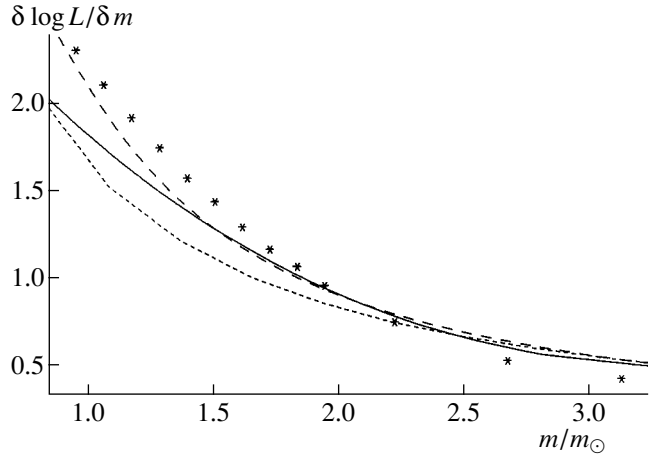

Fig. 5. Behavior of the derivative of various MLRs: theoretical relation (long dashes—Cambridge MLR); mean semiempirical relation (asterisks); empirical relation approximated by a polynomial (solid curve); and empirical relation approximated by a logarithmic function [5] (dashed curve).

statement: the behavior of the probabilities of nonrandom deviations of the mass-interval means from the overall mean is nearly the same for $(O-C)_T$ and $(O-C)_L$.

5. SEMIEMPIRICAL MASS–LUMINOSITY, MASS-RADIUS, AND MASS–EFFECTIVE TEMPERATURE RELATIONS

Finally, we analyzed the resulting (see Section 2) semiempirical mass–luminosity, mass–radius, and mass–effective temperature relations (MLR, MRR, and MTR; the MRR uses the logarithm of the radius) by comparing them with theoretical and empirical relations. We obtained a weighted-average polynomial fit of the positions of observed ZAMS stars with solar metallicity. The weights were inversely proportional to the combined errors of the observations and computations (see Section 2). We chose the degree of the polynomial based on the following criterion. Suppose we have N points $(m_i, f_i \pm \sigma_{f_i})$ approximated by a polynomial F_n of degree n. The accuracy of the fit can be characterized by the quantity

$$\tilde{\chi}^2 = \frac{\chi^2}{d}, \tag{5}$$

where $d = N - n$ is the number of degrees of freedom for

$$\chi^2 = \sum_{i=1}^{N} \frac{F_n(m_i) - f_i^2}{\sigma_{f_i}^2 + \sigma_{F_n}^2} \tag{6}$$

and σ_{F_n} is the standard deviation of the coefficients of the approximating IDL function.

The quantity χ^2 decreases with increasing n, however, d also decreases and $\tilde{\chi}^2$ has a minimum at some n^0, which is the chosen degree of the fitting polynomial. The value of $\tilde{\chi}^2$ at the minimum corresponds to probabilities 65–99%, and $\tilde{\chi}^2(n_0) \geq 95\%$ in most cases.

We have for the empirical (initial) and semiempirical (corrected for evolutionary effects and the metallicity dispersion) relations: $n^0 = 4$ (MLR), $n^0 = 3$ (MTR), and $n^0 = 5$ (MRR). The empirical relations are shown in Fig. 1 and listed in Table 3. Note that σ in this table characterizes the accuracy of the fit and is not equal to the half-width of the empirical relations (which, in turn, can be estimated from Fig. 1 in [6]).

We computed the mean semiempirical relations and their errors based on four semiempirical relations constructed for various theoretical models. They are also shown in Fig. 1 and presented in Table 3. These relations are well defined for the mass interval $(1-2)m_\odot$ (since it is highly populated) and are accordingly tabulated in more detail. The uncertainties in the interval $(3-6)m_\odot$ are much higher, due to the small number of observed objects and, as expected, exceed the formal errors from Table 3.

It is of interest to compare the behavior of the derivative of the MLR for the theoretical and approximated empirical and semiempirical relations. Let us consider only the region where the empirical relations are reasonably well defined. Figure 5 presents the derivatives of MLRs determined in various ways: the theoretical MLR (Covs; the difference between the derivatives of different theoretical MLRs is essentially zero for $m \geq 1.5m_\odot$ and does not exceed 0.1 in $d\log L/dm$ for $m \leq 1.5m_\odot$, as far as we can judge, given the relatively large mass step adopted by the Padova and Geneva groups), mean semiempirical MLR, our own empirical polynomial-approximation

MLR, and, for comparison, the commonly used logarithmic approximation of the empirical MLR [5]. In the region considered, the logarithmic approximation is less suitable in terms of the closeness of its derivative to the theoretical derivative. The derivative of the semiempirical MLR is clearly overestimated in the mass interval $(1.2-1.7)m_\odot$, whereas the derivative of the empirical logarithmic approximation agrees almost perfectly with the theoretical derivative for $m \geq 1.4m_\odot$. This may indicate that the amount of observational data for masses near $m = 1.5m_\odot$ is insufficient for our task. On the other hand, for masses below $1.2m_\odot$, the derivatives of the empirical and semiempirical MLRs are in better agreement than those of the theoretical and empirical polynomial or logarithmic approximations. This is precisely the region where the turnoff of the observed luminosity function lies, and the derivative of the MLR can be used to correctly take into account the star-formation history when constructing the IMF.

We can see that differences between the behavior of the derivatives of different MLRs become important for masses below $2m_\odot$ and can reach 0.5 in $d\log L/dm$ for masses $1m_\odot$. The relative scatter of these quantities is about a factor of two higher for $m \approx 1m_\odot$ than for $m \approx 2m_\odot$.

6. CONCLUSIONS

We have analyzed systematic differences between theoretical computations and observations using data for the MS components of SB2 eclipsing binary systems. We have compared parameters (the effective temperatures) estimated using theoretical computations together with the observational masses and radii of the stars, assuming a common origin (age and metallicity) for all components of a given system and corresponding values of the observed parameters.

We found that $(O-C)_T$ follows a normal distribution. The observed shift of the ensemble-averaged $(O-C)_T$ is associated with the specific nature of the method employed (the lower bound for the age in the tracks used, which distorts the age distribution) and of the distribution of the stars in the Hertzsprung–Russell diagram. We analyzed shifts of the mean $(O-C)$ averaged over various mass intervals relative to the ensemble-averaged mean in order to elucidate possible origins for these shifts. The dip in $(O-C)$ computed for four sets of models in the mass interval $(1-1.5)m_\odot$ is not real and appears to be a random fluctuation associated with individual peculiarities of the sample used. At the same time, the maximum exhibited by all the $(O-C)_T$ curves at $m \geq 1.5m_\odot$ is statistically significant and not random. This maximum is due to a systematic shift of the photometric effective-temperature scale, as is evident from a comparison with temperatures determined using Hipparcos data [11].

Thus, the results of our analysis lead us to conclude that there is no statistically significant evidence for systematic differences between the observed and computed stellar parameters that could not be due to observational uncertainties or computational errors. The models analyzed approximate the parameters of stars with a range of moderate masses well and uniformly.

In addition, note that our analysis for main-sequence stars does not provide any means to distinguish between models with and without convective overshooting.

Based on selected accurate observational data, we have proposed polynomial fits to the empirical MLR, MTR, and MRR. In the mass interval $(1-3)m_\odot$, the polynomial approximation is preferable to the logarithmic approximation in terms of the agreement between the slopes of the empirical and theoretical MLRs.

Our conclusion that the results of theoretical computations approximate the observational data in a uniform way suggests the use of mean, semiempirical relations between the mass and other parameters derived from empirical data taking into account effects associated with the dispersions in the ages and chemical compositions of field stars. In most cases, the computed uncertainties in the corrections are considerably smaller than the observational errors. The proposed semiempirical relations result from transforming the observational empirical relations into relations that are uniform in evolutionary status and metallicity. The width of these relations is determined primarily by random observational errors and can be reduced as further observations become available (in contrast to the widths of empirical relations, which are appreciably influenced by evolutionary effects and the metallicity dispersion, even at the currently achieved accuracy). The semiempirical relations are in best agreement with the theoretical models in the important region $m \approx 1m_\odot$, whereas empirical relations show maximum deviations from the computed relations for such masses.

7. ACKNOWLEDGMENTS

I am sincerely grateful to A.É. Piskunov for his ongoing assistance and to N.N. Chugai and Dr. Zahn for useful comments. I am grateful to Dr. Pols for the evolutionary tracks kindly provided. This work was supported by the Support of Young Scientists program of the Russian Academy of Sciences, a grant of the President of the Russian Federation (project no. 99-15-96022) and the Russian Foundation for Basic Research (project no. 00-15-96722).

REFERENCES

1. O. Yu. Malkov, Candidate of Science Dissertation in Physics and Mathematics (Moscow, 1993).
2. D. M. Popper, Ann. Rev. Astron. Astrophys. **18**, 115 (1980).
3. J. Andersen, Astron. Astrophys. Rev. **3**, 91 (1991).
4. O. Malkov, A. Piskunov, and D. Shpil'kina, Astron. Astrophys. **320**, 79 (1997).
5. S. Yu. Gorda and M. A. Svechnikov, Astron. Zh. **75**, 896 (1998) [Astron. Rep. **42**, 793 (1998)].
6. D. A. Kovaleva, Astron. Zh. **78**, 1104 (2001) [Astron. Rep. **45**, 972 (2001)].
7. F. D'Antona, in *The Stellar Initial Mass Function: 38th Herstmonceux Conference,* Ed. by G. Gilmore and D. Howell, Astron. Soc. Pac. Conf. Ser. **142**, 157 (1998).
8. O. R. Pols, C. A. Tout, K. P. Shröder, *et al.*, Mon. Not. R. Astron. Soc. **289**, 869 (1997).
9. O. R. Pols, K. P. Shröder, J. R. Hurley, *et al.*, Mon. Not. R. Astron. Soc. **298**, 525 (1998).
10. Yu. N. Tyurin and A. A. Makarov, *Statistical Data Analysis by Computer,* in Russian, Ed. by V. E. Figurnov (Infra-M, Moscow, 1998).
11. I. Ribas, A. Gimenez, J. Torra, *et al.*, Astron. Astrophys. **330**, 600 (1998).

Translated by A. Dambis

Astronomy Reports, Vol. 46, No. 3, 2002, pp. 246–254. Translated from Astronomicheskiĭ Zhurnal, Vol. 79, No. 3, 2002, pp. 272–280.

Sources of the Global Magnetic Field of the Sun

V. A. Kotov[1] and I. V. Setyaeva[2]

[1]*Crimean Astrophysical Observatory, Nauchnyĭ, Crimea, 334413 Ukraine*

[2]*Geographical Department, Moscow State University, Moscow, 119899 Russia*

Received January 17, 2001

Abstract—Data on the global magnetic field (GMF) of the Sun as a star for 1968–1999 are used to determine the correlation of the GMF with the radial component of the interplanetary magnetic field (IMF) $|B_r|$; all data were averaged over a half year. The time variations in the GMF $|H|$ are better correlated with variations in $|B_r|$ than the results of extrapolating the field from the "source surface" to the Earth's orbit in a potential model based on magnetic synoptic maps of the photosphere. Possible origins for the higher correlation between the GMF and IMF are discussed. For both the GMF and IMF, the source surface actually corresponds to the quiet photosphere—i.e., background fields and coronal holes—rather than to a spherical surface artificially placed $\approx 2.5\ R_\odot$ from the center of the Sun, as assumed in potential models ($R_\odot$ is the solar radius). The mean effective strength of the photospheric field is about 1.9 G. There is a nearly linear dependence between $|H|$ and $|B_r|$. The strong correlation between variations in $|H|$ and $|B_r|$ casts doubt on the validity of correcting solar magnetic fields using the so-called "saturation" factor δ^{-1} (for magnetograph measurements in the λ 525.0 nm FeI line).

1. INTRODUCTION

Active processes on the Sun and in the interplanetary medium are mainly controlled by the strong magnetic fields of active regions (ARs). At the same time, the sector structures in the polarity distributions of the global magnetic field (GMF) of the Sun as a star and of the interplanetary magnetic field (IMF) depend mainly on the pattern of weak, large-scale (background) fields outside ARs. Moreover, regular heliospheric magnetic fields and processes such as cosmic-ray modulation also depend chiefly on the background fields [1]. For this reason, the IMF polarity distribution is frequently used to analyze the structure and evolution of large-scale solar fields, and, under certain assumptions, measurements of the IMF *strength* can be used to improve the calibration of measurements of the photospheric magnetic field (see Section 6).

At the same time, on average, potential models describing the field in the transition region between the photosphere and the so-called source surface are in good agreement with the sector structure of the heliospheric field. However, such models cannot explain the actual IMF strengths at the Earth's orbit. (It is usually assumed that the base of the heliosphere, or the spherical source surface, is $R_S = (2.35–3.25)\ R_\odot$ from the center of the Sun, where $R_\odot$ is the solar radius; see, e.g., [1–3] for more details.)

In 1971, Wilcox [4] suggested that a special organization is inherent in the GMF, independent of the configuration of ARs—the basic element of the Babcock–Leighton model for the solar cycle. In this case, the boundaries of the background fields are stretched in the north–south direction, and do not experience differential rotation, while the magnetic fluxes of ARs are essentially balanced. Thus, it is the total signal of the background fields that should dominate in both the GMF and IMF. In this view, the GMF and IMF are relatively independent of the fields of sunspots and ARs [5, 6].

In GMF measurements [7–11], the longitudinal Zeeman effect for a photospheric absorption line is recorded using light from the entire solar disk. Therefore, the solar-magnetograph signal used to determine the GMF is a weighted average of all the photospheric fields, including the mean fields of coronal holes, spots, and ARs (or, more precisely, the mean line-of-sight components of these fields; limb-darkening makes the main contribution to the weighting function).

IMF measurements obtained using the *Ulysses* magnetometer [12] have demonstrated that the radial component of the IMF $|B_r|$ does not depend on heliographic latitude φ. Accordingly, Wang and Sheeley [3] extrapolated the photospheric field to the Earth's orbit using a potential model (for a spherical shell between $R_\odot$ and $R_S = 2.5\ R_\odot$) and the concept of the

1063-7729/02/4603-0246$22.00

source surface. Comparisons with the measured IMF showed that the solar-magnetograph data (obtained in the λ 525.0 nm FeI line) should be increased by a factor

$$\delta^{-1} = 4.5 - 2.5\sin^2\varphi, \quad (1)$$

which depends on the heliographic latitude (and takes into account the so-called line-saturation effect, see Section 2). This implies that the field increases sharply at the poles during epochs of solar-activity minima, reaching a mean value of about 10 G in the polar coronal hole. Wang and Sheeley [3] compared the component B_r of the IMF with the solar magnetic field using magnetic synoptic maps obtained at the Mt. Wilson Observatory (MWO) and Wilcox Solar Observatory (WSO) in 1970–1993. Here, we are interested in knowing (i) how necessary it is to introduce the saturation factor δ^{-1}, (ii) what its role is in comparing another important parameter of solar magnetism—the GMF—with the IMF, (iii) whether IMF measurements can be used to improve the calibration of photospheric-field measurements (GMF measurements, in particular), (iv) to what extent an extrapolation of synoptic maps can unambiguously represent the IMF at the Earth's orbit, and (v) what the role of the GMF is in this context and what the main photospheric sources of the GMF and IMF are.

2. THE SATURATION FACTOR

It is usually believed that magnetograph signals in the λ 525.0 line are underestimated, since (i) the photospheric magnetic fields are concentrated in thin ropes less that 1″ across with field strengths of $\approx$1.5 kG, resulting in "saturation" of the Zeeman polarization signal [13, 14] and (ii) the depths of lines with low excitation potentials (in particular, the λ 525.0 line) decrease due to the increase of the temperature in magnetic elements, which additionally lowers the signal. For this reason, a multiplicative factor δ^{-1} that depends on the heliocentric distance ρ is used to correct the measurements. (In this connection, some observers prefer to use other lines that are less sensitive to the magnetic field (and therefore less subject to saturation) when measuring magnetic fields, such as the λ 523.3 FeI line; see, e.g., [15].)

Relationship (1) was derived by Ulrich [16] from MWO magnetograms obtained in the λ 525.0 and λ 523.3 FeI lines. (In the original formula, the heliocentric angle θ was used in place of φ, and the spatial resolution of the magnetograms was taken into account [3].) However, the MWO data [13] show that, for $\theta < 60°$, the saturation factor varies from the center to the limb as

$$\delta^{-1} = 0.48 + 1.33(1-\rho^2)^{1/2} \approx 1.8 - 0.9\sin^2\theta, \quad (2)$$

which differs substantially from (1) with θ replaced by φ (the ratio of the mean values of δ^{-1} is about 2.5 for $\theta < 60°$).

A different δ^{-1} factor was obtained in 1978 by Svalgaard *et al.* [17] from WSO magnetograms [17] (λ 525.0, with a resolution of 175″ × 175″); they found that $\delta^{-1} = 1.8$, completely independent of $\rho = \sin\theta$.

Interesting results were also obtained in Crimean observations: the measured line-of-sight field depended not only on ρ, but possibly also on the magnetic sensitivity of the line $g\lambda^2$ and its equivalent width (g is the Landé factor and λ the wavelength) [18, 19]. Howard and Stenflo [13] and Gopasyuk [20] suggested that the discrepancy between the strengths measured in different lines was due to variations of the field in the solar atmosphere with height (accompanied by divergence of the field lines), temperature effects, and superfine field structure.

3. EXTRAPOLATION OF THE PHOTOSPHERIC FIELD

The result of [3] is based on a calculation of the open magnetic flux from the Sun, $|F_S|$, based on the magnitudes of the photospheric fields and proportionality to $|B_r|$ (by definition, magnetic configurations are called open if their magnetic field lines reach the source surface). The data on the photospheric fields were taken from MWO and WSO synoptic maps spanning the 24 years from 1970 to 1993 by Wang and Sheeley [3]. They used a potential approximation to calculate the total flux $|F_S|$ and extrapolate it into the corona, employing a thin-layer model for extrapolation into the heliosphere. They assumed that the measured line-of-sight photospheric field corrected for the effects of projection and saturation is the radial component of a potential field (see [2] for more details). No electric currents are present in the coronal region between the photosphere and the spherical source surface at radius $R_S = 2.5\ R_\odot$. The magnetic field lines at the source surface are radial, and the magnitude of the radial component of the IMF at a distance $R = R_E$ from the Sun (at the Earth's orbit) is

$$|B_r| = \frac{|F_S|}{4\pi R_E^2}. \quad (3)$$

The model assumes that, on average, the magnetic flux at the Earth's orbit is distributed isotropically.

Wang and Sheeley [3] constructed time-variation curves for three-month moving averages of the radial IMF component $|B_r|$ measured by satellites and the extrapolated radial component computed from synoptic maps. They found that, using the Stanford factor $\delta^{-1} = 1.8$, there was a significant discrepancy

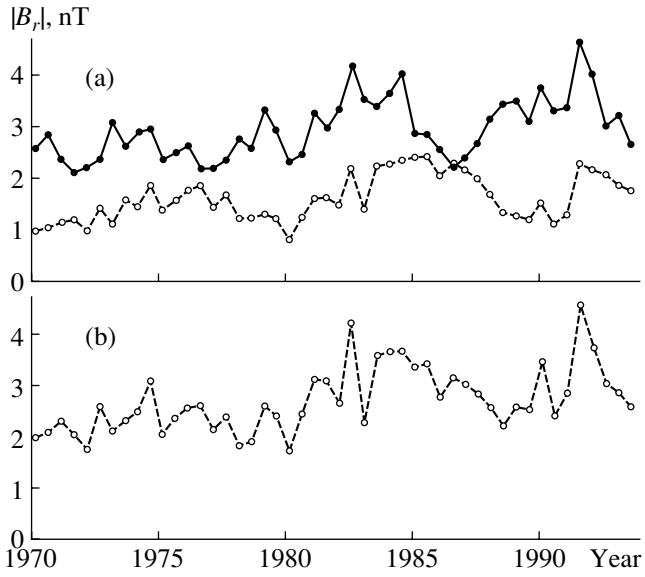

Fig. 1. Variation of the semiannual average of the radial component of the IMF at the Earth's orbit in 1970–1993: (a) measured values $|B_r|$ (solid circles) and extrapolated photospheric field $|B_r|'$ for a saturation factor of $\delta^{-1} = 1.8$ (open circles); (b) calculated values $|B_r|''$ for a factor of $\delta^{-1} = 4.5 - 2.5\sin^2\varphi$ (in each case, the three-month values from [3] are averaged over $\tau = 0.5$ yr).

between $|B_r|$ and the extrapolated values $|B_r|'$; the computed magnitude of the radial IMF component was a factor of two to three smaller than the true $|B_r|$ 1 AU from the Sun. (A substantial difference between the power spectra of the IMF and GMF variations was noted previously in [21].)

We reconstructed the graphs of [3] using an averaging interval of $\tau = 0.5$ yr. The results are shown in Fig. 1a, which shows the poor agreement between $|B_r|$ and $|B_r|'$, with a large vertical discrepancy. The correlation coefficient between $|B_r|$ and $|B_r|'$ is $r = 0.35$ (corresponding to 2.5σ).

However, upon correcting the maps using the latitude-dependent factor (1), Wang and Sheeley [3] obtained a satisfactory agreement between the measured and recalculated magnitudes of the radial component of the IMF ($|B_r|$ and $|B_r|''$, respectively) for both the overall (24-year) averages and their behavior with time. For the variations in the semiannual values of $|B_r|$ and $|B_r|''$ shown in Fig. 1, the correlation coefficient is $r = 0.69$, with a good agreement between the mean levels.

In addition to synoptic maps, several observatories obtained another time series for the same 24 years—GMF measurements, which provide independent information about the magnetic variability of the Sun. It is interesting to compare these with variations of the magnitude of the radial IMF component.

4. GMF SIGNAL OF THE SUN AS A STAR

The GMF for a given day is a weighted integrated value of the line-of-sight magnetic field of the visible hemisphere of the Sun. Measurements of the GMF were pioneered by Severny [5, 22] and his coworkers at the Crimean Astrophysical Observatory in 1968.

Such measurements are done using a Babcock magnetograph, which records the circular polarization in the wings of the λ 525.0 line. These measurements were conducted systematically at the MWO by Scherrer and Howard in 1970–1982 [7, 10] and have been carried out regularly at the WSO since 1975 [23] and at the Sayan Solar Observatory since 1982 (see [7–11, 24] for more details).

A total of 11 878 GMF measurements carried out at these four observatories in 1968–1999 have been published and are available for analysis. All are based on the measurements of λ 525.0 line. No special calibration or saturation factors were introduced. However, to obtain a unified time sequence, we multiplied the GMF values from each observatory by a normalizing coefficient k (see table), determined by the rms deviation Δ of the given dataset. This coefficient reduced Δ for each of the four independent datasets to the common rms value, 0.63 G (i.e., to the mean Δ for the four observatories). This yielded a single set of GMF values for 1968–1999, with the number of measurements $N = 11\,878$ and $\Delta = 0.63$ G. In this 32-year dataset, 9694 measurements were made in the interval 1970–1993 considered in [3].

Measured GMF of the Sun for 1968–1999

Observatory	Interval, years	N	Δ, G	k	Reference
Crimea	1968–1999	1707	0.661	0.953	[11, 25]
Mt. Wilson (MWO)	1970–1982	2457	0.670	0.940	[10]
Sayan (SSO)	1982–1993	313	0.775	0.813	[8, 9]
Stanford (WSO)1975–1999	7401	0.413	1.525	[23]	
All data	1968–1999	11878	0.629	–	–

As noted above, the strength of the GMF is determined chiefly by extensive areas of quiet photosphere occupied by background fields [5–7, 26]. The fields of ARs and spots are essentially balanced (they are closed configurations), and the dominant contribution to the GMF is made by open configurations, or, as is now commonly accepted, the fields of coronal holes. (Note, however, that some coronal holes may also be associated with closed configurations [27].) We emphasize that the GMF does not determine a mean (with a sign) strength of the photospheric field; instead, it is proportional to the *imbalance* between the contributions of open configurations with opposite polarities.

5. VARIATION OF THE MAGNITUDE OF THE GMF IN 1970–1993

We converted the 24-year GMF measurements into a series of 9694 magnitudes, which were then used to calculate half-yearly averages of the strength of the GMF, $|H|$. Their variations are shown in Fig. 2b. The overall mean of the GMF magnitude is $\langle |H| \rangle = 0.49$ G.

The variations in the GMF magnitude correlate well with the variations in the IMF ($|B_r|$) shown in Fig. 2a. The correlation coefficient is $r = 0.73$, much higher than for the $|B_r| - |B_r|'$ correlation for the two curves in Fig. 1a ($r = 0.35$). Applying a correction based on $\delta^{-1}(\varphi)$ [see expression (1)] to the synoptic maps [3] increases r to 0.69, but this values remains significantly lower than for the $|B_r| - |H|$ correlation.

Note that $|B_r|$, as well as the extrapolated fields from magnetograms and the GMF magnitude, display gradual increases with time. This is demonstrated by linear-regression equations calculated for the four quantities whose variations are represented in Figs. 1 and 2. Upon removing these linear trends, we obtain even more interesting values for the correlation coefficients:

$$|B_r| - |B_r|', r = 0.12,$$
$$|B_r| - |B_r|'', r = 0.57,$$
$$|B_r| - |H|, r = 0.74.$$

It follows that the IMF (we mean the radial component of the IMF $|B_r|$ unless otherwise specified) is best correlated with the GMF measurements *uncorrected* for saturation, rather than with the extrapolated synoptic maps corrected for saturation.

For each quantity, we obtained linear trends and determined the rms residuals after subtracting the trends Δ. For $|B_r|$, $|B_r|'$, and $|B_r|''$, these are 0.168, 0.247, and 0.201, respectively (in relative units). The variations of the GMF are much larger, $\Delta = 0.445$.

6. CALIBRATION OF THE GMF

The distributions of the line-of-sight velocity and UV emission in coronal holes—regions of open magnetic field—have demonstrated that the holes are sources of high-speed solar wind [28]. The field carried by the solar wind from coronal holes is determined by the magnetic-field topology in the holes and should therefore mainly determine the GMF of the Sun. There is some evidence that the magnetic fields in quiet regions and coronal holes are almost radial, at least at the level where the λ 525.0 line is formed; see, e.g., [2, 17]. (This same fact suggests that model interpolations have *limited usefulness*, since a radial photospheric field cannot be potential; see Section 9. This, however, does not prohibit using *measured* values of the photospheric field to impose boundary conditions for the potential-field problem.)

We assume that the mean strength of the photospheric background field is $H_0 \approx 2.0$ G [7, 26]. To crudely estimate the measured GMF, we also assume that the visible hemisphere is completely covered by a radial magnetic field H_0 (like a monopole field, or a dipole field viewed from a pole). We integrate the field over the solar disk taking into account the limb-darkening function and the inclination of the field lines θ to obtain the GMF:

$$|H| \approx 0.71 \times H_0 \approx 1.42 \text{ G}. \quad (4)$$

This is in satisfactory agreement with the maximum GMF amplitude ~ 1.1 G in Fig. 2b. On average, we

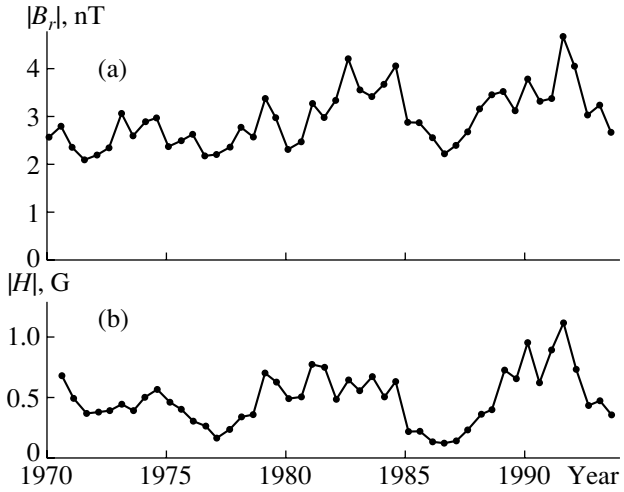

Fig. 2. Variation of the semiannual values of (a) the IMF $\mid B_r \mid$ and (b) the magnitude of the GMF $\mid H \mid$.

have for the radial IMF component at the Earth's orbit

$$\langle \mid B_r \mid_H \rangle = \alpha \times H_0 \approx 3.06 \text{ nT}, \qquad (5)$$

where

$$\alpha = \left(\frac{R_\odot}{R_E}\right)^2 \times \cos\psi \approx 1.53 \times 10^{-5}, \qquad (6)$$

and $\psi = 45°$ is the mean angle of the IMF Archimedes spiral 1 AU from the Sun (the subscript H in (5) refers to the GMF-based extrapolation). The value (5) agrees well with the observed 24-year mean for the radial component of the IMF: $\langle \mid B_r \mid \rangle = 2.95$ nT (Fig. 1; see also the similar treatment of Scherrer [7]).

Our result for the GMF is in contrast with the radial IMF extrapolated into the heliosphere using synoptic maps and the potential model (with thin current sheets); see our Fig. 1 and Fig. 2 in [3]. For the Stanford factor $\delta^{-1} = 1.8$, the overall average of the calculated IMF is $\langle \mid B_r \mid' \rangle = 1.61$ nT (Fig. 1a), which is a factor of 1.83 lower than the measured value, 2.95 nT. To obtain better agreement between $\mid B_r \mid$ and the IMF computed in the potential model, we must increase the photospheric field using the latitude-dependent factor $\delta^{-1}(\varphi)$ [see (1) and [3]], which is about a factor of 4.5 at the center of the disk and a factor of 2 at the poles.

Let us suppose, however, that the GMF is indeed underestimated due to saturation. In this case, according to the extrapolation [3], we should introduce Ulrich's factor $\delta^{-1}(\varphi)$ [16] for the background field; see (1) with φ replaced by θ. We also assume that the maximum observed magnitude of the GMF (without saturation taken into account) is 1.1 G. Integration of the uniform line-of-sight field over the solar disk (taking into account limb darkening) yields a coefficient of 2.55 instead of 0.71 in (4). Therefore, the maximum $\mid H \mid$ becomes $1.1 \times (2.55/0.71) \approx 3.95$ G, while the overall average GMF becomes about $(2.55/0.71) \times 0.49 \approx 1.76$ G. If we extrapolate this to the Earth's orbit in the simplest way [using (6)], we obtain for the mean IMF $\langle \mid B_r \mid_H \rangle \approx 2.69$ nT, which is close to the observed value $\langle \mid B_r \mid \rangle = 2.95$ nT.

Of course, this is actually impossible, since the mutual compensation of the fluxes of opposite polarities in the photosphere should substantially (by at least a factor of a few) reduce both overall averages, $\langle \mid H \mid \rangle$ and $\langle \mid B_r \mid_H \rangle$.

For the mean radial IMF component, introducing a saturation factor yields a strength that is too large compared to (5), $\langle \mid B_r \mid \rangle \approx \alpha \times H_0 \times 2.55/0.71 \approx 11.0$ nT. This is in strong disagreement with the measured IMF (see Fig. 1a, where the mean $\mid B_r \mid$ is about 3.0 nT).

Therefore, the factor $\delta^{-1}(\varphi)$ results in an erroneous, several-fold overestimation of the photospheric magnetic field. (We note that a similar extrapolation of our $\langle \mid H \mid \rangle = 0.49$ G to the Earth's orbit based on (6) yields the reasonable value 0.75 nT, which is about a quarter the actual value, $\langle \mid B_r \mid \rangle = 2.95$ nT. However, this may be due not to saturation of the magnetic-field signal but instead to the simple compensation of background fields of opposite polarities when the Zeeman polarization is integrated over the solar disk.)

These results argue against correcting measured solar magnetic field values using a saturation factor. At the very least, they cast doubt on the validity of the latitude dependence (1); thus, the situation with using the correction δ^{-1} becomes ambiguous and remains problematic (see also Section 8). In fact, when considering the GMF, no saturation factor is needed to

bring the effective mean strength of the background fields H_0 into agreement with the measured strength $|B_r|$. Moreover, as we saw in Section 5, the time variations of $|B_r|$ are also in better agreement with variations of the amplitude of the GMF than with variations of $|B_r|'$ or $|B_r|''$ based on a δ^{-1} correction.

If the visible disk of the Sun (more precisely, the central area with radius $\approx 0.6\ R_\odot$ [7]) is occupied by a unipolar background field, the maximum GMF strength is ≈ 1.42 G. This is in reasonable agreement with the actual GMF maximum, ≈ 1.1 G in Fig. 2b. (This figure, however, refers to semiannual averages, whereas the GMF magnitude may reach ≈ 3.2 G on our scale of GMF values on some days; this was the case, in particular, in 1991 [29].) At solar-activity minima, the GMF is weak and $|H| = 0.10$–0.15 G (Fig. 2b). As noted above, this is due to the mutual compensation of areas of background field with opposite polarities and the substantial decrease in the amplitude of the 27- to 28-day variations at solar-activity minima. Thus, there is a strong (to 50%), cyclic modulation of the GMF (seen in Fig. 2b), which greatly exceeds the modulation of the IMF.

7. EFFECTIVE STRENGTH OF THE PHOTOSPHERIC FIELD

The original values of $|B_r|$ (reduced as described in [3]) were averaged over three-month intervals. For a given day, however, the magnetograph records not the *true strength* of the photospheric field but instead a quantity proportional to the mean *magnetic flux* of a photospheric area corresponding to the spatial resolution of the instrument. Thus, the measuring procedure neglects fine structure of the fields—the fact that magnetic elements within the aperture of the telescope (and spectrograph) have different polarities and strengths. As before, we denote the mean effective strength of the background field (directed radially in the photosphere) as H_0, which we assumed to be 2.0 G. However, according to various estimates, it is actually equal to 0.8–2.2 G, even without any correction δ^{-1} for saturation; see, e.g., [7, 26]. We can now improve H_0 using the overall average $|B_r|$ (2.95 nT) for the 24-year IMF series:

$$H_0 = \frac{\langle |B_r| \rangle}{\alpha} = 1.93 \text{ G}. \qquad (7)$$

Since the pioneering publications of Severny [5, 22], it has been commonly acknowledged that the GMF is determined primarily by the excess *area* of the solar disk occupied by background fields of one polarity or another. It has also been indirectly implied that unipolar regions of large-scale field have nearly the same effective mean strength H_0. However, as we saw in Section 5, variations in $|B_r|$ are well correlated with variations in the amplitude of the GMF $|H|$. This means that variations in $|H|$ depend not only on the areas of background structures but also to a large extent on variations in H_0—at least on our averaging time scale, $\tau = 0.5$ yr.

It is therefore natural to suppose that (i) variations in the GMF are largely due to variations in H_0 and (ii) a substantial excess of one polarity or another over the solar disk—i.e., a relatively large magnetic imbalance, or a large GMF amplitude—is observed when H_0 is significantly increased. (This is consistent with the well-known fact that the elements that are predominant in the quiet photosphere (in terms of area) have the same sign that dominates in the background field and the GMF. This regularity underlies techniques for identifying structures in the solar background field.)

It is even reasonable to suggest that the initial origin for an imbalance, i.e., for a substantial growth in $|H|$, could be precisely a growth in the strength H_0 (of one polarity or another) over almost the entire visible hemisphere of the Sun, or over a substantial portion of this hemisphere.

Thus, we *postulate* in this section that variability of the GMF is mainly due to variations in H_0 rather than variations in the areas occupied by magnetic-field structures. In fact, area variations could well be secondary compared to variations in H_0. From the standpoint of the physics of solar magnetic structures and the dynamo mechanism, large-scale (global) variations in H_0—and, therefore, in the total magnetic flux of the photosphere—could be associated with the emergence of field from (or from beneath) the convection zone into the photosphere over the large areas characteristic of the large-scale structures of the background field.

8. RELATIVE VARIATIONS IN THE GMF AND IMF

Let us assume that linear trends in $|B_r|$ and $|H|$ are insignificant or have been removed. Variations about the overall averages are determined by the solar rotation, solar activity, the solar cycle, and the magnetic variability of the Sun in general. Variations due to changes in H_0 itself are also present. (We neglect complex heliospheric MHD processes and attendant phenomena; their effects should largely be smoothed out in the half-yearly averages.)

We introduce the following notation: $\delta(x)$ is the departure of a quantity x from its mean value, i.e., the *variation* of x; $\Delta(x)$ is the rms, or standard, deviation of $\delta(x)$; and H_0' is the actual (time-dependent) mean effective strength of the photospheric field. We will

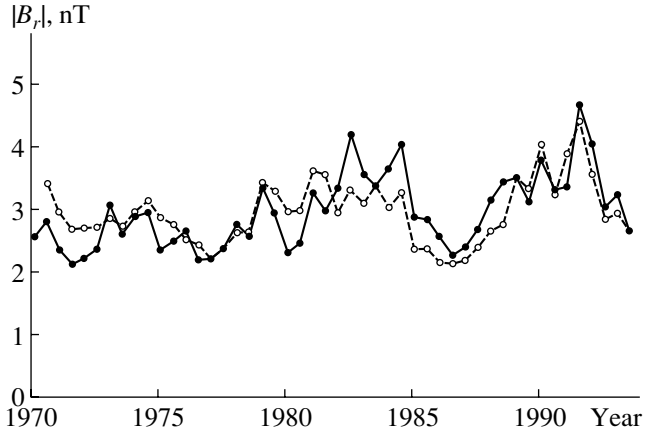

Fig. 3. Variations in the semiannual averages of the radial IMF component in 1970–1993: the solid circles and solid curve show the values measured at the Earth's orbit ($|B_r|$), and the open circles and dashed curve, an extrapolation $|B_r|_H$ based on the measured GMF of the Sun and the empirical law (8).

assume below that the magnetic-field lines are radial in the photosphere and, in accordance with the model of Parker [30], twisted in the heliosphere (this model is firmly supported by the *Ulysses* results [12]) and that the standard deviations of $|B_r|$ and H_0' are roughly the same.

We adopt $H_0' = H_0 + \delta(H_0')$ to be the strength of the background field and introduce the parameter $K = \Delta(|B_r|)/(\langle|B_r|\rangle) = 0.168$. We can then easily find

$$|B_r|_H = \alpha H_0 \times \left[1 + K\frac{|H| - \langle|H|\rangle}{\Delta(|H|)}\right]. \qquad (8)$$

Figure 3 shows the variations in $|B_r|_H$ computed using (8) compared to the actual variations in the radial IMF; the correlation coefficient is 0.74, as in Section 5. Therefore, the radial IMF can be much more reliably extrapolated to the Earth's orbit using observations of the GMF rather than synoptic maps of the photosphere and the potential model (as is now the standard practice).

According to Fig. 2, the extremum GMF values ($|H|$) are about 0.1 and 1.1 G. Thus, it follows from (8) that the effective strength of the background fields ranges from 1.35 to 2.84 G, with an average of about 1.93 G. These figures are in more or less good agreement with the estimates of [7, 26]. However, the GMF is zero on some days, while it sometimes (e.g., in 1991) reaches 3.2 G. Therefore, the actual range of variations in the effective strength of the photospheric field H_0' (on a daily time scale) is much wider, approximately from 1.2 to 6.0 G.

With regard to the sector structure of the IMF polarity, according to [3], the potential approximation results in a satisfactory agreement between the extrapolated and observed IMF structures (in particular, with respect to the high-latitude (up to 50°S) polarities indicated by the *Ulysses* data). The sector structure of the GMF also exhibits good agreement with that of the IMF, as has been demonstrated in a numerous studies [7, 24, 31, 32]. For this reason, we do not consider the polarities of the GMF and IMF. The dependence (8) can be written

$$|B_r| = \alpha H_0 \times \frac{1 + C|H|}{1 + C\langle|H|\rangle}, \qquad (9)$$

where $C = 1.241$ G^{-1} equalizes the scales of the *relative* variations in the IMF ($|B_r|$) and GMF ($|H|$). The correlation coefficient is $r = 0.74$, and this correlation is much better than the correlation between $|B_r|$ and the potential extrapolation [3]. It is especially interesting that the GMF data are *original,* without any correction for saturation.

It is best to compare our result for the GMF with the extrapolation [3] for $\delta^{-1} = \text{const}$ ($= 1.8$), since, in essence, this factor changes only the scale of the magnetic field in the potential model. For our data, this would imply an increase in the GMF by a factor of 1.8 (without changes in the relative GMF variations and, therefore, in the GMF–$|B_r|$ correlation), retaining a relatively high r. In contrast, the Wang–Sheeley extrapolation of synoptic maps with the factor $\delta^{-1} = 1.8$ yielded variations in the computed IMF ($|B_r|'$) that were virtually *uncorrelated* with variations in $|B_r|$ ($r = 0.12$)!

(Wang and Sheeley themselves noted that the resulting $|B_r|'$ values indicated the presence of broad maxima on the declining branches of the cycle and of minima near solar-activity maxima in 1979–1980 and 1989–1990 (Fig. 1a). Naturally,

using the latitude-dependent factor (1) enhances the contribution from low-latitude fields, especially in years of solar-activity maxima, which improves the correlation. However, the correlation remains markedly lower than the correlation between $|B_r|$ and the extrapolated GMF.)

9. CONCLUSION

Extrapolation of the photospheric field from the source surface to the Earth's orbit based on some potential model leads to a curious situation: the correlation with the actual strength $|B_r|$ (1 AU from the Sun) is worse for the computed, model radial IMF component than for $|B_r|$ values based on GMF measurements. This casts doubt on the validity of correcting synoptic photospheric field maps using a latitude-dependent saturation factor δ^{-1} [see (1) and Section 8]. Accordingly, the implication that the field is strongly concentrated at the Sun's poles (up to 10 G, according to [3]; see also [33]) is likewise put in doubt.

The satisfactory correlation between the GMF and IMF suggests that the usual interpretation invoking a saturation factor should be critically reviewed and that the problem of discrepancies between field measurements in various lines remains unresolved. We suggest that, together with purely solar effects, these discrepancies are largely associated with instrumental errors in measurements of the magnetic field, as well as complex photospheric factors related to the Zeeman splitting of absorption lines in the nonuniform solar atmosphere. The GMF strength ($|H|$) exhibits a larger relative modulation in the activity cycle that do the measured radial IMF component ($|B_r|$) and the extrapolated values of $|B_r|'$ and $|B_r|''$. This may be due to the fact that background fields with *opposite polarities* are averaged in GMF observations, while magnetogram measurements yield the strength of the IMF, independent of the direction of the magnetic vector (to some extent, this is also true in connection with the reduction of magnetic maps).

Thus, we conclude that, on average (over 24 years), the GMF better represents the behavior of the radial IMF component than does the field extrapolated from an imaginary source surface to the Earth's orbit using synoptic maps.

The IMF ($|B_r|$) and GMF are linked by the linear relationship (9) with a correlation coefficient $r = 0.74$, which can be written

$$|B_r| = \left(\frac{R_\odot}{R_E}\right)^2 \cos\psi (H_0)_{\min} \times (1 + C|H|), \quad (10)$$

where $(H_0)_{\min} = 1.20$ G is the minimum effective field strength in the quiet photosphere, $C = 1.24\ \mathrm{G}^{-1}$ and $|H|$ is the GMF amplitude (in G). The deviations from this dependence seen in Fig. 3 can be accounted for by IMF variations due to complex MHD processes in the heliosphere (in particular, interactions between magnetized solar-wind streams with differing speeds and shock waves). Some deviations can be attributed to the nonuniformity of the GMF data obtained at various observatories, which are subject to normalization errors associated with the reduction of the data to a single time sequence.

Dependence (10) argues in favor of the Parker model, in which open magnetic field lines issue radially from the photosphere, and are then twisted by the solar rotation into Archimedes spirals. As in the potential model, the field strength decreases in proportion to R^{-2} (where R is heliocentric distance).

The relative variations in $|B_r|$ show an approximately linear dependence on the synchronous variations of the (0.5-yr averaged) GMF and are proportional to fluctuations in the mean effective strength of the background fields, H_0'.

In other words, variations in the (radial) magnetic field are unisonic over the entire heliosphere and, on average, synchronous with fluctuations in the GMF of the Sun as a star, as well as with the effective strength H_0' (at least when averaged over several solar rotations).

It would be interesting to relate these global magnetic-field fluctuations, which involve the entire solar surface and heliosphere, to dynamo processes in and beneath the convection zone, where new magnetic flux appears to be generated. We note, however, that according to the *Ulysses* data the IMF is also highly sensitive to dynamical processes in the solar wind, especially plasma-compression effects. For this reason, it is difficult to use the strength of the IMF to directly judge the behavior of its true source—solar magnetic fields [12].

Data on the GMF confirm the presence of a positive trend in the strength of the solar magnetic field and—accordingly, in the IMF—in 1970–1993 [3, 34]. However, this trend was observed only within this restricted time interval; the complete data for the GMF in 1968–1999 do not show a considerable trend [29].

It is the photosphere, rather than an artificial spherical surface at a heliocentric distance of $\approx 2.5\ R_\odot$, that should be considered the source surface for the IMF ($|B_r|$). This reinforces the doubt cast by the *Ulysses* data [12] on commonly accepted models for the heliospheric field structure. (These models assume a strong dependence of the IMF on heliographic latitude at solar-activity minima, viz., an almost threefold magnetic-field excess over polar regions of the Sun.) Therefore, usual assumptions about the field distribution over the corona (determined by

dynamic coronal processes) and the source surface are not entirely correct, and potential models (without coronal currents between the photosphere and the imaginary spherical surface) and even those allowing for the presence of a heliospheric current sheet must be appreciably revised. Earlier, Balogh *et al.* [12] arrived at the same conclusion based on their analysis of *Ulysses* data for the IMF.

(For instance, Wang and Sheeley [2] noted the fundamental drawback of potential models that the photospheric magnetic field is nearly radial, and therefore undoubtedly nonpotential, at least at the level of formation of the λ 525.0 line.)

It follows from Figs. 2 and 3 that the GMF is an important characteristic of the magnetic variability of the Sun and of its cyclic activity. For this reason, GMF measurements are of no less interest than measurements of the sunspot index—the Wolf number—especially since it is the GMF with which the radial IMF component is so strongly correlated (see Section 5).

ACKNOWLEDGMENTS

We are grateful to M.B. Kraĭnev and M.A. Livshits for helpful discussions of some problems of heliospheric physics and GMF measurements, to V.I. Khaneĭchuk and N.G. Sunitsa for their assistance in reducing the observational data, and to the referees for a number of valuable comments. This work was partially supported by INTAS (grant no. 2000-840).

REFERENCES

1. M. B. Krainev, G. A. Bazilevskaya, and V. S. Makhmutov, *The Large-Scale Structure of Solar Activity* (Main Astron. Obs., St. Petersburg, 2000), p. 121.
2. Y.-M. Wang and N. R. Sheeley, Jr., Astrophys. J. **392**, 310 (1992).
3. Y.-M. Wang and N. R. Sheeley, Jr., Astrophys. J. Lett. **447**, L143 (1995).
4. J. M. Wilcox, in *IAU Symposium 43: Solar Magnetic Fields,* Ed. by R. Howard (IAU, Dordrecht, 1971), p. 744.
5. A. B. Severny, Q. J. R. Astron. Soc. **12**, 363 (1971).
6. V. A. Kotov, N. N. Stepanyan, and Z. A. Shcherbakova, Izv. Krym. Astrofiz. Obs. **56**, 75 (1977).
7. P. H. Scherrer, Stanford Univ. Inst. Plasma Res. Rep., No. 554 (1973).
8. V. M. Grigoryev and M. L. Demidov, Sol. Phys. **114**, 147 (1987).
9. V. A. Kotov, M. L. Demidov, V. I. Khaneĭchuk, and T. T. Tsap, Izv. Krym. Astrofiz. Obs. **94**, 110 (1998).
10. V. A. Kotov, P. H. Scherrer, R. F. Howard, and V. I. Haneychuk, Astrophys. J., Suppl. Ser. **116**, 103 (1998).
11. V. A. Kotov, V. I. Khaneĭchuk, and T. T. Tsap, Astron. Zh. **76**, 218 (1999) [Astron. Rep. **43**, 185 (1999)].
12. A. Balogh, E. J. Smith, B. T. Tsurutani, *et al.*, Science **268**, 1007 (1995).
13. R. Howard and J. O. Stenflo, Sol. Phys. **22**, 402 (1972).
14. J. O. Stenflo, Sol. Phys. **32**, 41 (1973).
15. S. I. Gopasyuk, O. S. Gopasyuk, I. P. Zalesov, *et al.*, Astron. Zh. **77**, 547 (2000) [Astron. Rep. **44**, 481 (2000)].
16. R. K. Ulrich, in *Cool Stars, Stellar Systems, and the Sun,* Ed. by M. S. Giampapa and J. A. Bookbinder (ASP, San Francisco, 1992), p. 265.
17. L. Svalgaard, T. J. Duvall, Jr., and P. H. Scherrer, Sol. Phys. **58**, 225 (1978).
18. S. I. Gopasyuk, V. A. Kotov, A. B. Severny, and T. T. Tsap, Sol. Phys. **31**, 307 (1973).
19. S. I. Gopasyuk and A. B. Severnyĭ, Pis'ma Astron. Zh. **9**, 120 (1983) [Sov. Astron. Lett. **9**, 65 (1983)].
20. S. I. Gopasyuk, Izv. Krym. Astrofiz. Obs. **72**, 159 (1985).
21. Yu. R. Rivin and V. N. Obridko, Astron. Zh. **69**, 1083 (1992) [Sov. Astron. **36**, 557 (1992)].
22. A. Severny, Nature **224**, 53 (1969).
23. Solar-Geophysical Data Prompt Reports (NOAA, Boulder, 1975–2000).
24. P. H. Scherrer, J. M. Wilcox, V. Kotov, *et al.*, Sol. Phys. **52**, 3 (1977).
25. V. A. Kotov, V. I. Khaneĭchuk, and T. T. Tsap, Izv. Krym. Astrofiz. Obs. **97**, 100 (2001).
26. V. A. Kotov and N. N. Stepanyan, Izv. Krym. Astrofiz. Obs. **62**, 117 (1980).
27. N. N. Stepanyan, private communication (2000).
28. D. M. Hassler, I. F. Dammasch, P. Lemaire, *et al.*, Science **283**, 810 (1999).
29. V. A. Kotov and I. V. Kotova, Pis'ma Astron. Zh. **27**, 302 (2001) [Astron. Lett. **27**, 260 (2001)].
30. E. N. Parker, Astrophys. J. **128**, 664 (1958).
31. A. Severny, J. M. Wilcox, P. H. Scherrer, and D. S. Colburn, Sol. Phys. **15**, 3 (1970).
32. V. N. Obridko and B. D. Shelting, Sol. Phys. **184**, 187 (1999).
33. V. A. Kotov and L. S. Levitskiĭ, Izv. Krym. Astrofiz. Obs. **71**, 32 (1985).
34. M. Lockwood, R. Stamper, and M. N. Wild, Nature **399**, 437 (1999).

Translated by A. Getling

Astronomy Reports, Vol. 46, No. 3, 2002, pp. 255–258. Translated from Astronomicheskiĭ Zhurnal, Vol. 79, No. 3, 2002, pp. 281–285.

Influence of Collective Plasma Processes on the Theoretical Flux of Solar Neutrinos

A. V. Fedorova and A. V. Tutukov

Institute of Astronomy, Russian Academy of Sciences, Pyatnitskaya ul. 48, Moscow, 109017 Russia

Received May 12, 2001

Abstract—Calculations using a standard solar model show that the decrease in proton–proton chain nuclear reaction rates due to collective plasma processes increases the theoretical solar neutrino flux, while the decrease in the opacity of the solar interior associated with the same processes decreases this flux. Taking into account both of these effects decreases the total neutrino flux, easing the solar neutrino problem.

1. INTRODUCTION

The puzzle of the solar neutrino flux remains a central astrophysical problem. All available detectors measure neutrino fluxes that are appreciably lower than theoretically predicted. According to review [1], the neutrino flux measured by a chlorine detector is 2.55 SNU, while the theoretical flux is 4–9 SNU. Fluxes measured by gallium detectors are 70 SNU (SAGE experiment) and 76 SNU (GALLEX experiment), while the theoretical flux is 100–140 SNU. The observed flux for a water detector (Kamiokande experiment) is only about 40% of the theoretical flux.

There are two basic ways to solve this problem: improvement of the solar model and detailed studies of the properties of neutrinos. A large number of studies have been carried out in the last few decades in both these directions (see, for example, the reviews [1–3]).

Initially, most attempts concentrated on the first approach. The theoretical flux of neutrinos was substantially decreased via refinement of such fundamental parameters as the rates of nuclear reactions, the equation of state and opacity of solar material, the chemical composition of the Sun, etc. Nevertheless, standard solar models have not been able to decrease the theoretical neutrino flux to values close to those observed. On the other hand, a number of so-called nonstandard solar models have been put forward. These predict lower neutrino fluxes but are based on assumptions that fall outside the framework of modern concepts about stellar internal structure and evolution [2]. As noted by Bahcall [4], many nonstandard solar models are mutually contradictory, so most must inevitably be incorrect. In any case, it is debatable if any of the nonstandard models could correspond to the real Sun.

Important results have also been achieved with the second approach indicated above. Studies of the properties of neutrinos led to the hypothesis of neutrino oscillations (i.e., transformations from one to another kind of neutrino) in the solar material and along their path from the Sun to Earth [5, 6]. As a result, some fraction of observable neutrinos can be transformed to nonobservable ones, decreasing the detected flux. This is a very promising hypothesis, and it is fully capable of solving the solar neutrino problem.

Nevertheless, studies aimed at clarifying the physics of solar material continue, since, naturally, we cannot be sure that our understanding of processes occurring in the solar interior is absolutely correct. In recent years, one of the basic approaches to obtaining a better understanding of the physics of solar material has become comprehensive investigations of the properties of plasma. Their detailed computations of collective plasma processes in the solar interior led Tsytovich *et al.* [7], Tsytovich [8] to conclude that (1) the real opacity coefficient of solar material may be approximately 10% lower than commonly accepted [7] and (2) the real rates of nuclear reactions in the proton–proton chain may be lower than those commonly used, with the decrease in the reaction rate being greater the greater the charges of the nuclei participating in the reaction [8]. Another idea put forward in [7, 8] is that the predicted decreases in the opacity and nuclear reaction rates should decrease the theoretical flux of neutrinos from the Sun, easing the solar neutrino problem.

In the present work, we study the influence of the predicted changes on the parameters and theoretical neutrino flux of the solar model numerically. Four versions of the standard model are considered, namely, with (1) standard nuclear-reaction rates and standard opacity, (2) reaction rates decreased in accordance with [8] and standard opacity, (3) standard reaction

1063-7729/02/4603-0255$22.00

Table 1. Coefficients of decrease in p–p chain nuclear reaction rates

Reaction	Coefficient
$^1\mathrm{H}(p, e^+\nu_e)^2\mathrm{H}$	1.106
$^2\mathrm{H}(p, \gamma)^3\mathrm{He}$	1.107
$^3\mathrm{He}(^3\mathrm{He}, 2p)^4\mathrm{He}$	1.223
$^3\mathrm{He}(^4\mathrm{He}, \gamma)^7\mathrm{Be}$	1.223
$^7\mathrm{Li}(p, \alpha)^4\mathrm{He}$	1.571
$^7\mathrm{Be}(p, \gamma)^8\mathrm{B}$	2.087
$^7\mathrm{Be}(e^-, \nu_e)^7\mathrm{Li}$	2.166

Table 2. List of computed solar models

Model	Reaction rates	Opacity
1	Standard	Standard
2	Decreased	Standard
3	Standard	Decreased
4	Decreased	Decreased

Table 3. Parameters of computed solar models

Model	X	l/H_p	$T_c/10^7$, K	ρ_c, g/cm^3	F(Cl), SNU	F(Ga), SNU
1	0.716	1.81	1.48	130	4.60	98.6
2	0.719	1.78	1.50	134	5.48	99.9
3	0.734	1.78	1.46	131	3.50	95.5
4	0.738	1.73	1.47	134	4.04	95.8

Note: X is the initial hydrogen content, l/H_p a parameter of convection theory, T_c and ρ_c the temperature and density at the solar center, and F(Cl) and F(Ga) the theoretical neutrino fluxes for chlorine and gallium detectors, respectively.

rates and the coefficient of opacity decreased by 10%, as suggested in [7], and (4) decreased reaction rates and coefficient of opacity. Our computations showed that the decrease in the nuclear reaction rates results in an increase in the theoretical neutrino flux, but the decrease in the opacity leads to a decrease in this flux. A simultaneous decrease in both the reaction rates and the opacity, overall, decreases the neutrino flux. Therefore, the proposed changes in the properties of the material in the solar interior implied by studies taking into account collective plasma processes can help solve the solar neutrino problem.

2. COMPUTATION OF THE SOLAR MODEL

2.1. Method of Computing the Standard Model

The solar evolution was computed using software based on the sweep method, intended for studying stars of low and moderate masses. We used a tabular equation of state obtained in [9, 10]. The opacity was calculated using tables from [11, 12]. We adopted the nuclear reaction rates from [13, 14]. We assumed that the CNO chain was in equilibrium but that the proton–proton (p–p) chain was not. The age of the modern Sun was taken to be 4.6×10^9 yr. The heavy-element content Z was taken to be to 0.017 [15]. The initial values of the hydrogen and helium contents, X and Y, and the ratio l/H_p in mixing-length theory were chosen by fitting the Sun; i.e., by computing a model for the modern Sun whose radius and luminosity are equal to the actual values within a specified accuracy. The initial abundances of deuterium and ^{3}He were taken to be 1.9×10^{-4} and 1.0×10^{-4}, respectively. The locations of the boundaries of the convection zones were calculated using the Schwarzschild criterion. Diffusion of hydrogen and helium was not taken into account in the computations. The evolution of the Sun from the stage of gravitational contraction to the main sequence was computed.

2.2. Coefficients of Decrease in the Reaction Rates and Opacity

The coefficients of decrease in the rates of proton–proton chain reactions taken from [8] are presented in Table 1.

The decrease in the coefficient of opacity was taken into account by multiplying by a constant factor of 0.9 throughout the star. We emphasize that this is a rather simplified interpretation of the results of [7], since the corresponding decrease deduced in that work refers only the central region of the Sun.

3. COMPUTATION RESULTS

3.1. Parameters of the Computed Solar Models

Table 2 presents a list of the solar models we computed. The parameters of these models are given in Table 3.

3.2. Effect of Decreasing the Nuclear Reaction Rates

The results for models 1 and 2 from Table 3 show that the decrease in the rates of proton–proton chain reactions increases the theoretical neutrino flux from the Sun. The flux measured by chlorine detectors should increase by 0.88 SNU, or 20%, whereas the flux measured by gallium detectors should increase by 1.3 SNU, or 1.4%.

This result can be explained qualitatively as follows. The luminosity in the computed model—the amount of nuclear energy released per unit time—is fixed and equal to the solar luminosity. Therefore,

a decrease in the reaction rates should lead to an increase in the temperature and density in the central regions of the star to compensate the lower energy release. Indeed, as we can see in Table 3, the central temperature and density in model 2 are greater than in model 1. On the other hand, a careful study of neutrino generation in the proton–proton chain shows that the relative contribution of the ppIII channel, which is responsible for the production of boron neutrinos, increases as the temperature and density increase. It is precisely boron neutrinos that make the largest contribution to the flux measured by chlorine detectors. Therefore, despite the fact that the total energy release in proton–proton chain reactions (i.e., to first approximation, the number of reactions per unit time) is the same for models 1 and 2, the relative contributions from the different channels change, such that the neutrino flux increases in the model with decreased nuclear reaction rates. The relative increase in the flux predicted for chlorine detectors proves to be considerably greater than for gallium detectors, since high-energy boron neutrinos contribute less to the flux measured by gallium detectors.

We also carried out test computations of the solar models using the coefficient from [8] for only one reaction of the proton–proton chain, while the rates of other reactions were kept standard. The aim of such computations was to identify particular reactions for which the rate variations were the most significant. The theoretical neutrino fluxes for these nonstandard models derived in this way are presented in Table 4.

We emphasize that these results hold no significance on their own and can be used only to draw certain obvious qualitative conclusions. Changing the rate of reaction 2 impacts the solar model least: since this rate is considerably greater than the rate for reaction 1 (the first reaction of the proton–proton chain), the effective rate of the sequence depends only on the rate of reaction 1. On the other hand, a considerable decrease in the theoretical fluxes can be achieved when the rates of reactions 4 and 5 are decreased, due to the decrease in the relative contribution of the ppIII channel. Therefore, although a simultaneous decrease in the rates of all reactions increases the neutrino flux, a decrease in the rates of some specific reactions can substantially decrease this flux. In addition, decreasing the rate of reaction 6 leads to the opposite effect, due to the increase in the relative contribution of the ppIII channel to the energy production.

3.3. Effect of Decrease in the Opacity

The parameters of models 1 and 3 from Table 3 show that decreasing the opacity of the solar material decreases the theoretical solar neutrino flux: the flux that should be measured by chlorine detectors decreases by 1.10 SNU, or 34%, while the flux measured by gallium detectors should decrease by 3.1 SNU, or 3.1%.

Table 4. Neutrino fluxes for solar models in which the rate of only one reaction was decreased

No.	Reaction	F(Cl), SNU	F(Ga), SNU
1	$^1\mathrm{H}(p, e^+\nu_e)^2\mathrm{H}$	5.70	101.4
2	$^2\mathrm{H}(p, \gamma)^3\mathrm{He}$	4.60	98.6
3	$^3\mathrm{He}(^3\mathrm{He}, 2p)^4\mathrm{He}$	5.02	100.7
4	$^3\mathrm{He}(^4\mathrm{He}, \gamma)^7\mathrm{Be}$	3.88	94.9
5	$^7\mathrm{Be}(p, \gamma)^8\mathrm{B}$	2.78	98.1
6	$^7\mathrm{Be}(e^-, \nu_e)^7\mathrm{Li}$	8.66	99.7

The fact that decreasing the opacity of the solar material can decrease the solar neutrino flux has been known for a long time (see, for example, [16]). This behavior has the following qualitative interpretation: the decrease in opacity leads to a smaller temperature gradient inside the star (i.e., a smaller rate of decrease in the temperature from the center to outer layers). As a result, the temperature at the center decreases, and the release of nuclear energy corresponding to the fixed solar luminosity occurs in a region that is somewhat larger than in the standard-opacity case. This temperature decrease in the zone of energy release, in turn, decreases the theoretical neutrino flux. As for model 2, the relative change of the predicted flux for chlorine detectors will be appreciably greater than for gallium detectors.

Of course, it is of interest to consider the influence of a further decrease in the opacity on the solar model. Computations with an opacity coefficient decreased by 20% (i.e., twice that assumed in [7]) gave theoretical neutrino fluxes of 2.56 SNU for chlorine detectors and 92.2 SNU for gallium detectors. Therefore, it is sufficient to decrease the opacity by an additional 10% to obtain predicted neutrino fluxes for chlorine detectors close to those observed. Unfortunately, this result can be interpreted only as a test. In addition, the solar neutrino problem for gallium detectors remains unresolved in this case.

3.4. Effect of Simultaneous Decrease in the Reaction Rates and Opacity

Model 4 from Table 3 includes both the proposed changes in the physics of solar material. The parameters for models 1 and 4 show that simultaneously taking into account decreases in the proton–proton chain reaction rates and in the opacity leads to an overall decrease in the theoretical solar neutrino flux:

the flux expected for chlorine detectors decreases by 0.56 SNU, or 22%, while that for gallium detectors decreases by 2.7 SNU, or 2.8%.

Therefore, despite the increase in the neutrino flux brought about by a decrease in the reaction rates, the effect of decreasing the opacity proves to be stronger, so the resulting theoretical neutrino flux for the solar model decreases. The influence of the opacity change on the expected fluxes for chlorine detectors is considerably greater than for gallium detectors.

4. CONCLUSION

We can draw the following conclusions from our computations of modern solar models.

(1) Decreasing the rates of proton–proton chain nuclear reactions in accordance with the coefficients presented in [8] increases the theoretical neutrino flux in the modern model for the Sun. This theoretical flux increases by 20% for chlorine detectors and by 1.4% for gallium detectors.

(2) Decreasing the coefficient of opacity of the solar material by 10%, in accordance with [7], decreases the theoretical neutrino flux. The expected flux for chlorine detectors decreases by 34% and that for gallium detectors by 3.1%.

(3) A simultaneous decrease in both the nuclear reaction rates and the coefficient of opacity in accordance with [7, 8] results in an overall decrease in the theoretical neutrino flux. The expected flux for chlorine detector decreases by 22% and that for gallium detectors by 2.8%.

Therefore, our computations confirm the hypothesis, put forward in [7], that a decrease in the opacity of the solar material should lead to a decrease in the theoretical solar neutrino flux. On the other hand, our results refute the analogous suggestion about the influence of the nuclear reaction rates on the neutrino flux put forward in [8]. However, the effect on the solar model of decreasing the opacity proves to be stronger than the effect of decreasing the nuclear reaction rates. As a result, the proposed changes in the physics of the material in the solar interior indicated by studies taking into account collective plasma processes, overall, result in a decrease in the theoretical neutrino flux and can help ease the solar neutrino problem.

5. ACKNOWLEDGMENTS

This work was supported by the Russian Foundation for Basic Research (project no. 99-02-17619).

REFERENCES

1. A. V. Kopylov, Priroda, No. 5, 31 (1998); No. 6, 27 (1998).
2. A. V. Fedorova, in *Modern Problems of Physics and Stellar Evolution* [in Russian] (Nauka, Moscow, 1989), p. 268.
3. J. N. Bahcall, *Neutrino Astrophysics* (Cambridge Univ. Press, Cambridge, 1989; Mir, Moscow, 1993).
4. J. N. Bahcall, Sol. Phys. **100**, 53 (1985).
5. S. P. Mikheev and A. Yu. Smirnov, Usp. Fiz. Nauk **153**, 3 (1987) [Sov. Phys. Usp. **30**, 759 (1987)].
6. S. S. Gernshteĭn, E. P. Kuznetsov, and V. A. Ryabov, Usp. Fiz. Nauk **167**, 811 (1997) [Phys. Usp. **40**, 773 (1997)].
7. V. N. Tsytovich, R. Bingham, U. de Angelis, and A. Forlani, Usp. Fiz. Nauk **166**, 113 (1996) [Phys. Usp. **39**, 103 (1996)].
8. V. N. Tsytovich, Astron. Astrophys. **356**, L57 (2000).
9. G. Fontaine, H. C. Graboske, and H. M. van Horn, Astrophys. J., Suppl. Ser. **35**, 293 (1977).
10. D. Saumon, G. Chabrier, and H. M. van Horn, Astrophys. J., Suppl. Ser. **99**, 713 (1995).
11. C. A. Iglesias and F. J. Rogers, Astrophys. J. **464**, 943 (1996).
12. D. R. Alexander and J. W. Ferguson, Astrophys. J. **437**, 879 (1994).
13. M. J. Harris, W. A. Fowler, G. R. Caughlan, and B. A. Zimmerman, Ann. Rev. Astron. Astrophys. **21**, 165 (1983).
14. G. R. Caughlan, W. A. Fowler, M. J. Harris, and B. A. Zimmerman, At. Data Nucl. Data Tables **32**, 197 (1985).
15. A. Dar and G. Shaviv, Astrophys. J. **468**, 933 (1996).
16. J. N. Bahcall, W. F. Huebner, N. H. Magee, *et al.*, Astrophys. J. **184**, 1 (1973).

Translated by Yu. Dumin